Optical Trapping Using a Photonic Crystal Cavity: Design and Sample Fabrication

by

Seyed Hamed Mirsadeghi

B.Sc., Shahid Beheshti University, 2007

A THESIS SUBMITTED IN PARTIAL FULFILLMENT OF
THE REQUIREMENTS FOR THE DEGREE OF
Master of Science

in

The Faculty of Graduate Studies

(Physics)

The University of British Columbia

(Vancouver)

April, 2010

ABSTRACT

A photonic crystal (PC) structure for trapping a 50nm radius dielectric particle at a precise location on a silicon surface in an organic solvent environment has been designed and all of its key components have been fabricated. The high gradient of electric field intensity in a PC cavity mode, with wavelength ~ 1.5 μm, exerts a radiation force toward the center of the cavity. The Finite Difference Time Domain (FDTD) modeling method was used to design a symmetric (input/output) structure that consists of two grating couplers, two parabolic tapered waveguides, two single mode ridge waveguides, two photonic crystal waveguides and a single three-missing-hole (L3) PC cavity. These elements are formed in a 196 nm thick silicon slab atop a micron thick layer of silicon dioxide (a silicon-on-insulator, SOI wafer). The grating couplers consist of a rectangular lattice of air holes in the Si slab for coupling near-normal incidence continuous wave (cw) laser light in and out of the structure. The tapered waveguides smoothly take the 22 μm wide multimode beam from the grating coupler down to a 409 nm wide single mode ridge waveguide. The ridge waveguides are coupled to PC waveguides through a slightly flared interface region. The PC waveguides were made in a triangular lattice of air holes by removing 7 periods of holes in the Γ-K direction, and they were end-coupled to the L3 PC cavity through two holes of different radii.

The grating couplers, tapered waveguides, and single mode ridge waveguide structures were carried over from existing designs after optical transmission experiments showed that they behaved well (the maximum coupling wavelength shifts ~ 90 nm) in a solvent environment (n~ 1.44). To maximize the optical energy that could be trapped in the L3 microcavity, and hence maximize the optical trapping force for a given laser power, the PC cavity and PC waveguides had to be modified from the standard geometry. Instead of merely leaving out holes in an otherwise uniform 2D triangular photonic crystal, the row of holes directly adjacent to the

photonic crystal waveguides were decreased in radius by 27%, from 126nm to 92.4nm, in order to increase the group velocity and minimize propagation losses in the waveguide section. The two holes on either side of the L3 cavity were first shifted and shrunk to maximize the vertical quality factor (Q_v) for an isolated cavity (Q_v ~3800), and then readjusted when integrated with the waveguides in order to have a structure with the highest possible Q value, while having maximum coupling efficiency between the PC waveguides and the cavity (design value of ~50%).

The radiation force on the dielectric sphere was exactly calculated using FDTD simulations to evaluate the Maxwell Stress Tensor (MST) in the presence of the particle to be trapped. This result was compared to that obtained using the simpler dipole approximation, and good agreement between them was found. The component of the radiation force normal to the silicon surface at the cavity centre, when the sphere is ~75nm above the surface of the silicon slab, was found to be ~8 fN for a cw laser power of ~5 mW. This force corresponds to a trapping potential energy of ~ 60 kT at room temperature, which is bigger than the minimum required potential energy for stable trapping (~10kT).

The fabrication of the structure was done by electron beam lithography and chlorine plasma etching. Because of the limited area of patterning possible in the in-house lithography system, it was not possible to pattern the whole structure at once. Instead, the tapered, ridge and PC waveguides and the cavity were fabricated so that they could be placed in the centre of multimode ridge waveguides with grating couplers on each end, fabricated separately. Four samples were successfully fabricated after considerable process development.

The Q factors for some of the fabricated samples were measured from the cavity enhanced photoluminescence emission of PbSe quantum dots deposited on the sample surface. A vertical Q factor of 3600 (in vacuum environment) was measured for an isolated cavity, which corresponds to a Q_v of 3800 (in solvent environment) in the FDTD simulations. Also, the Q of the overall structure (cavity and the waveguides) was measure to be 1050 in vacuum, which from simulations is equivalent to a Q of 1800 in a solvent. These Q values and the resonant frequencies of the modes are in close, but not perfect agreement with the simulation results.

TABLE OF CONTENTS

LIST OF FIGURES

LIST OF TABLES

ACKNOWLEDGMENT

First and foremost, I would like to express my sincere gratitude to my supervisor, Dr. Jeff Young for his inspiration, guidance and continuous support during my Masters study. I really appreciate the time and energy that you spent for guiding and encouraging me all the time during my research. My special thanks to Dr. Haijun Qiao and Dr. George Rieger for their leadership and support throughout this work. And my special thanks to Charles Foell, who patiently taught me the SEM patterning and ECR process. It was a pleasure working with you. Thanks to the rest of the Nanolab members for their help and good company during my stay in the lab, Hailong Ning, Stephanie Flynn, Ellen Schelew.

I would like to thank Mario Beaudoin for his help in the cleanroom, Derrick Horne for his valuable help in SEM Imaging.

I'd also like to thank my family for keeping in such close contact and for providing so much support and encouragement.

I also like to thank my friends specially, Mohammad Modarres and Milad Omidi for their invaluable friendship.

To My Family & Friends

CHAPTER 1 INTRODUCTION

1.1 Motivation And Objectives

1.1.1. Engineered structures for the study of light-matter interactions at the quantum level

There is a desire to reduce physical systems down to their basic elements to investigate and engineer their interactions at a fundamental level. Cavity quantum electrodynamics (CQED) is one example involving the fundamental interaction of resonant electrons and photons. In the term "cavity QED," "cavity" refers to an optical or microwave resonator and "QED" implies the interaction of some material system (usually atomic or atomic-like) with the electromagnetic field (photons) localized inside the cavity [**Mabuchi2002**]. The presence of a cavity can insulate a system of atoms and photons from decoherence (which is mainly due to the emission or escape of photons into the surrounding continuum (vacuum)). Such systems are ideal for studying light-matter interactions and matching theory with experiment in the study of quantum coherence. They have already played a central role in basic research on quantum physics, especially in connection with decoherence, measurements, and entanglement. [**Mabuchi1999**, **Vernooy1998a**].

Depending on how lossy a cavity is, two different regimes can be defined: the strong and weak coupling regimes. In the first one, all decoherence processes affecting either the emitter or the photon are slow and this presents one of the best candidates for the experimental realization of quantum information science (QIS) protocols and systems [**Martini2002**]. The long-lived internal states of the atoms are well suited for the storage of quantum information, and the interaction of atoms with light can be used for readout and transmission. More specifically, many

of the physical requirements for quantum computation [**DiVincenzo2000**] are satisfied by confining a small number of atoms, molecules or "artificial atoms", eg. quantum dots (QD), to a cavity in such a way that they are individually addressable by laser light and can undergo controllable interactions with each other [**McKeever2004**]. The second, weak coupling regime applies, when the decoherence time is short compared to the characteristic time for the atoms and cavity mode to exchange excitations, but still large enough to significantly enhance the vacuum emission properties of the atoms (the Purcell effect [**Purcell1946**]). An interesting application of the Purcell effect uses the enhanced SE, from a single atom, or "artificial atom", to produce non-classical, "single photon sources" [**Gerard2003, Claudon2010**, **Heindel2010**, **Shields2007**].

While the most revealing research results in CQED have so far resulted from real atoms inside very high *finesse* (well isolated), very short (small mode volume, large electric field for a single trapped photon) Fabry-Perot cavities, there is much interest in developing more scalable, and more flexible CQED systems using semiconductor chip technologies. Most research along these lines has involved microfabricated cavities coupled to "artificial atoms" consisting of epitaxially grown quantum dots **[Faraon2008**, **Hennessy2007**, **Reithmaier2004],** or colloidal nanocrystals [**Bose2009**, **Bose2007**, **Pattantyus-Abraham2009**]. Depending on the specific application, the relevant Figure of merit for the cavities is either Q/V *or* $Q/V^{1/2}$, where Q is the quality factor (the higher the Q, the more isolated the photons in the cavity), and V is volume occupied by the mode (the smaller is V, the larger is the electric field associated with one photon in the mode). An advantage of microfabricated cavities is that their mode volumes can be rather easily made much smaller than conventional mirror-based Fabry-Perot cavities. However, in many cases small mode volume cavities have unacceptably low Q values. Among the different kinds of cavities studied to date, "planer photonic crystal (PC) cavities" offer a good compromise for CQED experiments due to their relatively high Q factors, and relatively small mode volume [**Song2005, Akahane2005, Tanabe2007**]. Planar photonic crystal cavities are discussed further below.

Both epitaxial quantum dots and colloidal nanocrystals exhibit sharp atomic-like absorption spectra (sharp "two-level system" threshold absorption with a slowly rising background to higher energies). [**Imamoglu1999, Loss1998**] They can have the advantage of higher dipole transition moments as compared to true atomic systems (enhancing the coupling to photons), their resonant frequency can be varied over wide ranges by controlling their growth

conditions, and their location is fixed in relation to the cavity. [**Khitrova2006**]. The main disadvantages of artificial atoms have to do with the stochastic nature of their centre frequencies (no two artificial atoms are identical), and their relatively strong coupling to vibrations (phonons), which introduces additional decoherence (above and beyond radiative coupling to the vacuum).

Self-assembled, epitaxial QDs have been successfully coupled with PC cavities in the strong coupling regime [**Faraon2008, Hannessy2007**, **Reithmaier2004, Thon2009**], but the strength of the coupling is just barely enough to overcome the dephasing in these demonstrations. Colloidal QDs such as CdSe and PbS have been successfully coupled to engineered microcavities [**Fushman2005**], but the strong coupling regime has not been realized due to the stronger dephasing rate in colloidal, versus epitaxial quantum dots. Nevertheless, the colloidal nanocrystal system offers important possibilities for scalable quantum computation and QED applications [**Bose2009**]. One advantage of using Pb-chacolgenide QDs over self-assembled QDs is the ability to integrate them with silicon-based microcavities, thus tapping into the vast silicon processing infrastructure [**Bose2007, Wu2007**].

Further progress in QD-based CQED technology has been partially hindered by the conventional practice of incorporating many QDs at random locations in the cavity, leading to indirect/off-resonant coupling to other QDs overlapping the mode. Observation and manipulation of quantum effects requires the deterministic placing of one or more QDs at well defined locations in a cavity [**Gerard2003, Hennessy2007**]. Young's group has developed a multi-step lithography process for locating just a few 5 nm diameter PbSe or PbS nanocrystals within the main antinode of a photonic crystal microcavity with a Q value of ~ 3500, and mode volume of 0.12 μm^3, made in the top silicon layer of a silicon-on-insulator (SOI) wafer [**Pattantyus-Abraham2009**]. This material system combination exhibits nanocrystal-cavity coupling (weak coupling regime) at room temperature [**Pattantyus-Abraham2009**], and efforts are underway to realize single photon emitters at 1.5 μm wavelengths using them.

The primary deficiency with the existing process reported in Ref. [**Pattantyus-Abraham2009]**, is that a relatively high density of nanocrystals must be exposed to the lithographically prepared cavity to ensure that at least one successfully attaches. At such high concentrations it has proven difficult to avoid undesired attachment of nanocrystals to other locations not defined by lithography. While various different chemical approaches are being

pursued to solve this problem, by getting more selective attachment at the lithographically defined site, a different method would be to enhance the selective attachment at the mode's antinode using *optical forces* to trap the nanoparticles. This is the motivation behind the work described in this thesis: the objective of the project described in this thesis is to localize a single semiconductor nanoparticle (an "artificial atom") in the high-field region of a wavelength-scale, long-lived optical microcavity using the radiation force of the cavity mode.

1.1.2. **Optical forces**

Approximately seven decades after the first experimental demonstration of optical pressure in 1901 [**Lebedov1901, Nicholls1901**], Arthur Ashkin at AT&T Bell Laboratories reported the first observation of acceleration and trapping of micron-sized latex particles using laser light [**Ashkin1986**]. He also theoretically demonstrated the possibility of trapping atoms using resonant radiation pressure of laser light [**Ashkin1970a**], which was experimentally observed in 1985 [**Chu1985, Phillips1985**]. Ashkin and his co-workers' success in trapping small micron-sized dielectric particles became the basis of what is called "optical tweezers" [**Ashkin1986**]. Optical tweezers are an invaluable tool for manipulating tiny micron-sized objects in a noncontact manner. These techniques are now applied in a variety of research fields such as chemistry, biology, and materials science. For example optical tweezers made it possible to follow the movements, forces and strains in molecular structures during a reaction [**Bustamante2000** and the references therein]. Optical tweezers can be used to measure directly the forces that hold molecular structures together. By attaching glass or latex beads to macro-molecules, it has been possible to trap them in the laser focus and do the force and position measurement directly with high accuracy. Some other applications of this technique in biology include measuring the elastic properties of DNA [**Smith1996**], characterizing the mechanical unfolding of proteins [**Kellermayer1997, Tskhovrebova1997, Onoa2003**], and measuring the force in single myosin molecules [**Finer1994**]. Note that all of these optical trapping applications involving macroscopic particles are achieved with the particles embedded in liquid environments, where buoyancy effects mean the main forces competing with the optical force are due to Brownian motion.

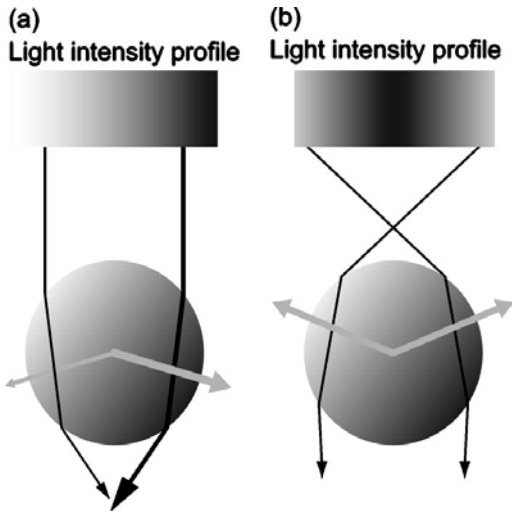

Figure 1.1 *A transparent bead in two different light intensity profiles. a) The light intensity is larger on the right hand side of the beam so the change in light momentum after refraction would be larger there than on the other side. Thicker arrows indicate larger magnitudes. b) The beam is symmetric around its center and therefore the forces on different sides of the bead would be equal and in opposite directions with respect to the symmetry axis and the bead will stay on the axis. Reprinted Figure with permission from [**Neuman2004**].*

The appropriate calculation method for estimating the radiation force depends on the size of the particles and the wavelength of the radiation. If the size of a particle is much larger than the wavelength of light, we are in the Mie regime. In this regime, the optical force can be understood using ray optics. When a transparent particle enters a tightly localized radiation field, the light rays will reflect and refract and this leads to a change in the light's momentum. From Newton's third law, the particle experiences the same amount of momentum change in the opposite direction. In a non-uniform field like a Gaussian beam, this force is towards higher light intensity regions (when the refractive index of the particle is higher than the medium). This phenomenon is illustrated in Figure 1.1. So for the case a) in Figure 1.1, the particle will be attracted towards the region with higher intensity of light (in the direction of the gradient of light intensity). But in the case b of Figure 1.1, for which the particle is at the axis of the light beam, the gradient force will be canceled out and there would only an axial force due to the refraction and scattering of light.

When the particle size is much smaller than the light wavelength (Rayleigh regime) the particle can be regarded as a point dipole (because it will be approximately uniformly polarized in the electric field of the laser light). There are gradient and scattering forces for these particles and since this is directly relevant to this project, the calculation of the Rayleigh regime force is separately given in section (2.1.1).

Traditional optical tweezers, which use focused laser light for trapping, have a common limitation. The minimum volume within which a particle can be trapped is dependent on how tightly the laser light can be focused and this is limited by diffraction. Therefore the minimum volume for trapping particles is limited to roughly a wavelength. Also, since the force is a gradient force, diffraction in a uniform medium limits the maximum magnitude of the optical force. This is particularly problematic when trying to trap small dielectric particles which have a small total polarization, and therefore require large field gradients to achieve forces large enough to overcome the Brownian forces.

One way to increase the localization of the light is by tailoring the optical and structural properties of a medium [**Mandal2009**]. For example Yang *et al* experimentally demonstrated optical trapping and transporting of dielectric nanoparticles using enhanced field confinement around a "slot waveguide" [**Yang2009**]. Since the waveguide was able to confine the light power to a very small scale (60nm), it overcame the uniform medium diffraction limitation. The evanescent field around the waveguide could attract particles as small as 75nm and the scattering/absorption force along the waveguide was exploited to propel and transport these 75 nm particles.

Some modes supported by the planer PC cavities discussed briefly above, and in detail below, have antinodes that are tightly confined at the material surface, and therefore offer potentially high field gradients, especially if a large amount of optical energy can be built up inside the cavity [**Krauss1996, Noda2000**]. The same properties that make microcavities interesting for CQED studies (high Q, small mode volume), are therefore also exactly what are required to maximize the potential optical trapping force that can be achieved at the cavity's antinode, for a given power laser [**Rahmani2006**].

1.1.3. **Thesis outline**

This thesis reports a compact optical circuit realized in the top silicon layer of a SOI wafer. The circuit is designed to trap suspended colloidal semiconductor nanocrystals at the antinode of a photonic crystal microcavity, using a 5 mW cw laser tunable from 1520 to 1630 nm. Prototype circuits have been fabricated according to the design, and the optical properties of some individual subcomponents have been successfully characterized, although a complete system has yet to be used for actual trapping experiments.

The remainder of chapter 1 provides basic technical background information relevant to the key structures used in the design of our circuit. The basic concepts that underlay microcavity design in high index dielectrics are emphasized.

Chapter 2 provides more specific theoretical background relevant to the simulation tools and analytic methods used to design the circuit. This primarily focuses on the finite difference time domain (FDTD) technique for "exactly" solving Maxwell's equations in 3D, the methods used to calculate optical forces, and some basic cavity coupling theory.

In chapter 3 we discuss all of the considerations and calculations involved in specifying the final prototype's design, including estimates for the trapping force that are expected when excited using 5 mW of cw laser power. In chapter 4, we describe the fabrication processes used to make the optical circuit described in chapter 3. These processes primarily involve electron beam lithography and plasma etching..

Chapter 5 shows images of the fabricated samples, and presents the results of experiments done to measure the Q values of the cavities (with and without coupling to waveguides), and the transmission of the input/output coupler in a solvent environment.

Chapter 6 contains conclusions and suggestions for future work.

1.2 Key Concepts: An Overview

1.2.1. **Introduction**

As stated above, the objective of the work described in this thesis was to design and fabricate an optical "circuit" in the top 200 nm thick layer of silicon on an SOI wafer, that includes a relatively high Q, small mode volume optical microcavity that can be efficiently coupled to using a fiber-coupled, cw diode laser source that is tunable between 1530 and 1620 nm. The novelty in the design has to do with the plan to operate the circuit in a solvent containing a small concentration of PbSe or PbS nanocrystals, with the intent to optically trap a single nanocrystal at the antinode of the excited cavity mode, when the cavity is resonantly excited by the tunable cw laser. Once trapped, the nanocrystal should be "self-aligned" in the optimal position to enable studies of nanocrystal-cavity-photon coupling in this material system.

One attribute of this scheme is that the design criteria for the optical circuit are essentially identical whether one considers the nanocrystal-cavity photon coupling experiment, or the optical trapping process proposed to assemble the final structure. Starting with the cavity itself, one strives for the maximum possible Q factor, and the minimum possible mode volume. For most dielectric photonic cavity designs, the Q value tends to vary in proportion to the mode volume, since light tends to leak out of 3D dielectric structures when the size shrinks below the wavelength. This leads to a design tradeoff between high Q and small V. The Q value for an isolated cavity is limited by leakage of the cavity photon to a continuum of radiation modes that, in general, carry energy away from the cavity in many different directions. This means that to *efficiently* couple light into the cavity, one has to add an additional channel (usually a 1D waveguide) to the structure in such a way that the cavity photon leaks a significant fraction of its total radiated power into that channel. There is an optimum relative coupling for this "control channel" in relation to the radiation continuum, which maximizes the energy stored in the cavity mode for a given cw level of optical power incident through the waveguide. Finally, it is necessary to couple as much power from the fiber-coupled cw laser to the 1D waveguide that interacts directly with the cavity. This is non-trivial because the typical cross section for this 1D waveguide is 200 nm×500 nm, at a wavelength of 1.5 μm. The circuit developed in this thesis

used an existing grating coupler that directs roughly 10% of the laser output into a wide, 200 nm×20 μm, multimode waveguide. A parabolic shaped "tapered waveguide" then had to be developed to couple this multimode signal into the single mode waveguide that couples to the cavity.

The following sections more fully define and describe the cavity *Q*, mode volume, and factors that must be considered when coupling the waveguide to the cavity. Examples of various cavities that have been studied in the literature are given, with specific emphasis on the planar photonic crystal cavities used in this work.

1.2.2. *Q* factor and mode volume

The *Q* factor is a parameter that shows how fast a resonator damps and is inversely proportional to the decay rate of energy in the resonator. Its definition is [**Jackson1975**]:

$$\mathrm{Q} = \frac{\omega_0 \mathrm{U}}{\mathrm{P}} \qquad 1.1$$

Here U is the total energy stored in the cavity, P is the outgoing power, and ω_0 is the angular frequency of the resonant mode.

If one plots the square of the Fourier transform of the electric field versus frequency, it would have a Lorentzian shape with a full width at half maximum (FWHM) of $\frac{\omega_0}{Q}$. This is another equivalent definition of *Q*:

$$\mathrm{Q} = \frac{\omega_0}{\Delta\omega}, \qquad 1.2$$

where $\Delta\omega$ is the FWHM of the resonant peak.

To measure the *Q* factor using our FDTD simulations in chapter 3, we used eq.1.1 and the fact that the energy stored in the cavity is decaying exponentially. If the electric field amplitude decays with a lifetime of τ, the energy stored in the cavity will have a lifetime of $\frac{\tau}{2}$. This implies that:

$$P = -\frac{dU}{dt} = \frac{2}{\tau}U \tag{1.3}$$

$$Q = \frac{\omega_0 \tau}{2} \tag{1.4}$$

where τ can be found from m, the slope of the linear envelope of the graph of $(ln\, E_i(t))$ versus time (the subscript i can represent any of the x, y, or z components of the mode's electric field, which is decaying).

$$\tau = \frac{-1}{m} \tag{1.5}$$

The cavity mode decay rate is:

$$\gamma_c = \frac{\omega_0}{2Q} \tag{1.6}$$

The other important parameter that shows how much a cavity can spatially confine light is the mode volume of the cavity. The mode volume is defined as:

$$V \equiv \frac{\int d^3\mathbf{r}\epsilon(\mathbf{r})|\mathbf{E}(\mathbf{r})|^2}{\max(\epsilon(\mathbf{r})|\mathbf{E}(\mathbf{r})|^2)} \tag{1.7}$$

To calculate the mode volume, one must find the spatial distributions of permittivity and electric field intensity of the cavity when the mode is excited. The next chapter explains how to find the mode volume using FDTD simulations.

1.3 Dielectric Microcavities

1.3.1. **Different types of optical cavities**

There have been many efforts to design different cavities with large Q/V to increase the light matter interaction. Some cavities, like microposts, or micropillar cavities (Figure 1.2), are Fabry-Perot-style and confine light with high reflectance mirrors (Bragg reflectors) [**Jewell1989, Pelton2002, Pelton2002a**] in one direction, while relying on total internal reflection in the other two directions. They have been used as single photon sources to enhance spontaneous emission [**Pelton2002a, Vahala2003**]. These cavities have maximum Q values of only a few thousands, which is limited due to the scattering by the residual roughness of the pillar sidewalls. There are another group of cavities including microspheres [**Gorodetsky1996, Vernooy1998**], microrings and microdiscs that support whispering gallery modes, which confine light based on continuous total internal reflection (Figure 1.3). They have very high Q values and moderate mode volumes. The Q factor in silica microspheres can reach to 10^9 and usually is limited by the atmospheric water absorption [**Gorodetsky1996, Vernooy1998, Cai2000**] and they have found many applications in cavity QED [**Vernooy1998a**]. In microdiscs and microrings Q values over 10^6 has been achieved, and the Q is typically limited by the sidewall roughness of the structure after the etching process [**Little1997, Borselli2004, Borselli2006**]. Since microdiscs and microrings have small mode volume and can easily be integrated monolithically on chip, they have been used extensively as building block for integrated photonic devices like add-drop filters [**Little2004, Popovic2006**], CQED [**Srinivasan2005**] and frequency conversion [**Preble2007**].

Another group of microcavities, which have attracted a great deal of attention since their concept was first introduced by Eli Yablonovitch and Sajeev John, are photonic crystal cavities [**Yablonovitch1987, John1987**]. A photonic crystal (PC) is a multidimensional periodic structure with period of the order of an optical wavelength. They are the photonic analog of an atomic lattice for electrons. The refractive index of the structure is the parameter that changes periodically and like electrons in atomic lattices, photons in photonic crystal exhibit a dispersive band structure that can include full optical band gaps under certain conditions. For optical frequencies inside the photonic band gap, propagation of light is prohibited in all directions, for any polarization.

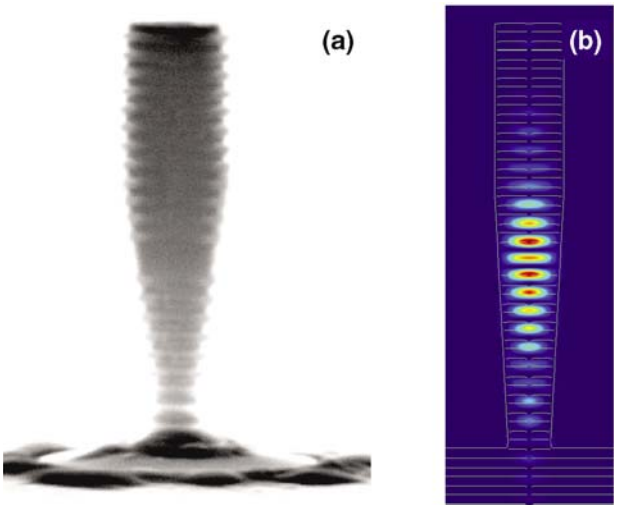

Figure 1.2 *a) Scanning-electron microscope (SEM) image of a micropost microcavity b) The profile of the electric field amplitude for the fundamental mode of the cavity. Reprinted Figure with permission from [**Pelton2002a**].*

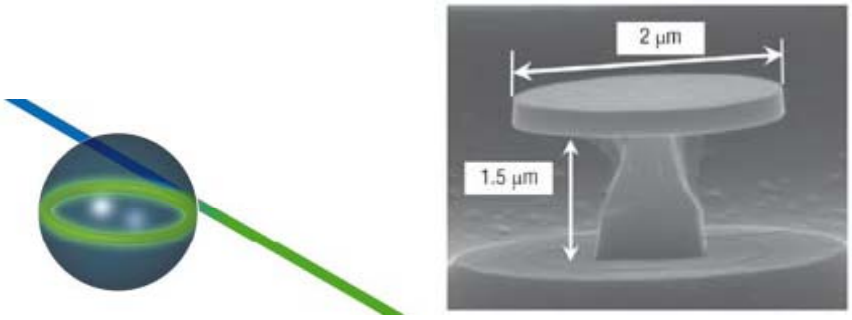

(a) *(b)*

Figure 1.3 *(a) Schematic of a silica microsphere coupled to a fiber taper waveguide. The blue shows the light coupled in and the green shows the out-coupled light that is resonant to the microsphere ($V=3000\mu m^3$). Reprinted Figure with permission from [**Vahala2003**]. (b) Scanning electron microscopy side view of a 2 μm diameter microdisk (side view). Reprinted Figure with permission from [**Peter2005**].*

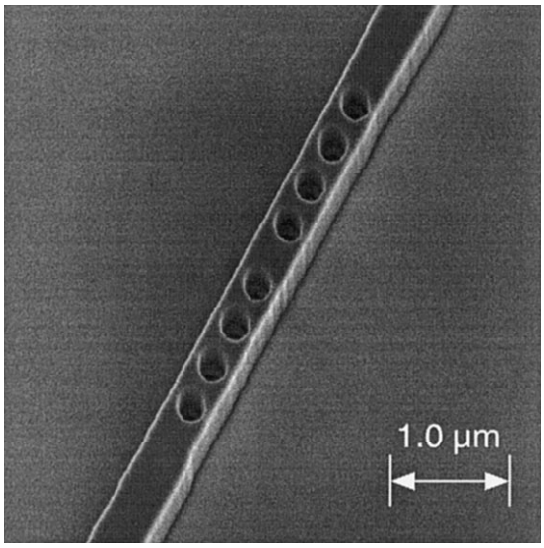

(a)

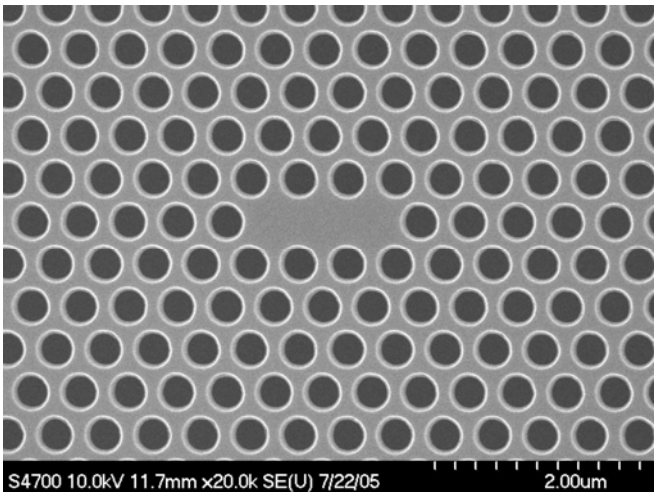

(b)

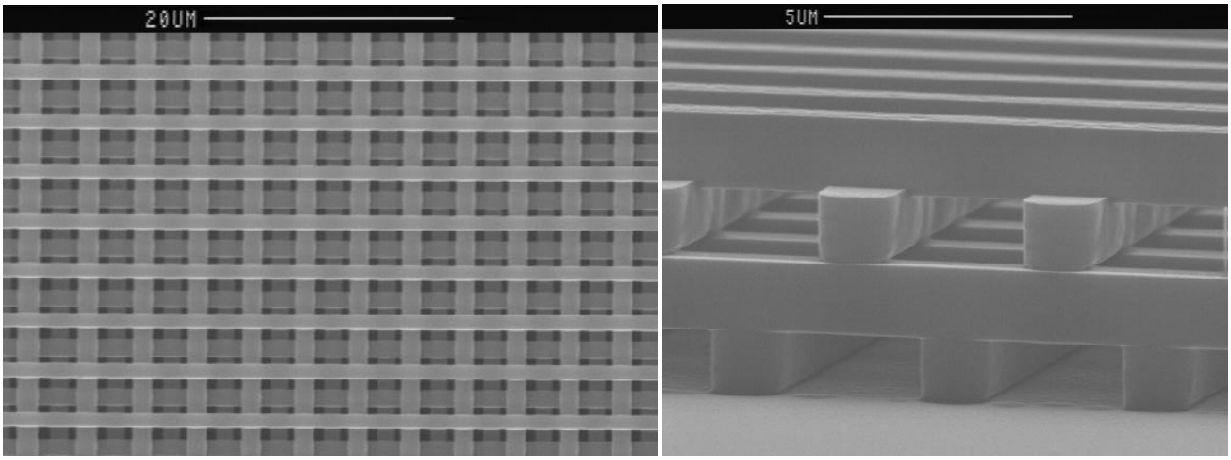

(c)

Figure 1.4 *(a) Scanning electron micrograph of a PBG waveguide microcavity fabricated by X-ray lithography. Reprinted Figure with permission from [**Foresi1997**]. (b) A 2D PC cavity made in Young's group out of silicon. The cavity consists of 3 missing holes in an* otherwise triangular lattice of air holes (this is known as an L3 cavity). (c) SEM micrographs of a 3D photonic crystal. Left image is the top view of *a completed four layer structure and the right image is the cross-sectional view of the same 3D photonic crystal. The rods are made of polycrystalline silicon. Reprinted Figure with permission from [**Lin1998**].*

A complete band gap only can happen for three dimensional (3D) photonic crystals with specific symmetries and dielectric contrast. 1D and 2D dielectric lattices can only have band gaps in

some special directions. Images of 3 different kinds of photonic crystals are illustrated in Figure 1.4.

1.3.2. **Planer PC cavities**

Among different types of PC cavities, the 2D PCs that consist of a dielectric slab with a 2D lattice of air holes are widely used because of their strong light confinement and simple fabrication [**Krauss1996, Noda2000**]. The light confinement in these cavities is the result of two different types of confinement processes. In the in-plane directions, the light wave will encounter a 2D lattice of holes and if the frequency of the light falls in the band gap of the lattice then it cannot propagate in the plane of PC. For the out of plane directions, the light will be confined by total internal reflection due to the high refractive index contrast between the slab and the background medium that is usually air. The mechanism is shown on Figure 1.5.

The PC cavities provide both extremely small mode volume ($V\sim (\lambda/n)^3$) and high Q factor, which make them as an important candidate for fundamental studies and integrated nanophotonic applications for enhanced light-matter interactions. Some of these applications include CQED [**Yoshie2004**], add-drop filters [**Takano2006**], all optical logic, low-threshold lasers [**Park2004**], enhanced optical nonlinearities [**Barclay2005**]. The work in this thesis focuses exclusively on defect states within these 2D photonic crystal cavities made in silicon membranes.

There have been extensive efforts to improve the Q factor of these cavities while keeping their mode volume approximately the same. The Q factor and the mode volume usually change proportionately. If properly designed, the main sources of intrinsic loss of the cavity mode are coupling to vertically propagating radiation modes in the surrounding vacuum (and/or solvent and/or substrate). For Fourier components of the modes that have in-plane wavevectors that lie below the light cone of the cladding ($k_{||} > \omega/nc$, where n denotes the refractive index of the cladding) there is no coupling to radiation modes, but when a mode has Fourier components with $k_{||} < \omega/nc$ there will be loss to the cladding. Shrinking of the side-holes or shifting them outward, in the L3 cavity (see Figure 1.4b), leads to the so called "gentle confinement" regime with enhancements of the Q factor [**Akahane2003, Akahane2005, Andreani2004, Srinivasan2002**] of over an order of magnitude. Through this k-space engineering of cavity modes, recently point

defect cavities with measured remarkable high Q factors (up to ~10^5) have been achieved [**Akahane2003, Akahane2005, Notomi2004, Ryu2003, Ryu2004, Tanabe2007**].

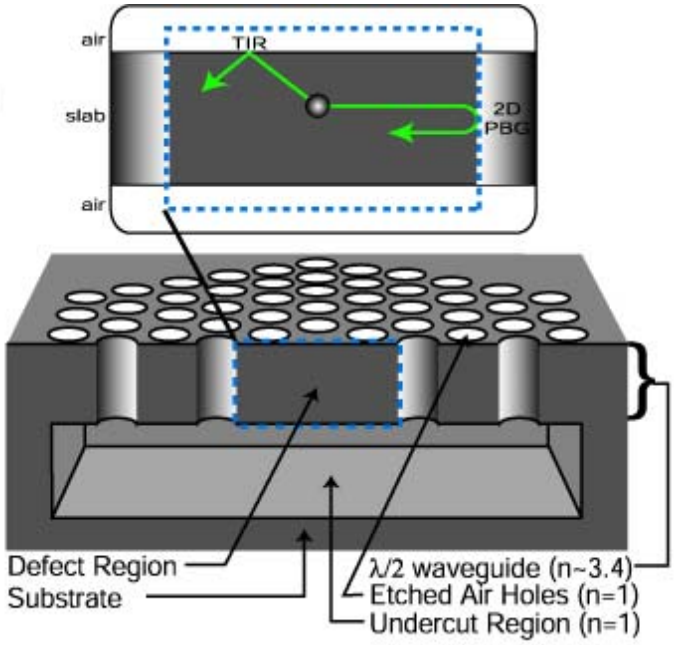

Figure 1.5 *Light confinement in 2D PC cavity. The vertical confinement is due to total internal reflection and in plane confinement is due to destructive interference of the light wave reflected from the lattice of holes.*

1.4 Efficient Coupling Of A Planer PC Cavity To PC Waveguides

1.4.1. **PC waveguides**

The other advantage of planer PC cavities is the relative ease of integrating them with low-loss one dimensional waveguides that can transport optical power to and from the cavities to other cavities, other integrated devices, or input/output couplers. Figure 1.6 shows a cavity integrated with a PC waveguide that is in turn coupled to a ridge waveguide in silicon.

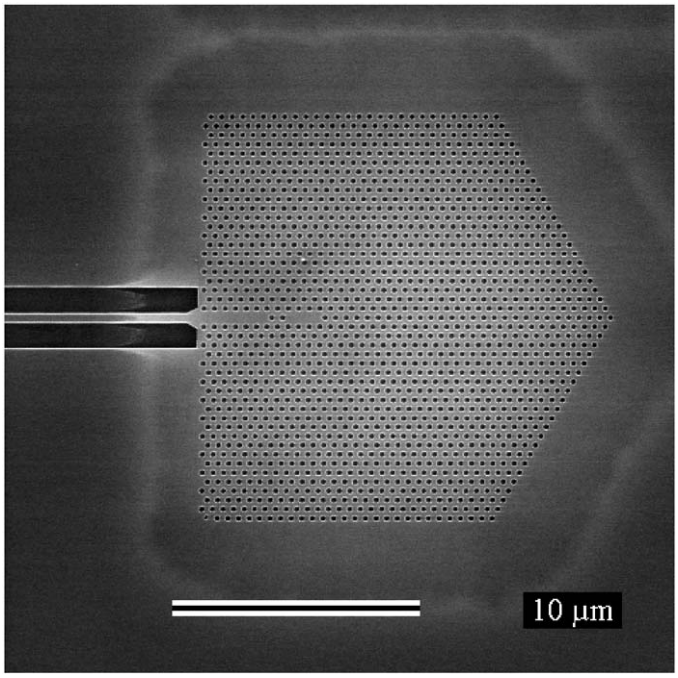

(a)

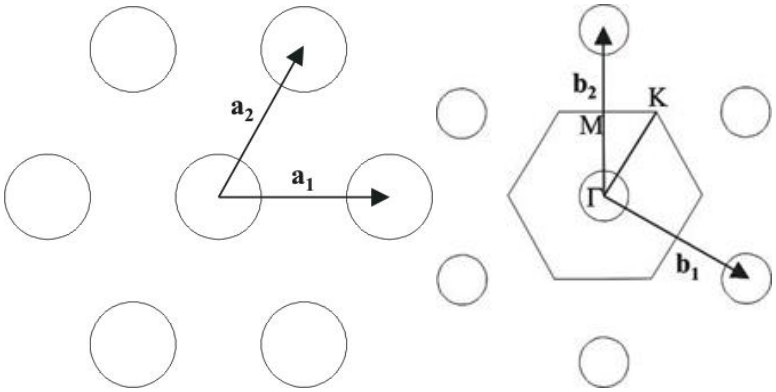

(b)

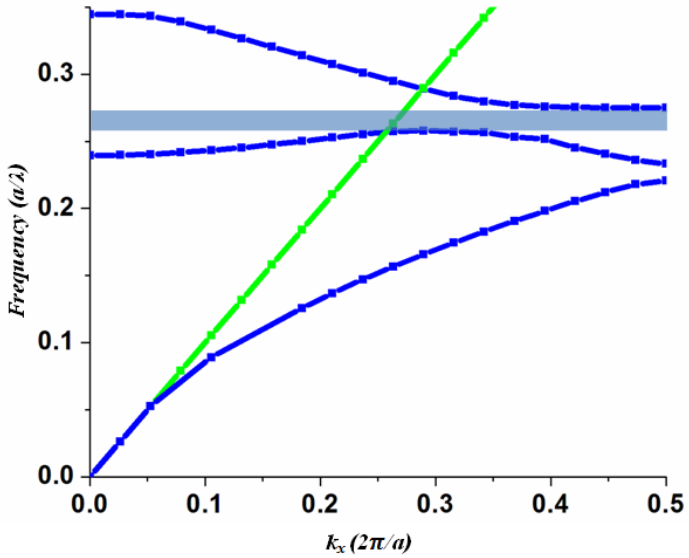

(c)

Figure 1.6 *(a) A suspended PC waveguide connected to a ridge waveguide. The PC waveguide is made out of a row of missing holes in the Γ-K direction (see the part (b) of this Figure) of a triangular lattice. Reprinted Figure with permission from [**Banaee2007**].(b) The real triangular lattice of holes and its corresponding reciprocal lattice including the lattice vectors and the Briliouin zone boundary . (c) A sample band structure for a PC waveguide showing the lightline (green) and the first 3 bands of the band structure. a is the pitch of the PC waveguide in the Γ-K direction. k_x is the wave vector in the Γ-K direction for the structure shown in part (b) of this Figure. 0.5 in kx axis is the Brillouin zone boundary (point K).*

To maintain a high Q for a planar photonic crystal cavity in silicon, it has to be surrounded typically by at least 10 rows or rings of holes. The waveguide in direct "contact" with the cavity thus has to be implemented in the PC: it must be a photonic crystal waveguide. It is usually desirable to minimize the propagation distance in PC waveguides that are relatively lossy compared to ridge waveguides, hence the basic cavity-PC waveguide-ridge waveguide structure as shown in Figure 2.5. The simplest 1D PC waveguide are made by leaving out one row of holes in a PC lattice, as in Figure 2.5.

For PC waveguides it should be noted that near to the Brillouin zone boundaries the group velocity of the guided modes goes to zero (Figure 1.6c). Small group velocity waveguide modes are known to be very lossy, even when they fall below the lightlines, due to fabrication

imperfections. There are various strategies for modifying the band structure to increase the group velocity over as wide a range as possible below the light line [**Grillet2003**, **Yamada2001, Kim2004**]. One of these strategies was changing the radius of the nearest neighbor holes to the PC waveguide to shift its band structure up or down. In the next chapter, it will be explained how this modification changes the band structure and the transmission efficiency and its reason.

1.4.2. **PC waveguide-cavity coupling**

Once the highest possible "intrinsic" Q value for an *isolated* planar PC cavity has been achieved, a PC waveguide has to be integrated with the cavity in such a way as to maximize the amount of optical energy stored in the cavity for a given optical power incident in the waveguide [**Ryu2003, Notomi2004, Mitsugi2003, Kim2004, Chutinan2001, Kim2004**]. Optimization of the energy inside the cavity was done according to Temporal Coupled-Mode Theory [**Fan2004**]. In the following, we identify the intrinsic Q of the isolated cavity, due to vertical coupling out via a continuum of radiation modes in all directions, as Q_v, and the Q due to power coupled out of the cavity to the purposely introduced waveguide, as Q_w. The following calculation is a specific case of a more general derivation that can be found in Chapter 10 of [**Joannopoulos2008**].

A schematic of the cavity and the PC waveguides is shown in Figure 1.7. $S_{1\pm}$ and $S_{2\pm}$ are proportional to the mode amplitudes inside the waveguides. $\|S_{1+}\|^2$, $\|S_{2+}\|^2$ are equal to the power of the modes going into the cavity through the left and right PC waveguides, respectively, and $\|S_{1-}\|^2$, $\|S_{2-}\|^2$ are the powers inside the waveguides that are going away from the cavity. It is assumed that the couplings between waveguides and the cavity are weak, and also that the cavity energy can only leak into these two waveguides or dissipate in the out-of-plane direction. τ_1 and τ_2 are the decay lifetimes of the cavity mode into the waveguides, which are equal because of the symmetry of the design. Also τ_v is the vertical decay lifetime of the cavity mode in the out-of-plane direction. The total lifetime of the cavity mode is therefore given by:

$$\frac{1}{\tau} = \frac{1}{\tau_1} + \frac{1}{\tau_2} + \frac{1}{\tau_v} = \frac{1}{\tau_w} + \frac{1}{\tau_v}, \qquad 1.8$$

where τ_w is the total decay lifetime into the waveguides.

Thus, using eq.1.8, the relation between the total Q and Q_v, Q_W is:

$$\frac{1}{Q} = \frac{1}{Q_w} + \frac{1}{Q_v} \qquad 1.9$$

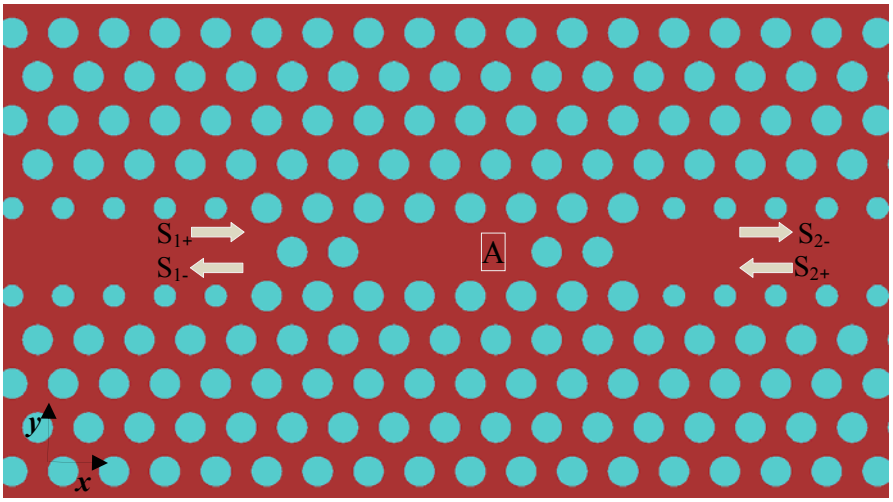

Figure 1.7 *The simulation layout of an L3 cavity, placed in between two photonic crystal waveguides (one on each side).* $\|S_{1\pm}\|^2$ *and* $\|S_{2\pm}\|^2$ *are the input and the output power in the waveguides and* $\|A\|^2$ *gives the energy inside the cavity.*

By assuming weak coupling and using conservation of energy, the following relations were found [**Joannopoulos2008**]:

$$\frac{d}{dt}A = -i\omega_0 A - A\left(\frac{1}{\tau_v} + \frac{1}{\tau_w}\right) + \sqrt{\frac{1}{\tau_w}}S_{1+} + \sqrt{\frac{1}{\tau_w}}S_{2+} \qquad 1.10$$

$$S_{1-} = -S_{1+} - \sqrt{\frac{1}{\tau_w}}A \qquad 1.11$$

$$S_{2-} = -\sqrt{\frac{1}{\tau_w}}A \qquad 1.12$$

ω_0 in eq.1.10 is the mode frequency. Since in our design we have assumed that the left waveguide is the input channel then, S_{2+} is zero. In the steady state, when the input power is in resonance with the cavity mode ($\omega=\omega_0$), we will have:

$$|A| = \sqrt{\frac{2}{\omega_0}} \frac{Q}{\sqrt{Q_w}} |S_{1+}| \qquad 1.13$$

Therefore to maximize the energy stored in the cavity for a specific input power, we have to maximize $\sqrt{\frac{2}{\omega_0}} \frac{Q}{\sqrt{Q_w}}$.

The result is that for a specific Q, when

$$Q_v = Q_w \qquad 1.14$$

$\frac{Q}{\sqrt{Q_w}}$ is maximized, and therefore the radiation forces would be maximized.

Thus, the cavity-PC waveguide design should satisfy this condition (eq. 1.14). This condition also optimized the transmittance from input PC waveguide to the output PC waveguide (eq. 1.15) [**Notomi2004, Mitsugi2003, Kim2004**], which should assist in optically characterizing the device. The optimum transmittance is 25%.

$$\frac{Q^2}{Q_w{}^2} \qquad 1.15$$

Recall that Q_v should be first, independently maximized to reduce the power loss in to the solvent, and then the coupling to the PC waveguide should be set so Q_w equals Q_v.

CHAPTER 2 RADIATION FORCE

2.1 Radiation Force Calculations

As mentioned in sub section 1.1.2, the relatively high degree of spatial field confinement for modes supported by PC cavities means there can potentially be a high gradient of electromagnetic field intensity if one can couple sufficient energy into the cavity mode. The question is whether the absolute field gradients can be large enough that associated optical "gradient forces" are sufficiently strong to overcome random forces exerted on particles in solution, and thus allow optical trapping of small particles at the antinode of the cavity mode.

Since the QDs we plan to trap are much smaller than the wavelength of photons in the cavity, it should be a good approximation to treat them as point dipoles that don't modify the cavity field very much (see subsection 1.1.2). Below we briefly review the "dipole approximation" approach to estimating the optical force exerted on a small polarizable dielectric particle in the presence of an inhomogeneous electromagnetic field, and then also outline the more general (and time-consuming) method that involves integrating the Maxwell stress tensor evaluated by including the particle in the self-consistent calculation of the electromagnetic field. The results of these two approaches are compared in Chapter 3.

2.1.1. **Dipole approximation**

In the Rayleigh regime, which applies to particles with sizes much smaller than the electromagnetic field's wavelength (Rayleigh particles), polarizable particles can be

approximated as point dipoles. In this regime the effect of the particle on its surrounding electric field is neglected. The radiation force on a dipole is given by [**Novotny2006**]:

$$\mathbf{F}(\mathbf{r},\mathrm{t}) = (\mathbf{p}(\mathbf{r},\mathrm{t})\cdot\nabla)\mathbf{E}(\mathbf{r},\mathrm{t}) + \frac{\mathrm{d}}{\mathrm{dt}}[\mathbf{p}(\mathbf{r},\mathrm{t})\times\mathbf{B}(\mathbf{r},\mathrm{t})]\,, \qquad 2.1$$

where $\boldsymbol{F}(\boldsymbol{r},t)$ is the total dipole force, $\boldsymbol{p}(\boldsymbol{r},t)$ is the dipole moment of the particle, and $\boldsymbol{E}(\boldsymbol{r},t)$ and $\boldsymbol{B}(\boldsymbol{r},t)$ are the electric and magnetic fields, which are functions of position and time. If the polarization is linearly proportional to electric field, $\boldsymbol{p}(\boldsymbol{r},t) = \alpha\boldsymbol{E}(\boldsymbol{r},t)$, the force is:

$$\mathbf{F}(\mathbf{r},\mathrm{t}) = \alpha(\mathbf{E}(\mathbf{r},\mathrm{t})\cdot\nabla)\mathbf{E}(\mathbf{r},\mathrm{t}) + \alpha\frac{\mathrm{d}}{\mathrm{dt}}[\mathbf{E}(\mathbf{r},\mathrm{t})\times\mathbf{B}(\mathbf{r},\mathrm{t})] \qquad 2.2$$

Assuming time harmonic electromagnetic fields, the second term in eq. 2.2 vanishes after time averaging over several optical cycles. This term corresponds to the radiation pressure (scattering plus absorption forces) due to the change in the momentum of the incident light. Thus after averaging, we end up with [**Novotny2006**]:

$$\langle\mathbf{F}(\mathbf{r},\omega)\rangle = \frac{\alpha'(\omega)}{4}\nabla{\mathrm{E}_0}^2(\mathrm{r},\omega) + \frac{\alpha''(\omega)}{2}{\mathrm{E}_0}^2\nabla\phi(\mathrm{r})\,, \qquad 2.3$$

where the electric is assumed to have the form of:

$$\mathbf{E}(\mathbf{r},\mathrm{t}) = \mathbf{E_0}(\mathbf{r},\omega)\mathrm{e}^{\mathrm{i}(\phi(\mathrm{r})-\omega\mathrm{t})} \qquad 2.4$$

and, where α' and α'' are the real and imaginary parts of the polarizability. The first term of eq. 2.3 corresponds to the gradient of intensity which is also known as the dipole term. This part of the force comes from the interaction between the external electric field and the induced dipole moment of the particle. The second term, which corresponds to the dissipative part of the polarizability, results from transfer of momentum of light to the particle (usually known as scattering force). In the case of lossless particles or standing waves (the case that corresponds to PC cavity modes) the second term in eq. 2.3 vanishes and the average scattering force is zero.

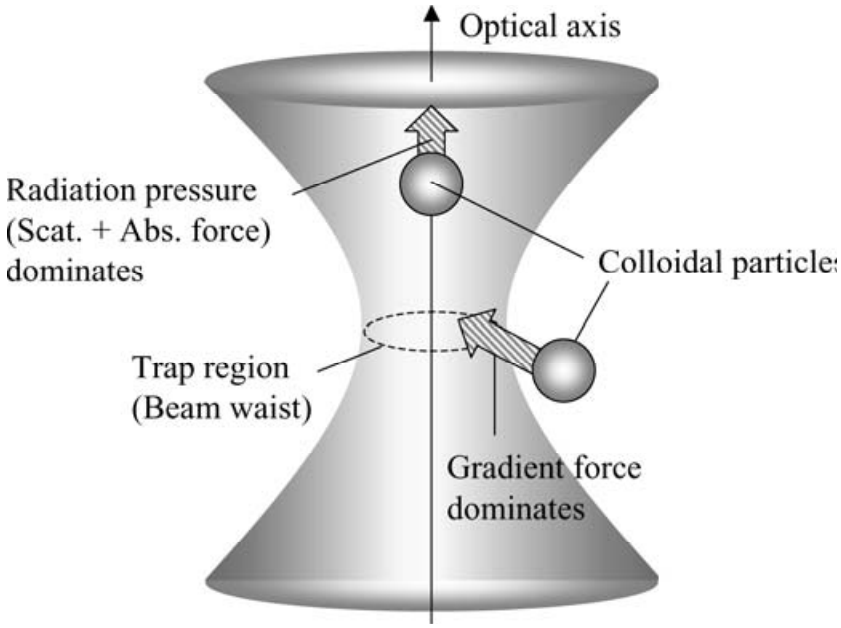

Figure 2.1 *Different contributions to the radiation force are illustrated. The gradient force (1st term of eq. 2.3) attracts particle to the highest intensity position and the scattering force (the 2nd term in eq. 2.3) exerts force in the direction of the beam propagation. Reprinted Figure with permission from [**Iida2008**].*

This is one advantage of standing waves over propagating waves, because the scattering force can move the particle out of the stable trapping point defined by the dipole term (i.e. the point with highest intensity). To approximate the force on a particle in the PC cavity using this dipole approximation, we need to know the polarizability of the particle to be trapped, and the spatial distribution of the electric field for a given excitation of the PC cavity mode, as calculated in the absence of the particle.

As mentioned above, in this approximation, the influence of the point dipole on the external fields is not included. To take this influence into account, another calculation method was used, which is going to be explained in the next section.

2.1.2. **Radiation force calculation using the Maxwell Stress Tensor (MST)**

The rigorous method of calculating the force on a particle in an electromagnetic field involves self-consistently evaluating the total field distribution including the particle, and then

integrating the "Maxwell Stress Tensor" over a surface surrounding the particle, as explained below.

The Lorenz force acting on a charge q at the position $\boldsymbol{r}$ moving with the velocity $\boldsymbol{v}$ in the electromagnetic fields, $\boldsymbol{E}$ and $\boldsymbol{B}$, is given by:

$$\mathbf{F}(\mathbf{r},\mathrm{t}) = \mathrm{q}[\mathbf{E}(\mathbf{r},\mathrm{t}) + \mathbf{v}(\mathbf{r},\mathrm{t}) \times \mathbf{B}(\mathbf{r},\mathrm{t})] \quad 2.5$$

For a group of induced charges (due to polarization in the field) inside the nanoparticle the force would be:

$$\mathbf{F}(\mathbf{r},\mathrm{t}) = \int [\rho(\mathbf{r},\mathrm{t})\mathbf{E}(\mathbf{r},\mathrm{t}) + \mathbf{j}(\mathbf{r},\mathrm{t}) \times \mathbf{B}(\mathbf{r},\mathrm{t})]\mathrm{dv} \quad 2.6$$

From Maxwell equations we can write:

$$\nabla \times \mathbf{E} \times \epsilon_0\mathbf{E} = -(\frac{\partial \mathbf{B}}{\partial \mathrm{t}}) \times \epsilon_0\mathbf{E} \quad 2.7$$

$$\nabla \times \mathbf{B} \times \mu_0\mathbf{H} = [\frac{1}{\mathrm{c}^2}\left(\frac{\partial \mathbf{E}}{\partial \mathrm{t}}\right) + \mu_0\mathbf{J}] \times \mu_0\mathbf{H} \quad 2.8$$

Now we add eqs. 2.7. and 2.8:

$$\epsilon_0(\nabla \times \mathbf{E}) \times \mathbf{E} + \mu_0(\nabla \times \mathbf{H}) \times \mathbf{H} = -\frac{1}{\mathrm{c}^2}\left(\frac{\partial \mathbf{H}}{\partial \mathrm{t}}\right) \times \mathbf{E} + \frac{1}{\mathrm{c}^2}\left(\frac{\partial \mathbf{E}}{\partial \mathrm{t}}\right) \times \mathbf{H} + \mathbf{J} \times \mathbf{B} \quad 2.9$$

The two terms on the LHS of eq. 2.9 can be written as:

$$\epsilon_0(\nabla \times \mathbf{E}) \times \mathbf{E} = \nabla \cdot \left(\epsilon_0\mathbf{E}\mathbf{E} - \frac{\epsilon_0}{2}\mathrm{E}^2\overleftrightarrow{\mathbf{I}}\right) - \epsilon_0\mathbf{E}(\nabla \cdot \mathbf{E}) \quad 2.10$$

$$= \nabla \cdot \left(\epsilon_0\mathbf{E}\mathbf{E} - \frac{\epsilon_0}{2}\mathrm{E}^2\overleftrightarrow{\mathbf{I}}\right) - \rho\mathbf{E}\,, \quad 2.11$$

where $\boldsymbol{EE}$ denotes the outer product and $\overleftrightarrow{\boldsymbol{I}}$ denotes the unit tensor.

Similarly,

$$\mu_0(\nabla \times \mathbf{H}) \times \mathbf{H} = -\nabla \cdot \left(\mu_0 \mathbf{HH} + \frac{\mu_0}{2} \mathrm{H}^2 \overleftrightarrow{\mathbf{I}}\right) \quad 2.12$$

Thus, eq. 2.9 can be written as:

$$\nabla \cdot \left(\epsilon_0 \mathbf{EE} - \mu_0 \mathbf{HH} - \frac{1}{2}(\epsilon_0 \mathrm{E}^2 + \mu_0 \mathrm{H}^2) \overleftrightarrow{\mathbf{I}}\right) = \rho \mathbf{E} + \frac{1}{c^2}\left(\frac{\partial(\mathbf{E} \times \mathbf{H})}{\partial t}\right) + \mathbf{J} \times \mathbf{B} \quad 2.13$$

The Maxwell stress tensor (MST) is defined as (in vacuum):

$$\overleftrightarrow{\mathbf{T}} = \epsilon_0 \mathbf{EE} - \mu_0 \mathbf{HH} - \frac{1}{2}(\epsilon_0 \mathrm{E}^2 + \mu_0 \mathrm{H}^2) \overleftrightarrow{\mathbf{I}} \quad 2.14$$

If we integrate eq. 2.14 on an arbitrary volume that contains all sources ρ and $\boldsymbol{J}$ and use Gauss' integration law, we find:

$$\int \overleftrightarrow{\mathbf{T}} \cdot \mathbf{n}\, \mathrm{da} = \int (\rho \mathbf{E} + \mathbf{J} \times \mathbf{B})\, \mathrm{dv} + \frac{1}{c^2} \frac{\mathrm{d}}{\mathrm{dt}} \int (\mathbf{E} \times \mathbf{H})\, \mathrm{dv} \quad 2.15$$

On the RHS, the first term is the force that we are looking for and the second term is the force carried by the field momentum which is zero when averaged over a few optical cycles [**Iida2008**].

So the final form of eq. 2.6 after averaging is:

$$\int \langle \overleftrightarrow{\mathbf{T}} \rangle \cdot \mathbf{n} \mathrm{da} = \langle \mathbf{F} \rangle \quad 2.16$$

Thus, to rigorously find the radiation force on the nanoparticle we should define a closed surface surrounding the nanoparticle and then integrate the MST on this closed surface. The result will be the average force on the nanoparticle. In the case of colloidal nanoparticles in a solvent (relevant to this work), the MST should is slightly modified as:

$$\overleftrightarrow{\mathbf{T}} = \epsilon \mathbf{EE} - \mu \mathbf{HH} - \frac{1}{2}(\epsilon E^2 + \mu H^2)\overleftrightarrow{\mathbf{I}}, \quad 2.17$$

where ϵ is the dielectric permittivity and μ is the permeability of the liquid medium surrounding the particle.

In chapter 3, the FDTD solver is used to find the exact electromagnetic field distribution in the vicinity of a microcavity, including the presence of the particle, and the MST is integrated to find the net optical force for a given energy stored in the cavity mode. The result is compared with that obtained using the dipole approximation described in the previous section.

CHAPTER 3 OPTICAL CIRCUIT DESIGN

3.1 Introduction

Prototyping a complex photonic structure before fabrication is a critical step to limit the range of parameters that need to be explored in the fabricated devices. Modern computers allow the accurate numerical solution of Maxwell's equations in nanometer-textured structures, at near infrared wavelengths, over volumes of order a thousand cubic micrometres. One of the most common methods employs a finite difference time domain (FDTD) approach, originally proposed by Yee in 1966 [**Yee1966, Pelton2002**]. The technique is discrete in both space and time. The whole simulation region is divided into discrete unit cells, called Yee cells [**Yee1966**]. The electric field components are solved in one cell at an instant of time and recorded in the computer memory. Then the corresponding magnetic field components are found in the same cell. By doing this process over and over in all Yee cells one can find the electromagnetic field components at any point of time over the entire simulation region. The commercial FDTD software which was used in this work is from "Lumerical FDTD Solutions". Using this software we were able to characterize all essential properties of our cavity and waveguide designs, including resonant cavity frequencies, their Q values and mode volumes, and the coupling efficiencies between different parts of a structure, the dispersion of waveguide modes, the net transmission through the entire structure, and ultimately the expected radiation force on particles near the antinode of the excited cavity.

The objective of the current design was to couple radiation from a tunable cw fibre-coupled laser (power level ~ 5 mW), as efficiently as possible into a "high" Q PC microcavity in order to achieve as the highest possible field-gradient optical trapping force at the main antinode

of the cavity mode. The strategy involved using pre-existing, relatively efficient gratings to couple the cw laser into and out of 20 micron wide, multimode waveguides, ~ 1 mm long, in the top, ~200 nm thick silicon layer of the SOI wafer. The PC cavity thus had to be fabricated in the middle of this 20 micron wide waveguide, and the multimode waveguide had to be adiabatically coupled to a single mode waveguide that interacted directly with the PC cavity.

Previously in Young's group, a student [**Banaee2007**] had designed and tested a related structure that included a PC cavity efficiently coupled to a single mode silicon waveguide that was in turn adiabatically coupled to a grating coupler (see Figure 3.1). That structure was optimized to work in air. Since the optical trapping of particles can only be achieved in solution, Banaee's design had to be significantly redesigned to work in a dielectric background of n ~1.44, versus n ~1. This chapter describes the steps involved in redesigning Banaee's structure to operate with the pre-existing grating couplers, in a solution environment.

3.2 Initial Design

3.2.1. **Banaee's design**

The geometry shown in Figure 3.1 was proposed by Banaee *et al* [**Banaee2007**] as a method for efficiently coupling energy in a PC cavity mode out to a silicon ridge waveguide in SOI. The 2D PC cavity consisted of 3 missing holes in a triangular lattice of holes (known as an L3 cavity [**Akahane2003**]). The pitch of the lattice was a = 420nm and the radius of the holes in the PC lattice was $r = 0.29a$. The entire PC was freestanding (undercut). The cavity was coupled to a PC waveguide which was made by removing (not patterning) 6 holes from the lattice in the Γ-K direction of the lattice. This PC waveguide was connected to a grating coupler by a combination of ridge and tapered waveguide (Figure 3.1). Laser light was used to directly pump the cavity and the light coupled into the cavity mode was guided by the waveguides (i.e. PC, ridge and tapered waveguides) to the grating coupler and then it was out-coupled for monitoring purposes. The width of the ridge waveguide was $d = 0.974a$ and the length of it was 10 μm. The length of the tapered waveguide was 30 μm. The grating coupler included a rectangular lattice of

air holes with radius of 244nm. The pitch of the lattice parallel to the waveguides axis was $a_{\parallel}$= 795nm and in the perpendicular direction was $a_{\perp}$= 750nm.

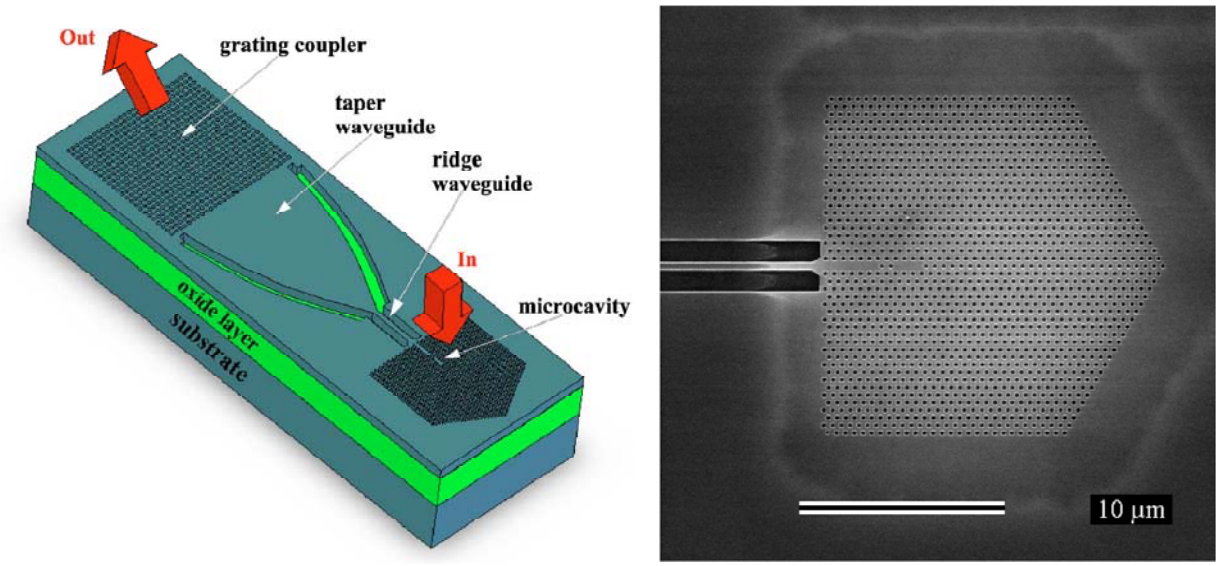

(a) *(b)*

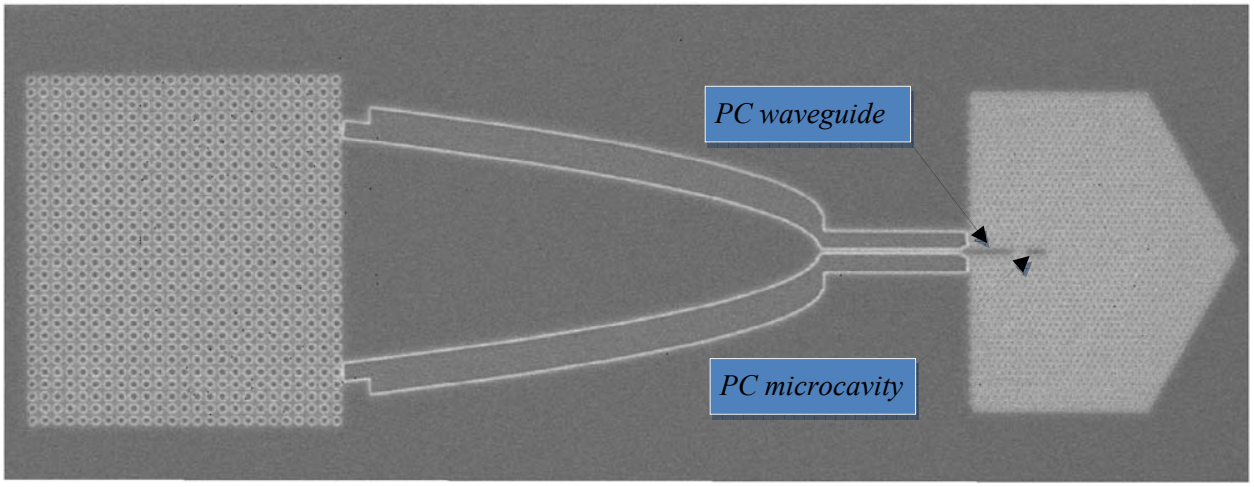

(c)

Figure 3.1 *(a) A schematic of the structure used by Banaee et al for measuring the coupling between PC cavity and the ridge waveguide. All features except the substrate are to scale. (b) The SEM image of the fabricated microcavity by Banaee (c) An SEM image of the top view of the fabricated sample by Banaee showing how the cavity and the waveguides and grating coupler are located. Reprinted Figure with permission from [**Banaee2007**].*

The silicon slab has thickness of t=196 nm and it is on top of a 1 μm thick layer of SiO2. The entire structure exists on top of a 1 mm thick silicon substrate.

3.2.2. **Essential modifications to Banaee's design for trapping purposes**

There were two reasons that made modifications unavoidable. The original (Banaee's) structure was designed so that the cavity region could be excited from free space. This limits the excitation efficiency of the mode, and also leads to additional fields in the cavity that in the current application would exert a complicated, extra force on the nanoparticle. In addition, the trapping experiment is done in a liquid environment (a solvent), not in air, so the structure had to be modified to support a high-quality mode at the correct frequency in a solvent dielectric environment.

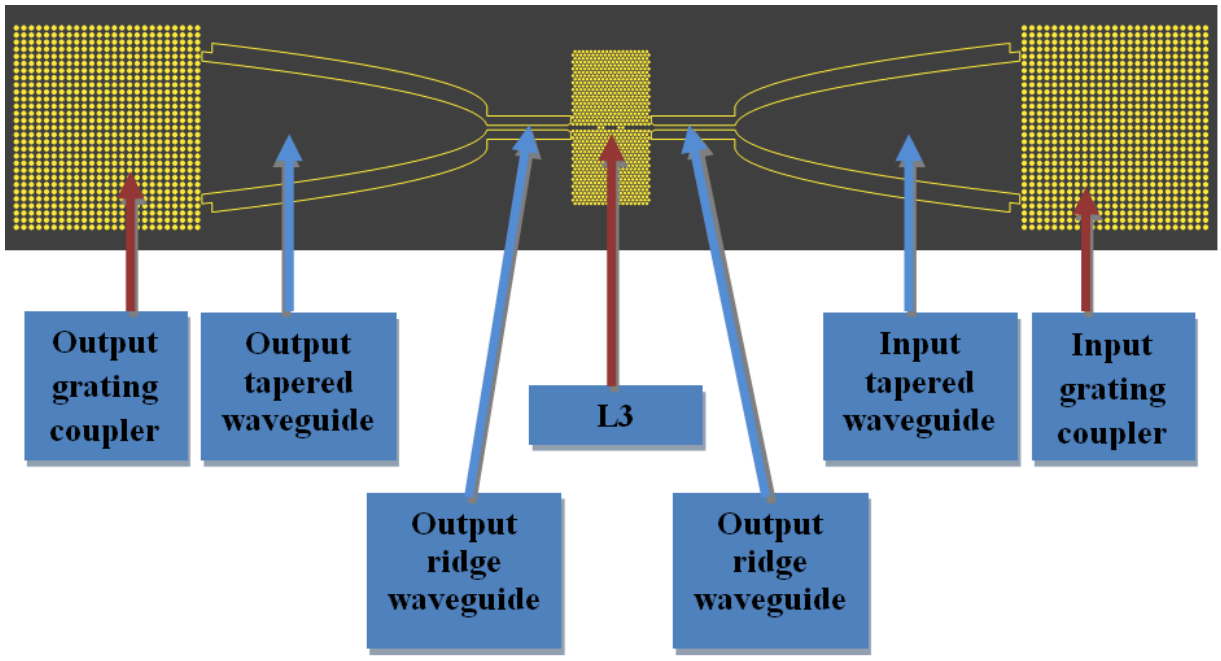

Figure 3.2 *The new design for coupling light in and out of PC cavity (top view). The laser light is coupled to the microcavity through an input grating coupler and three waveguides in series. The light is out-coupled from the cavity through monitored symmetric geometry on the other side of the cavity*

3.3 Characterization Of The Initial Design In A Liquid Medium

3.3.1. **L3 cavity fundamental mode resonance**

In the next step, the cavity resonant frequency and the transmission from the entrance to the exit waveguides were examined both in air and after adding a solvent to the system. The calculations were done using the FDTD method using "Lumercial FDTD Solutions'" software. Initially, two simulations were run to find the shift in the cavity resonance. The structure simulated is shown schematically in Figure 3.4.

The get the most accurate results, the mesh cell size should be chosen so there are an integer number of cells within each period of the lattice. For example in the simulations corresponding to Figure 3.6, there are 40 mesh cells per a (the period of the lattice along *x* axis) and 40 cells per $\frac{\sqrt{3}}{2}a$ (the period of the lattice along *y* axis). All dimensions used in the simulations are given in Table 3.1. In this way the structure is completely periodic in both *x* and *y* directions. In the *z* direction the mesh size was selected to be 9.8 nm so that there would be an integer number of mesh cells inside the silicon slab with thickness of 196 nm. This also helps the accuracy of the simulation results. The other point that is important is the size of the whole simulation region, which should be determined to have exactly an integer number of mesh cells along each axis. For example in this simulation we used a simulation region size of $20a \times 20\frac{\sqrt{3}}{2}a \times 10t$. These conditions all together guarantee the periodicity of the structure being simulated.

Figure 3.3 shows the calculated resonance frequency of the lowest energy, highest Q, fundamental mode of a cavity defined by the parameters in Table 3.1, in a background dielectric of air (Figure 3.3 a), and a solvent with refractive index 1.445 (Figure 3.3). The mode frequency was shifted from 1522nm to 1570nm. These particular simulations were done with a relatively fine mesh size (see Table 3.1) to accurately find the absolute frequencies and the shift due to the solvent (a ~ 48 nm red shift). Even with the shift due to the solvent, the cavity mode frequency falls within the excitation laser's tunable range (between 1520 and 1630 nm), so there was no need to modify the background PC lattice parameters.

Table 3.1 *The simulation parameters for investigating the consequences of changing the background medium from air to a solvent.*

Case #	***Pitch of the lattice(nm)***	***Lattice hole radius***	***Mesh cell dimensions***	***background refractive index***
1	*a=420*	*r=0.3a*	*(0.025a, 0.025a$\frac{\sqrt{3}}{2}$, 0.05t)*	*n=1*
2	*a=420*	*r=0.3a*	*(0.025a, 0.025a$\frac{\sqrt{3}}{2}$, 0.05t)*	*n=1.445*

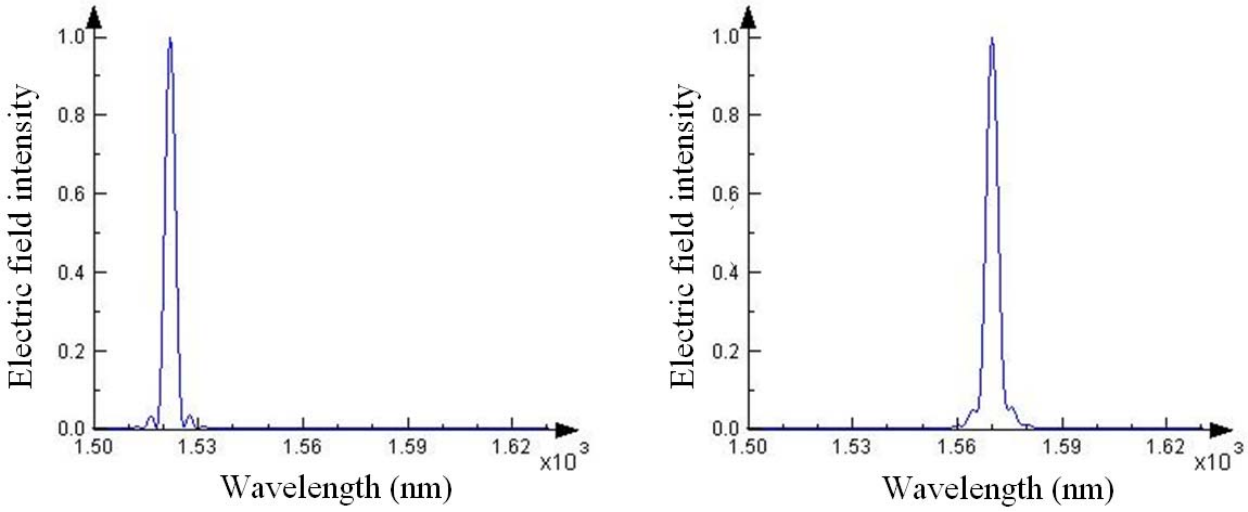

(a) *(b)*

Figure 3.3 *The resonant frequencies of the fundamental mode of the L3 cavity in two different media are shown. a) In air (Case # 1 in Table 3.1). The wavelength of the mode is λ_{Air} =1522nm b) In a solvent (Case # 2 in Table 3.1). The wavelength of the mode is, $\lambda_{Solvent}$ =1570nm. Both simulations were done for freestanding structures using the hole sizes and patterns described in Table 3.1. These spectra are not completely resolved.*

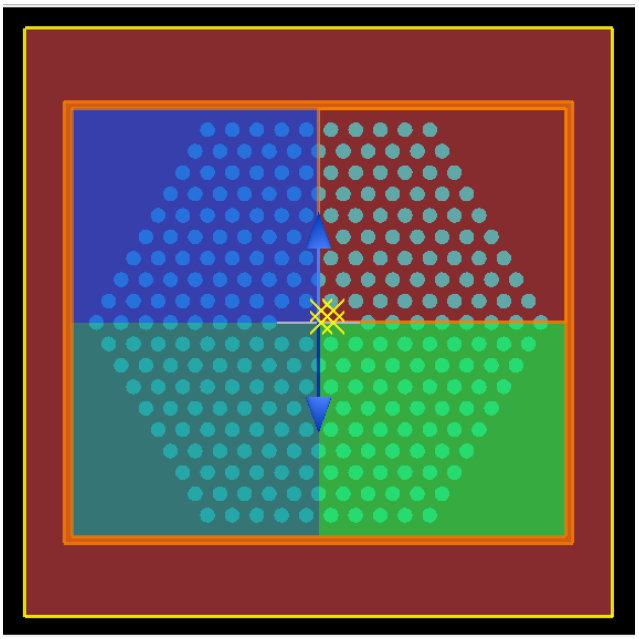

(a)

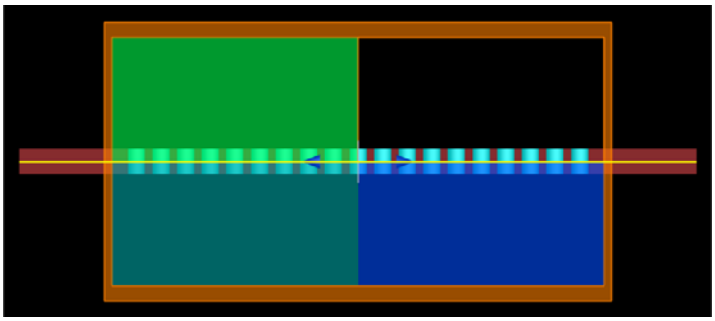

(b)

Figure 3.4 *This Figure shows the simulation layout for measuring the Q factor and the resonant frequency of an L3 cavity with structure properties, listed in Table 3.1. (a) The xy plane (Top view) of the structure shows the simulation region (orange box), a electric dipole source (the blue arrow), time monitors (yellow cross marks), 2D index and profile (DFT) monitors (the yellow box that is actually the two monitors overlapped on each other). The blue arrow shows the polarization direction of the source (the middle of this arrow shows the position of the source). (b) The zx plane (side view) of the design. The yellow line shows the index and DFT monitors placed at the middle of the silicon slab to collect data at the plane with highest mode intensity. Because of the symmetry boundary conditions that were imposed on x and y and z axes 7/8 of the whole simulations region is in color (green and/or blue) and the software only calculate the fields in 1/8 of the simulations region and uses the boundary condition to find the fields in the rest of the simulation region.*

The electric field of the fundamental mode of the L3 cavity is symmetric around the *y* and *z* axes and anti-symmetric around the *x* axis. This can be incorporated in the simulations using "symmetry boundary conditions", which helps to decrease the time and memory required by the simulation: the total time of a simulation decreases by a factor of 2 for each symmetry boundary condition used. To excite the mode, we used an electric dipole source that was polarized along the *y* axis, located at the centre of the cavity. This allowed efficient and selective coupling to the cavity's fundamental mode (look at Figure 3.6a for the intensity profile of the mode in *xy* plane).

3.3.2. **Q factor of the L3 cavity**

To find the Q factor of cavities, we used eq. 1.4 ($Q = \frac{\omega_0 \tau}{2}$) and the slope of the linear envelope of the logarithmic electric field decay graph. An example of this method is shown in Figure 3.5. For multimode cavities, there will be interference beats in the data collected by the time monitors, which makes it hard to measure the slop *s* for each mode accurately. There were two methods to overcome this problem. In the first method, we set some symmetry filters in the software by defining the boundary conditions at symmetry planes. For example, in Figure 3.5 the x=0 and z=0 planes have symmetric boundary conditions but y=0 plane has anti-symmetric. Using all of these symmetry conditions, we omitted all localized modes of the cavity except the fundamental mode. If two modes have exactly the same symmetry, the symmetry filters will fail to work. In that case, one can use long excitation-pulse duration to isolate a specific mode. Long pulses have very narrow spectral widths. They enable the user to isolate modes separated by more than their line-widths. The other method was using a helpful feature in Lumerical software called "analysis group" that does all the Q calculation automatically by running a script file. It consists of a group of point time monitors and the script file. The monitors are placed at multiple locations in the cavity to pick up *some* signal from all modes. The script file use Gaussian filters to isolate all of the resonant peaks in the Fourier Transform of the signal and then, to find the slope and Q factor for each mode, it multiplies the Fourier transform of the field signal by the Gaussian filter corresponding to that mode.

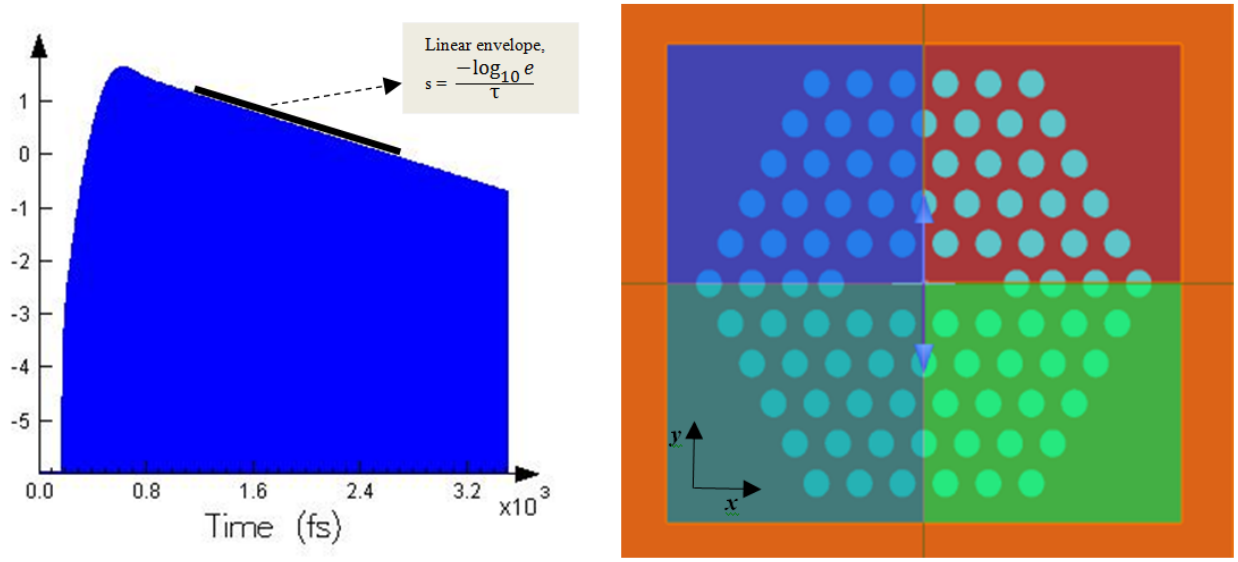

(a) *(b)*

Figure 3.5 *An example of a low Q factor cavity. (a) From the slope of the decay graph of the logarithm of electric field, one can calculate the Q of the cavity. (b) The layout of this simulation. There are only 6 periods of holes around the center of the cavity and therefore the Q factor is small and the slope of the graph in part (a) is steep enough to be measured exactly despite the short simulation time.*

For more information about this analysis group, refer to the the Lumerical User's manual. Using these analysis groups of monitors, it was found that after replacing air with a solvent as the background medium, the *Q* factor of the structure in Figure 3.4 (consisted of 10 rings of holes around the center of the cavity) dropped from 4570 to 770. This required redesigning the cavity to increase the *Q* in the presence of the solvent, as described below in section 3.4.3.

3.3.3. **The mode electric field intensity profile**

Figure 3.6 shows the results obtained using a frequency domain profile monitor (also known as a DFT monitor) and an index monitor. If we assume an electric field of the form:

$$\mathbf{E}(\mathbf{r},t) = \mathbf{E_0}(\mathbf{r},\omega)e^{i(\phi(\mathbf{r})-\omega t)} \qquad 3.1$$

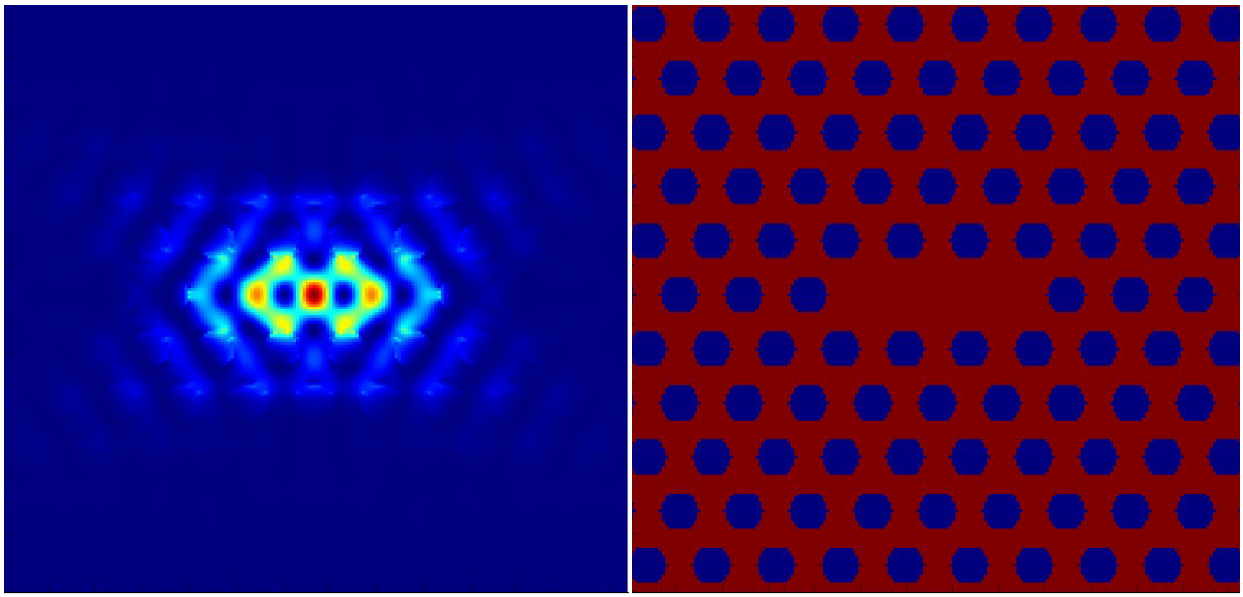

Figure 3.6 *The electric field intensity and refractive index profiles recorded by the DFT and index monitors of Figure 3.4. The images show a 2×2 (μm)^2 cross section of the structure (Figure 3.4) at the z=0 plane. The structure is in a solvent medium (n=1.445). The holes in right image are not perfectly circular because of the finite size of the mesh cells.*

the DFT monitor records the fast fourier transform (FFT) of the time domain electric field, which is $\boldsymbol{E}(\boldsymbol{r},t) = \boldsymbol{E_0}(\boldsymbol{r},\omega)e^{i\phi(r)}$.

The left image in Figure 3.6 is the intensity profile of the frequency domain field $|\boldsymbol{E_0}(\boldsymbol{r},\omega)|^2$.

One helpful feature of the DFT monitors (when set in the cwnorm state (see User Guide of Lumerical FDTD Solution)), is that there is no need to run the simulation with a long, quasi-cw source pulse for calculating fields at a specific frequency. Instead, a short pulse source can be utilized for excitation and the software calculates the time domain response of the system, and then calculates the Fourier transform of the fields and divides them by the Fourier transform of the source signal. This is more efficient because with a single simulation, one can get the response of the system at several frequencies and also there is no need for long simulations involving quasi-cw sources. The other benefit of the DFT monitors over time domain monitors is that it reduces the amount of memory required by the simulation by just recording the time domain data corresponding to some specific frequencies. Thus for the simulation corresponding

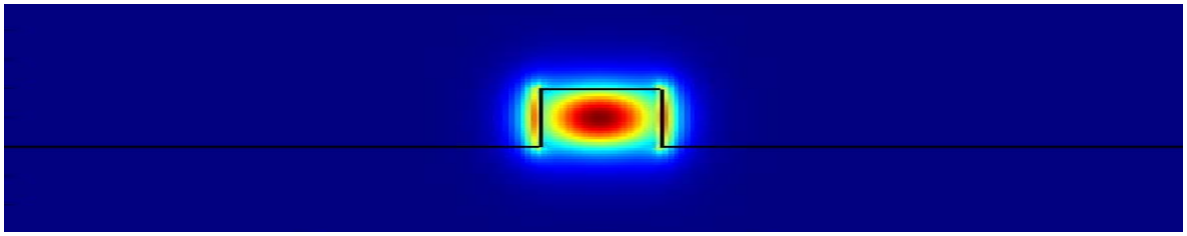

Figure 3.7 *The yz profile of the electric field intensity superimposed with the structure (the black line is the boundary between substrate plus ridge waveguide and the solvent environment.*

to Figure 3.6, we just set the frequency of the DFT monitor equal to the cavity resonance to get the profile of the cavity fundamental mode.

3.3.4. **The transmission efficiencies**

Figure 3.8a shows the structure used to estimate the transmission from the silicon ridge waveguide into and along the 1D PC waveguide of Banaee's design, in the absence of the PC cavity. The waveguides are assumed to rest on a SiO_2 slab, and are surrounded on top by a solvent with refractive index n=1.445. Since the refractive indices of the SiO_2 slab and the solvent were approximately the same (n=1.44427), it was decided not to undercut the PC cavity, **so all the following simulations correspond to non-undercut cavities**. It should be noted that although the refractive index of the solvent and SiO_2 slab were very close, the resonance of the cavity for the fundamental mode shifts from 1570nm to 1549nm, when we replaced the lower cladding of the cavity by the SiO_2 slab.

The source used for exciting the cavity through the ridge waveguide (which is lossless) was a "mode source". The Lumerical software is able to calculate the modes of a waveguide by knowing the cross sectional geometry of the waveguide. The ridge waveguide supports a single transverse electric (TE) mode with the profile illustrated in Figure 3.7. This waveguide structure makes it possible to employ a symmetric boundary condition along the x axis, to save computation time. Several 2D DFT monitors were placed at different locations along the waveguides to measure the intensity of the electric field and therefore the light power passing through them (Figure 3.8a).

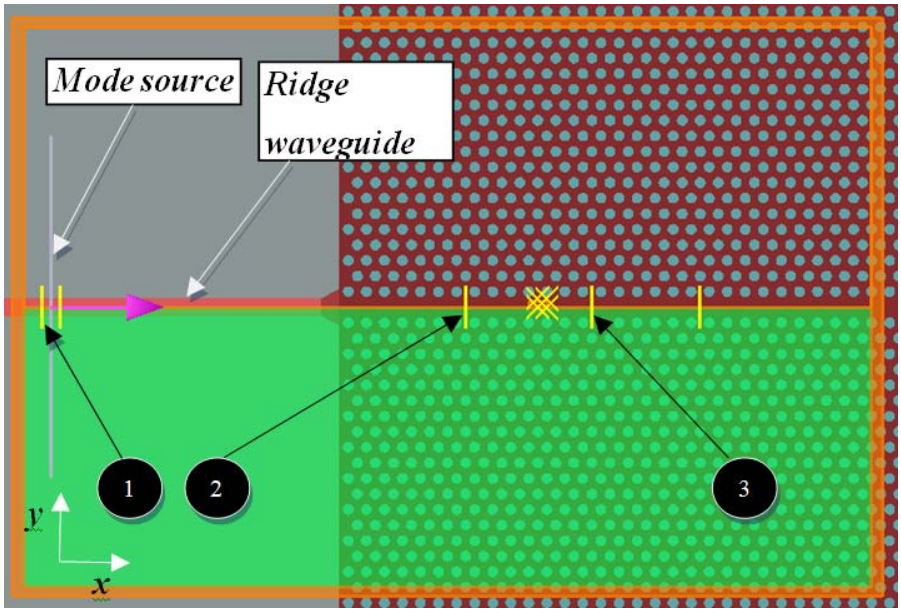

(a)

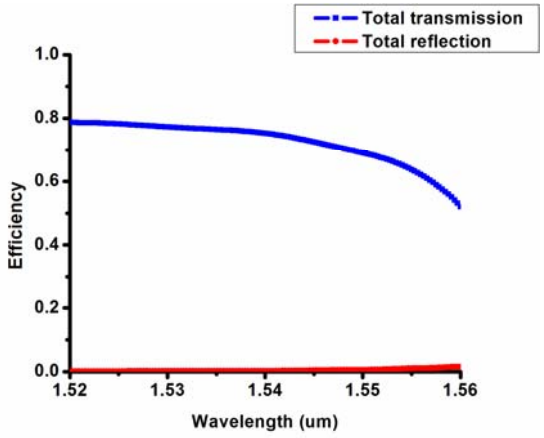

(b)

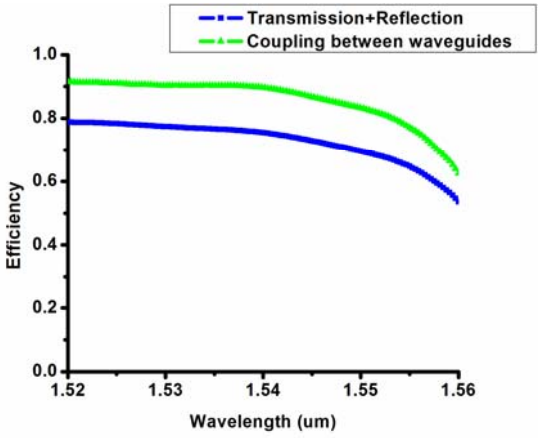

(c)

Figure 3.8 *(a) The simulation layout for measuring the transmission efficiency of the PC waveguide and the coupling efficiency between the ridge and PC waveguides. The injected mode source and the ridge waveguide are labeled. There are 5 DFT monitors at different locations, 3 of which are labeled 1 to 3. The monitors are 2D and their planes are perpendicular to the waveguides to measure the transmission efficiency in the x direction along the waveguides. The yellow cross marks are time monitors. (b) The transmission efficiency (blue curve) between the source and monitors #2, and the reflection efficiency (red curve) measured by monitor #1. (c) The sum of transmission through monitor #2 and reflection through monitor #1(blue curve). The green curve is the coupling efficiency between the ridge and PC waveguides calculated as explained in the text.*

Each of them was set to record data at 350 different frequencies to find the transmission spectrum at their locations. Monitor #2 was located 7 periods away from the interface of the two waveguides and monitor #3 was placed 7 periods away from monitor #2. The transmission efficiency from the source to the location of monitor #2 is illustrated in Figure 3.8b (blue curve). This curve told us that at a wavelength of 1549 (the resonance of the cavity when is not undercut) ~70% of the power that the source had injected into the ridge waveguide reached monitor #2, which is where the cavity is located in the final design. The red curve in Figure 3.8b shows the total reflection efficiency back from the interface of the two waveguides. Since the ratio between the transmission efficiencies of monitor #3 to #2 is equal to the transmission efficiency of 7 periods of PC waveguide, we could separately estimate how much of the total ~30% loss was due to scattering loss where the two waveguides meet, and how much was due to propagation along the PC waveguide. The distance between the green curve in Figure 3.8c and unity is the scattering loss at the junction of the two waveguides, which at 1549nm is ~ 16%.

In another simulation, the microcavity (case #2 in Table 3.1 but without undercutting) was added to the system as shown in Figure 3.9a. The transmission efficiency measured by monitor #2 and the total reflection back to the ridge waveguide, measured by monitor #1, are illustrated in Figure 3.9b and 3.9c. From the transmission curve (blue), it was found that the transmission efficiency from the source to monitor #2 was zero except near to the resonance of the cavity (1549nm) where it reached a maximum of ~1.8%. The reflection curve (red) shows that ~41% of the total injected power, on resonance, was reflected back to the ridge waveguide. Therefore ~57% (=100-41-1.8) of the total injected power was dissipated on resonance. Since the reflection before adding the microcavity was almost zero over the whole range of wavelengths (Figure 3.8b red), the reflection in Figure 3.9c is entirely due to the coupling of the PC waveguide and the microcavity.

To find the coupling efficiency between the input PC waveguide and the microcavity, we used the data of both simulations (Figure 3.8 and 3.9).

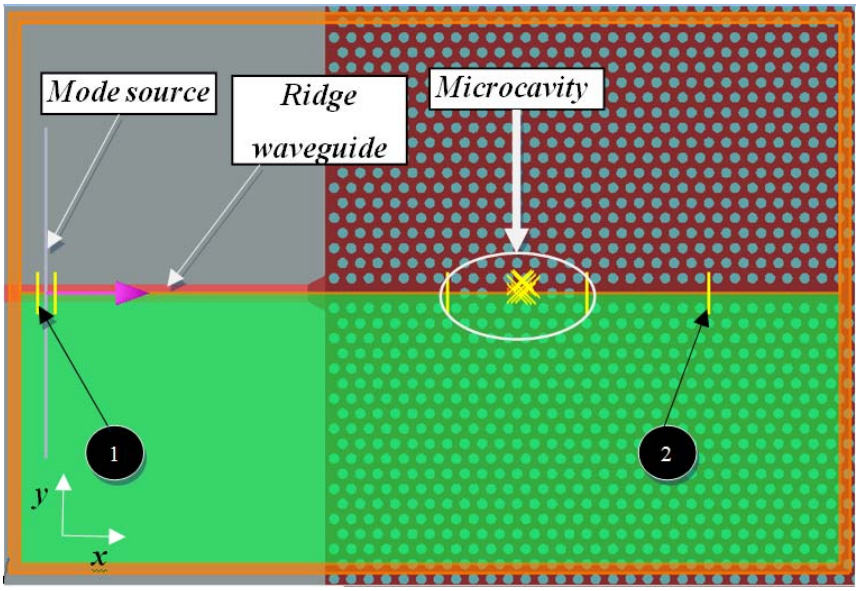

(a)

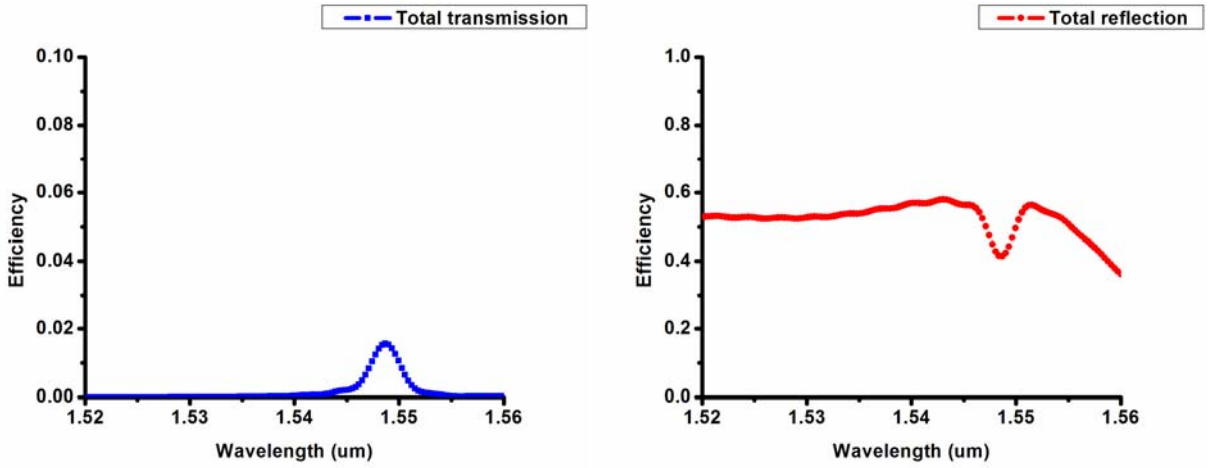

(b) *(c)*

Figure 3.9 *(a) The simulation layout for measuring the transmission efficiency through the microcavity. The injected mode source and the ridge waveguide are labeled. There are 5 DFT monitors at different locations, 2 of which are labeled 1 to 2. The monitors are 2D and their planes are perpendicular to the waveguides to measure the transmission efficiency in x direction along the waveguides. The yellow cross marks are time monitors. (b) The total transmission efficiencies between the source and monitors #2. (c) The total reflection efficiency measured by monitor #1.*

From Figure 3.8b, we found that ~70% of the total power reached to monitor #2. The position of monitor #2 is right before the place that the microcavity is located in Figure 3.9, so ~70% of the total power reaches the microcavity. On the other hand, from Figure 3.9c we found that ~41% of the total power was reflected back to the ridge waveguide. Thus, ~84% ($= \frac{0.41}{(0.70)^2}$) of the power that reached to the microcavity was reflected back and therefore the coupling efficiency between the PC waveguide and the cavity was found to be ~16% (=100-84).

A third simulation was run to confirm the total transmission from the input ridge waveguide to the output ridge waveguide. The simulation structure is illustrated in Figure 3.10a. It contained the input and output ridge and PC waveguides as well as the PC microcavity. The cavity is the same as in the previous simulation (case #1 in Table 3.1 without undercutting). The medium is also the same (n=1.445). The transmission measured by monitor #2 in Figure 3.10a is shown in part b of this graph.

In Figure 3.10b, the blue curve is the total transmission efficiency spectrum recorded at the location of monitor #2. The spectrum has higher resolution than the graphs in Figure 3.8 and 3.9 to find the exact value of the total transmission. The transmission on resonance was ~ 1.6%. By dividing this value (i.e. 1.6) by the transmission efficiency from the source up to the cavity (that was measured in Figure 3.8b to be ~70%), we estimate the power that was out-coupled from the cavity to the output PC waveguide to be ~ 2.3% of the total injected power. Thus we conclude that ~3.3% ($= \frac{2.3}{70}$) of the power delivered to the cavity by the input PC waveguide was transmitted to the output PC waveguide. This value should be equal to the theoretical value of $\frac{Q^2}{{Q_w}^2}$ (for definition of Q and Q_w see section 1.4.2). The Q factor of the cavity (case #2 in Table 3.1 without undercutting) before adding the PC waveguide was about 700 (this is equivalent to Q_v due to the large number of the rings around the cavity) and after adding the waveguides to the cavity (Figure 3.10a) the Q dropped to about 580 (this is equivalent to total Q). Therefore the Q_w was found to be ~3380. These values of the total Q and Q_w give a theoretical transmission efficiency of ~3% for the microcavity, which was in good agreement to the value found above from DFT monitors (i.e. ~3.3%). Note that this transmission efficiency is far off from the optimum value, which is 25%.

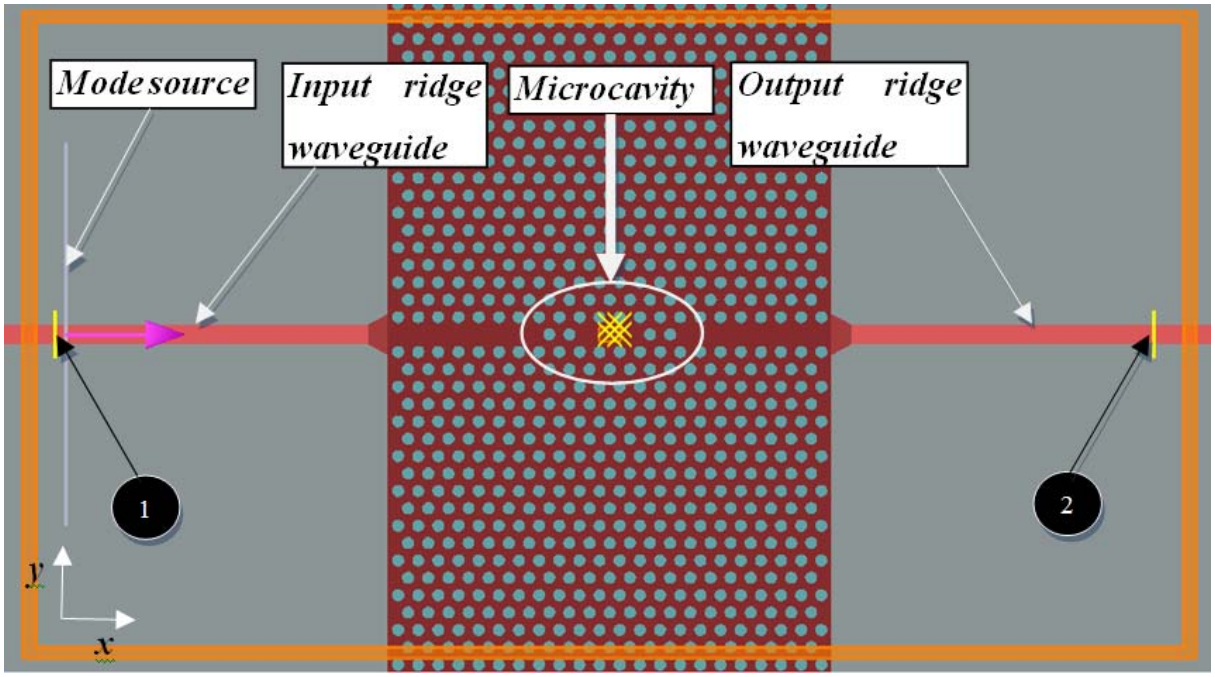

(a)

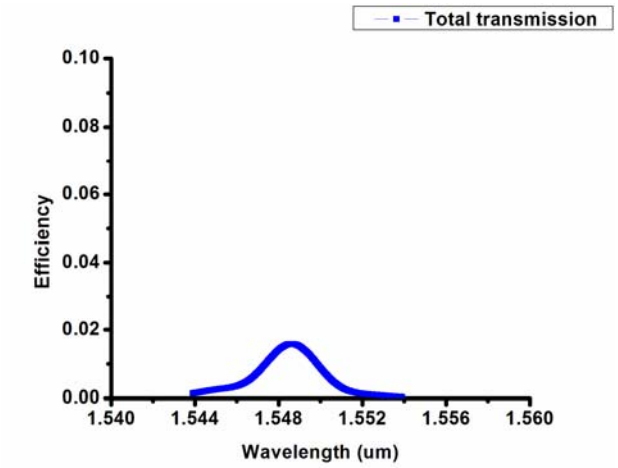

(b)

Figure 3.10 *(a) The simulation layout for measuring the transmission efficiency through the entire structure including input and output ridge and PC waveguides as well as the microcavity. The mode source and the ridge waveguides and the cavity are labeled. The two DFT monitors are labeled 1and 2. The yellow cross marks are some time monitors for measuring Q factor. (b) The transmission efficiency from the source to monitor #2. It has higher spectral resolution than the graphs of Figures 3.8 and 3.9. This spectrum is fully resolved, as its Q value agrees with that found from measuring the Q using the time domain approach explained above.*

Table 3.2 *Summary of scattering properties of the existing "for-vacuum" design (Figure 3.10a) immersed in a solvent environment.*

Input power (%)	***Total reflected power (%)***	***Power reaching the cavity (%)***	***Power transmitted through cavity (%)***	***Power reaching the output ridge waveguide (%)***
100	*41*	*70*	*2.3*	*1.6*

3.4 Design Optimization

As previously mentioned, the objective of maximizing the optical trapping force at the antinode of the cavity requires having the highest possible coupling efficiency from the light source to the cavity. In chapter 1 (section 1.4.2) we found that the energy stored inside the cavity is dependent on both in-plane and out-of-plane Q factors and also we found that to enhance the energy stored in the cavity, we should enhance the Q_v as much as possible and then try to set Q_w equal to Q_v. But as we investigated in the previous section, the Q_v factor of Banaee's cavity dropped from > 4000 to <800, after adding the solvent. In addition, the PC waveguide transmission loss (14% for 7 periods) and the coupling loss between the ridge and PC waveguide (~ 16%) are high when Banaee's structure is in a solvent environment. The following describes design changes made to improve the performance of this structure in a solvent environment.

3.4.1. **Modification of the PC waveguide**

To understand the relatively high loss of Banaee's 1D waveguide when in a solvent environment, the band structure of the 1D PC waveguide was investigated. The relevant branch of the band structure for the PC waveguide mode near to the BZ boundary is plotted in Figure 3.12c. The curves shown in this figure are for two different cases.

1. PC waveguide made from a row of missing holes in the PC lattice (Banaee's structure) but with background refractive index of 1.445.

2. The same as case 1 but with one change: The radius of the nearest neighbour holes to the PC waveguide were reduced from r_1=0.30a to r_1=0.22a (a is the pitch of the lattice). These structures are described fully in Table 3.3 and their simulation layouts are shown in Figure 3.12.

As shown in Figure 3.12, for the first case of Table 3.3 the cavity resonance was very close to the Brillouin zone boundary, where the group velocity of propagating modes is very small, which result in higher loss (see section 1.4.1). Also operating close to the band edge limits flexibility in adjusting the cavity resonance frequency.

Table 3.3 *The characteristics of the structures used for finding the band structure of the PC waveguide mode in Figure 3.12.*

Case #	***Pitch of the lattice(nm)***	***Lattice regular holes' radius***	***Nearest neighbor holes' radius***	***PC waveguide cladding refractive index***
1	*a=420*	*r=0.3a*	*r1=0.3a*	*n=1.445*
2	*a=420*	*r=0.3a*	*r1=0.22a*	*n=1.445*

The radius of the nearest neighbor holes to the PC waveguide were reduced to shift down the band structure [**Yamada2001**, **Kim2004**] (Figure 3.12c). Other, more complicated modifications to the design that could reduce the loss in the PC waveguides [**Grillet2003**, **Yamada2001**] were considered, but they were either hard to fabricate, or they were difficult to couple to from the ridge waveguides (i.e. the reflection at the interface of the ridge and PC waveguides was large). By shifting down the band structure of the waveguide we expected to have higher group velocity and therefore smaller loss. It is crucial to note from Figure 3.12 c) that the cavity mode intersects the waveguide dispersion curves above the solvent light line. This means that, unfortunately, the PC waveguide modes are intrinsically lossy. As shown below, the losses are not large enough over the short propagation length, to be a serious concern. However, future design iteration would attempt to shift this intersection below the light line.

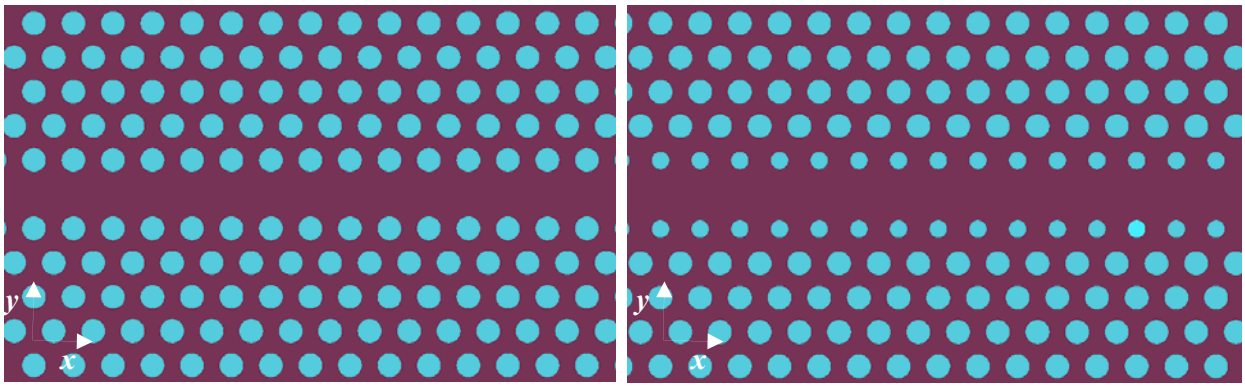

(a) *(b)*

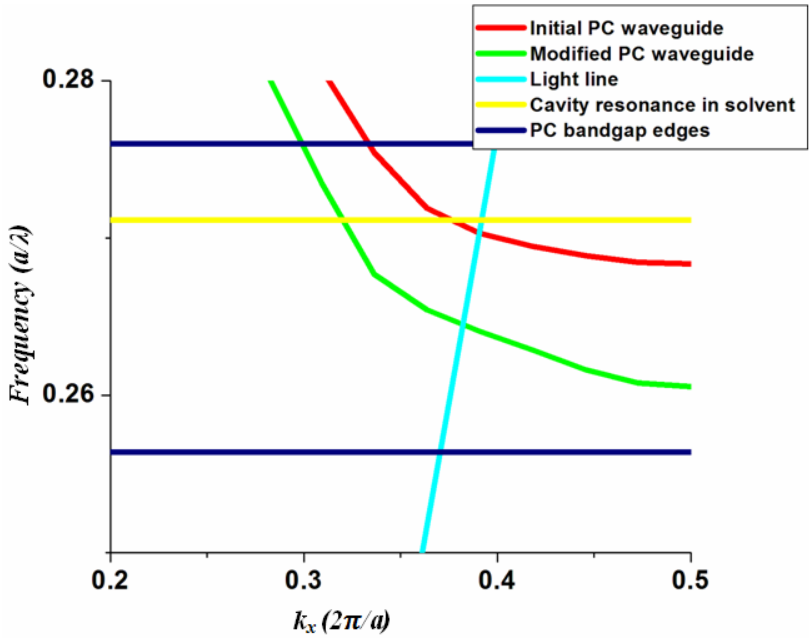

(c)

Figure 3.11 *(a) The structure layout for the first case of Table 3.3, where all holes have the same radius.(b) The structure layout for the second case of Table 3.3, in this case the nearest holes to the waveguide have smaller radius. (c) A portion of the waveguide mode dispersion (near to the first Brillion zone edge) of the PC waveguides. Each curve corresponds to one of the cases mentioned in Table3.3. The yellow line is the cavity resonance in solvent (i.e.1549nm). The lightline in the solvent as well as the bandgap of PC lattice are also indicated.*

3.4.2. **Characterization of the new PC waveguide**

A separate simulation (Figure 3.12a) was run to measure the transmission efficiency of the modified PC waveguide and also to find the coupling efficiency between the waveguides. This simulation is exactly equivalent to the simulation of Figure 3.8a, which we had run for the original waveguide except that we replaced the original PC waveguide (with r_1=0.3a) with the modified one (with r_1=0.22a). The results of the simulation are shown in Figures 3.12b and 3.12c. After doing the same procedure, we measured the same quantities as we had measured for the original PC waveguide; we found that the transmission efficiency from the source to monitor #2 was ~ 87% and the reflection back to the ridge waveguide was ~0% of the total source power.

By using the ratio between the transmission efficiencies measured by monitors #2 and #3, which is equal to the transmission efficiency of 7 periods of PC waveguide, we found that the coupling efficiency between the ridge waveguide and the PC waveguide was ~ 92% and therefore the loss in the interface was ~ 8% of the total injected power of the source, and the loss in 7 periods of PC waveguide was ~5% (=13-8) of the total power.

Thus the coupling efficiency between the ridge and PC waveguide is enhanced from ~84% to ~92% and the loss in 7 periods of PC waveguide was reduced from ~14% to ~5%. Note that all of these reported values are at the wavelength of 1549nm (Banaee's PC microcavity resonance in solvent). The other potential benefit of this PC waveguide design is the larger bandwidth that lies within the PC bandgap, and also below the solvent light line.

The next step in modification of the design was to maximize the amount of energy that gets into the cavity from the PC waveguide, for a given cw laser excitation power.

The following section explains the two steps followed to increase the optical energy stored in the cavity: first the cavity was modified to increase Q_v in the solvent environment, and then the coupling between the cavity and PC waveguide was modified to set Q_w equal to Q_v.

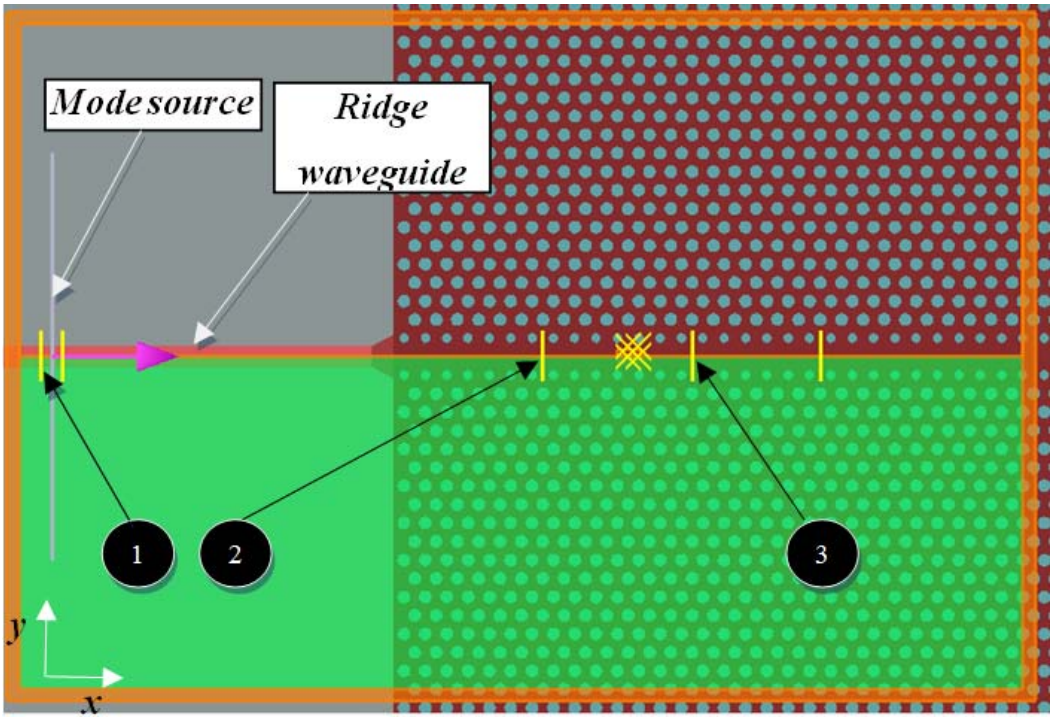

(a)

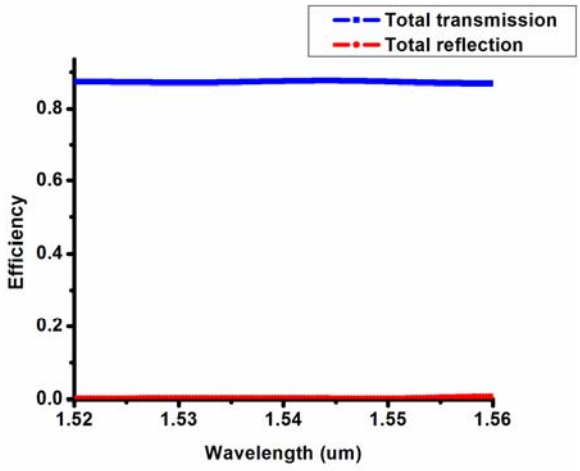

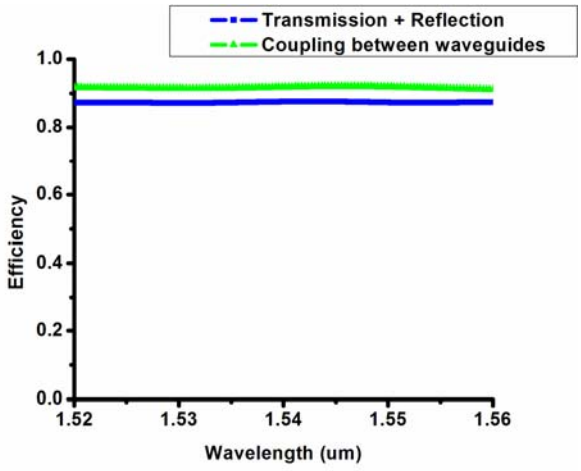

(b) *(c)*

Figure 3.12 *(a) The simulation layout for investigating the transmission efficiency of the modified PC waveguide. This simulation is equivalent to the one in Figure 3.8 except that the nearest holes to the PC waveguide are shrunk. (b) The transmission efficiency from the source up to monitor #2 (blue curve) and the reflection back to the ridge waveguide (red curve) recorded by monitor #1. (c) The sum of the reflection and transmission curves of part b (blue curve) and the coupling efficiency between the ridge and PC waveguides (green curve).*

3.4.3. **Maximizing Q_v as limited by coupling to radiation modes**

Shrinking the side-holes or shifting them outward, in the L3 cavity, leads to the so called "gentle confinement" regime which enhances the Q factor [**Akahane2003**, **Akahane2005, Andreani2004, Srinivasan2002**]. By making these changes, one can tailor the defect geometry in Fourier space, which decreases the coupling between the momentum components of the cavity mode and those momentum components that are either guided in the PC slab or located above the light line of the cladding. The Q factor of Banaee's cavity in solvent was therefore calculated for different side-hole shifts (Figure 3.13). The PC lattices in these simulations consisted of ten rings of holes. The upper cladding was solvent (n =1.445) and the structure was on top of a SiO_2 substrate (n=1.44). The symmetry boundary condition along x axis was anti-symmetric and along the y axis was symmetric. The side shifts of the holes s were varied from 0.1a to 0.2a.

The results of the simulations are shown in Figure 3.13. Since there are the several rings of holes around the cavity, the in-plane Q is not affected significantly by the side-holes shift and therefore the Q calculated in Figure 3.14b is a representative of Q_v. From Figure 3.13, the shift of 0.2a gives a higher Q. Higher shifts were disregarded, because of fabrication issues (when the two neighboring holes get too close to each other, chances were high to overexpose that area, during lithography).

To increase the Q_v factor further, we investigated shrinking the side holes [**Andreani2004**]. The side-holes radius was changed from r'=0.22a to r'=r=0.3a, for a shift of s=0.2. It was found that for r'=0.22a, Q_v had its maximum value (~ 3100). Smaller radii were not tested because the fabrication would be more challenging for them, reducing the already low yield.

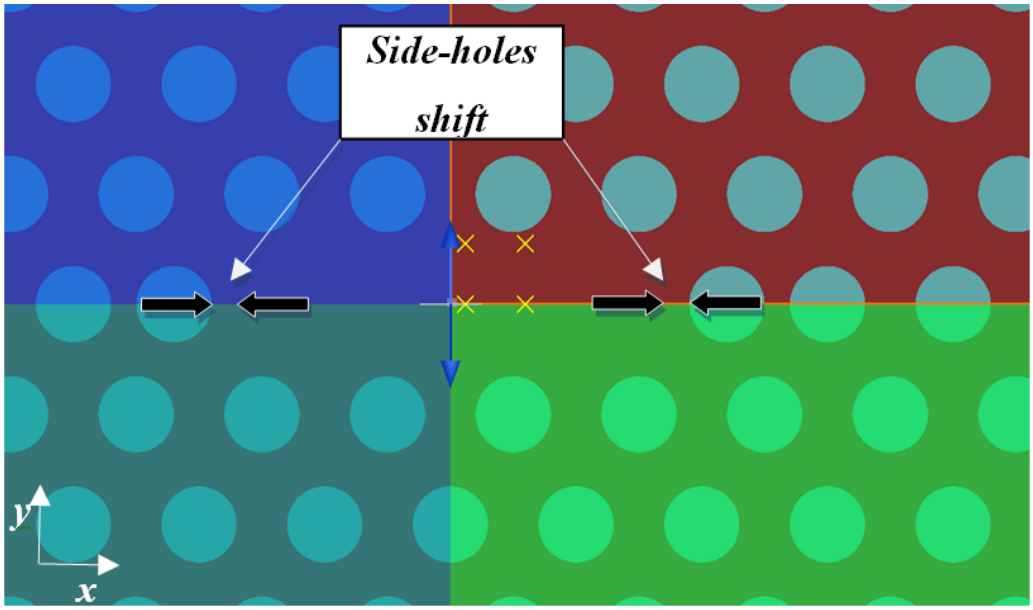

(a)

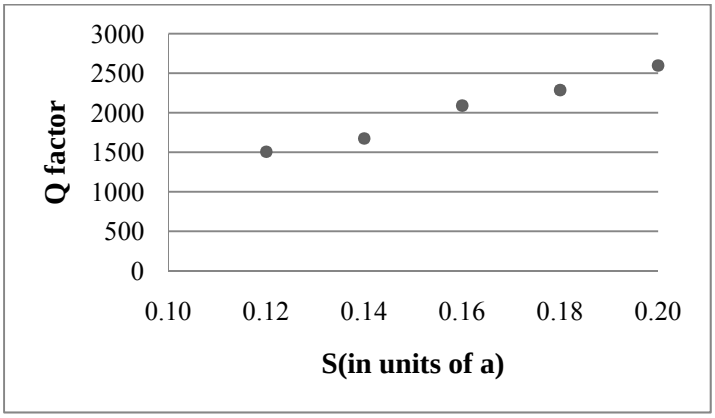

(b)

Figure 3.13 *(a) This image shows the layout of the structure of an L3 cavity. The black arrows show the side-hole shifts. The blue arrow shows the polarization of the electric dipole source, placed at the center of the cavity. The four yellow crosses are the analysis group of time point monitors for measuring the Q factors. (b) The simulation results showing the effect of side-holes shifts on the Q factor.*

After optimizing the Q_v factor of the cavity, we had to optimize the coupling between the modified cavity and the modified 1D PC waveguides mode to get more energy from the PC

waveguide into the cavity (setting Q_w equal to Q_v). The coupling properties depend on spatial overlap between the waveguide mode and the cavity mode [**Kim2004**].

Knowing Q_v from simulations of the isolated cavity, Q_w could be easily calculated by using $\frac{1}{Q} = \frac{1}{Q_w} + \frac{1}{Q_v}$, where Q is the total Q found by simulating the full structure, including both cavity and the PC waveguides.

To modify the coupling between PC waveguides and the cavity, the radius and position of the holes (indicated ed with yellow arrows in Figure 3.14) were changed systematically to satisfy the required condition (i.e. setting Q_w equal to Q_v).

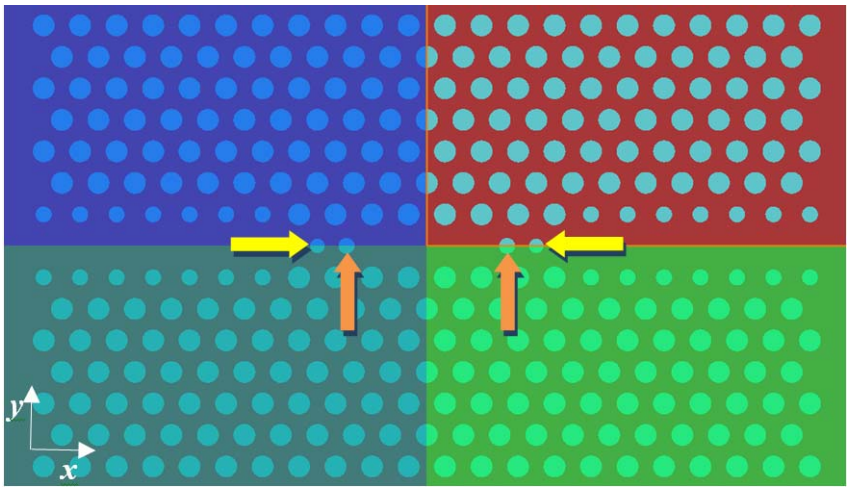

Figure 3.14 *The final optimized design for the optical trapping experiment. This is the layout of the FDTD simulation. The yellow arrows show the two holes with radius r" and side shift of s' and the orange arrows are pointing to holes of radius r' and side shift of s. All parameters of the structure are mentioned in Table3.4. The background medium had n=1.445 and the substrate was SiO_2 (n=1.444)*

Table 3.4 *The cavity parameters used for enhancing the coupling efficiency between the PC waveguide and cavity.*

Pitch (nm)	***Lattice holes radius***	***Side-holes shifts***	***Cladding refractive index***	***Side-holes radius***	***Mesh cell dimensions***
a=420	*r=0.3a*	*s= 0.20a*	*n=1.445*	*r'=0.22a*	*(0.025a, 0.025a$\frac{\sqrt{3}}{2}$,0.05d)*
		s'=0.04a		*r"=0.22a*	

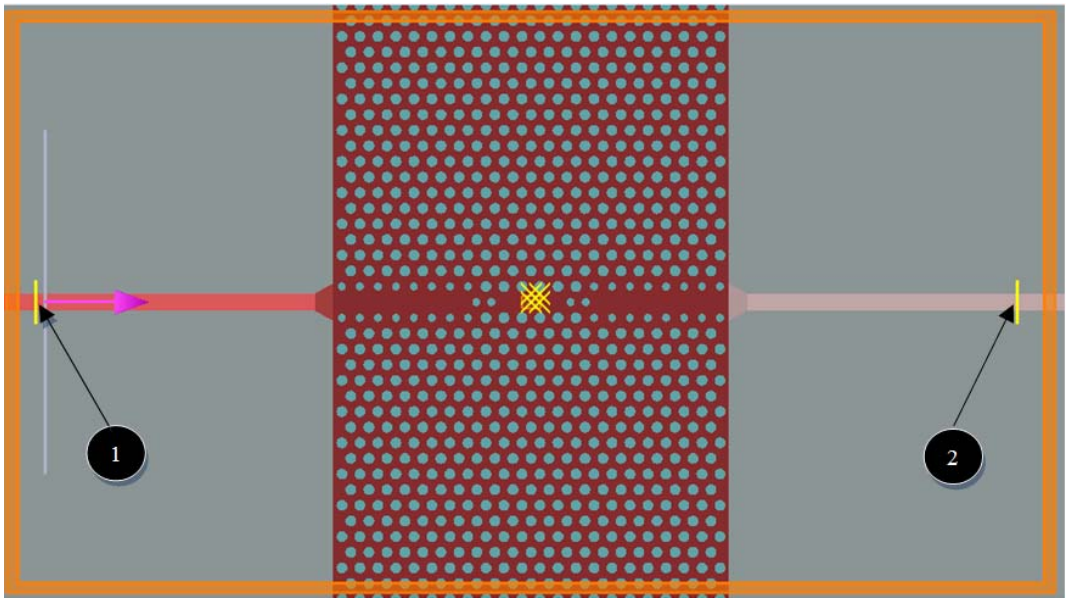

(a)

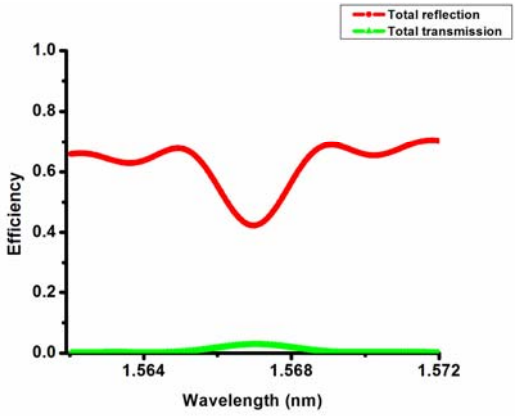

(b)

Figure 3.15 *(a) The simulation layout used for measuring the total transmission and reflection efficiencies from the input ridge waveguide to the output for the modified structure. (b) The total transmission efficiencies (green curve) and the total reflection efficiency (red curve) for the structure of part (a). The reflection was measured by monitor #1 and the transmission was measured by monitor #2. Because of the higher Q factor, the spectrum is* ***not*** *resolved, so the peak transmission values are inaccurate.*

It was found that for a design with the parameters shown in Table 3.4, the condition would be satisfied and the total Q would be very close to $0.5Q_v$, while maintaining a relatively high Q_v of 3800. In particular, Q was found to be ~1900. Thus we expect the microcavity to pass ~ 25%$\left(= \left(\frac{1900}{3800}\right)^2\right)$ of the power incident on it through the input PC waveguide. This value should be compared with ~3% of the Banaee design immersed in solvent.

It should also be mentioned that the resonance of the cavity after the modifications was shifted from 1549nm to 1567nm.

Finally we simulated the transmission efficiency through the entire structure for the modified design (PC waveguide and cavity). The simulation structure is illustrated on Figure 3.15. At the new cavity resonance (1567nm) the transmission efficiency form the ridge waveguide to the location of monitor 2 in Figure 3.12a is ~86%. Based on the simulated Qv and Qw values discussed above the coupling through the cavity was found to be very close to the optimum value of ~25%,so if the simulation were fully resolved (a simulation that would last several days!) the transmission efficiency form the input ridge waveguide to the output ridge waveguide should be ~18%. Overall, a considerable improvement has been achieved over Banaee's design immersed in solvent.

3.5 Force Calculation

3.5.1. **Maxwell Stress Tensor (MST) method**

Once the structure was optimized, we calculated the radiation force exerted on a particle near the antinode of the cavity mode, as projected onto the top silicon surface.

As explained in the previous chapter (section 2.1.2), the non-resonant radiation force on a nanoparticle calculated using the self-consistent MST is:

$$\langle \mathbf{F} \rangle = \oiint \langle \overleftrightarrow{\mathbf{T}} \rangle \cdot \mathbf{nda} \qquad 3.2$$

To find the force we have to calculate the average MST over a closed surface, which surrounds the nanoparticle. The nanoparticle in our calculation was a sphere of radius 50nm with refractive index of 1.49. This is meant to represent a 5 nm diameter PbSe nanocrystal embedded in a much larger diameter polymer sphere. It was placed at different heights with respect to the center of the cavity and the corresponding radiation forces on the particle were calculated.

To calculate the integral of eq. 3.2, six 2D frequency domain power monitors were used. Each of these monitors can record the electric and magnetic fields at its position. So all together, these monitors can make a closed 3D box around the nanoparticle and give the fields' spatial distribution on the surface of the box (Figure 3.16d). The monitors were set to find the field profiles exactly at the resonance frequency of the cavity. Once the spatial profiles of the fields are known, we were able to calculate the surface integral in eq. 3.2.

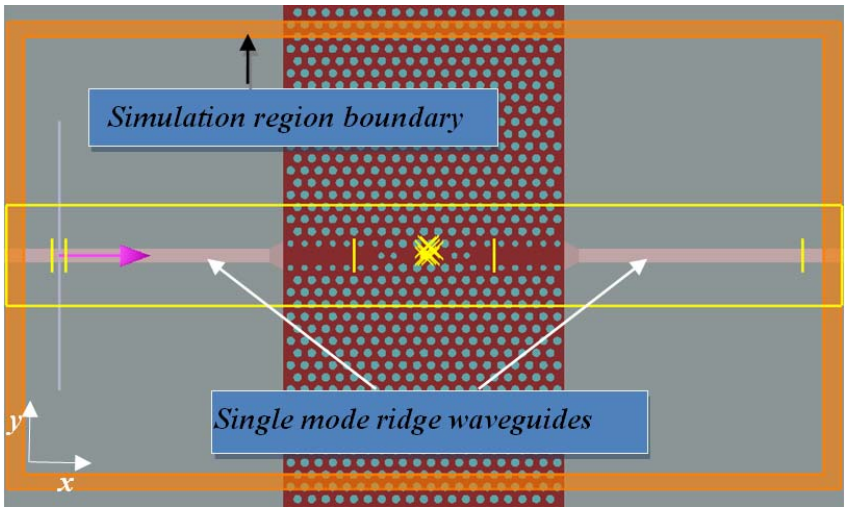

(a)

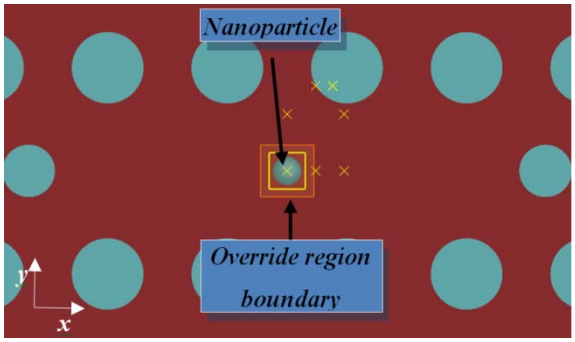

(b)

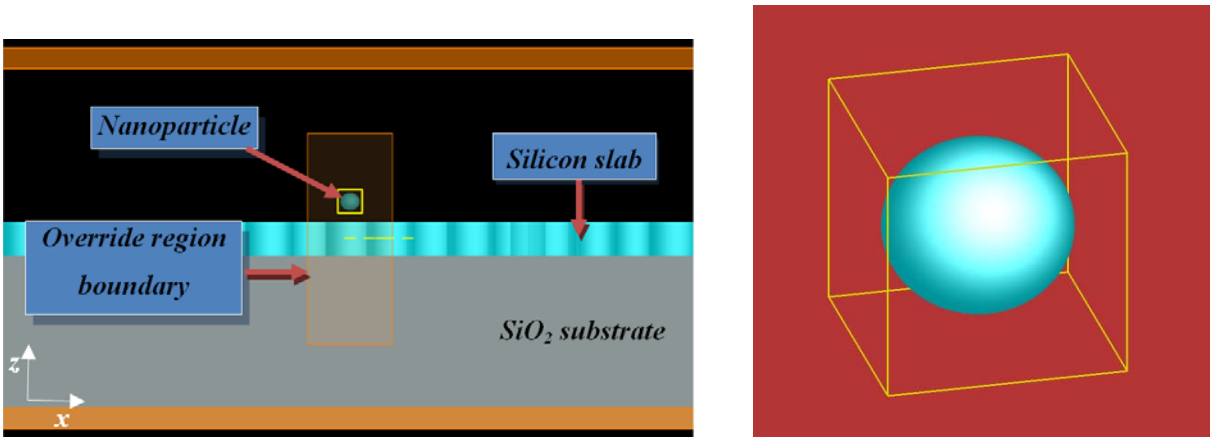

(c) *(d)*

Figure 3.16 *(a) The simulation layout for the optical force calculation. The yellow lines and boxes are frequency domain monitors and yellow crosses are point time monitors. Simulation region boundary and the override region are shown on the pictures. (a) The top view (xy plane) of the design. (b) A larger view of the cavity and the nanoparticle. (c) The side view (xz plane) of the structure. (d) Nanoparticle and six 2D monitors surrounding it.*

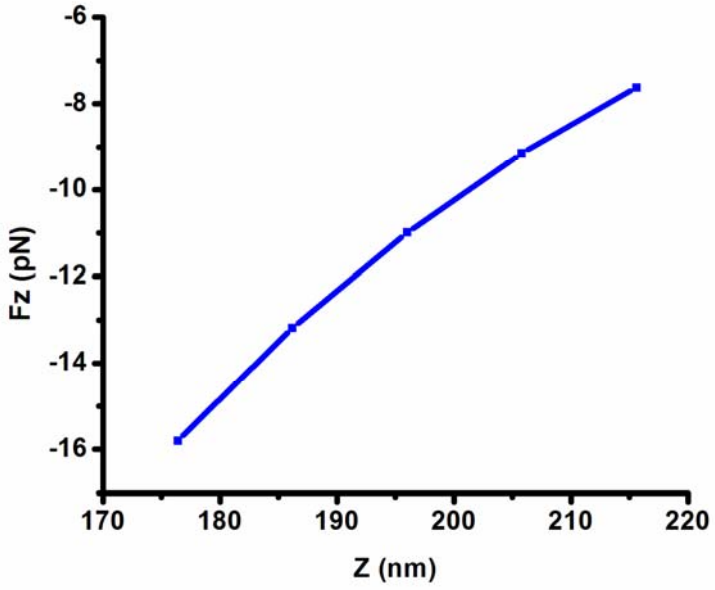

Figure 3.17 *Plot of F_z versus the displacement of the NP along z axis, calculated using the MST method. The NP is located above the center of the cavity and z is the distance between the NP and the center of the cavity. The force is normalized to a light power inside the input ridge waveguide of 1 W.*

The results are shown on Figure 3.17. The forces are normalized to the power injected by the source into the input ridge waveguide of 1 W. It should be mentioned that even when there was no particle in the 2D DFT monitors box, the calculated force was not exactly zero, which was because of numerical errors in the data collected by the DFT monitors. Thus, to find the real radiation force due to the presence of the nanoparticle, we subtracted the force in the absence of the particle from the force calculated with it in the simulation.

3.5.2. **Radiation force in dipole approximation**

In this section we compare the MST integration method with the much faster, but approximate dipole gradient force calculation. From previous chapter (section 2.1.1) it was found that for Rayleigh particles, we can estimate the radiation force from knowledge of the field profile in the absence of the particle, using the dipole approximation (all symbols were defined in section 2.1.1):

$$\langle \mathbf{F}(\mathbf{r},\omega)\rangle = \frac{\alpha'(\omega)}{4}\nabla \mathrm{E_0}^{\mathbf{2}}(\mathbf{r},\omega) + \frac{\alpha''(\omega)}{2}\mathrm{E_0}^{2}\nabla\phi(\mathbf{r}) \qquad 3.3$$

For the cavity mode, which is effectively a standing wave, the second term is zero. To find $\nabla {E_0}^2(r,\omega)$, we only need to find the 3D distribution of the electric field (no surface integrals are required, and the simulation does not have to be run separately for different particle positions). We found $E_0(\mathrm{r},\omega)$ in the cavity with a 3D DFT monitor. Exactly the same simulation as in Figure 3.16 was run to find the 3D distribution of the electric field but with two changes: the particle was removed and a 3D DFT monitor was placed above the cavity (Figure 3.18).

The polarizability of a bulk dielectric sphere of radius a and refractive index of n_1 in a medium of refractive index of n_2 is defined as [**Harada1996**]:

$$\alpha = 4\pi\epsilon_0 \mathrm{n_2^2 a^3}\,\frac{\mathrm{m^2-1}}{\mathrm{m^2+2}}, \qquad 3.4$$

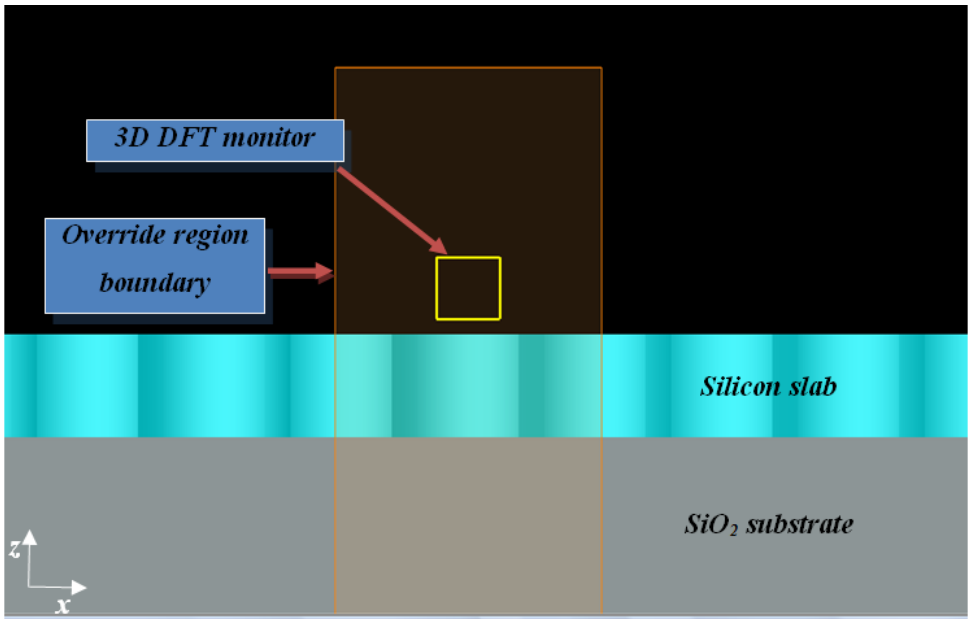

Figure 3.18 *The simulation layout for recording the 3D distribution of the electric field on top of the silicon slab. The 3D DFT monitor was used for this purpose. The structure and all other simulation parameters including the mesh cell dimensions were the same as Figure 3.16 except that the nanoparticle was removed and a 3D DFT monitor was used instead the 2D monitors.*

where $m = \frac{n_1}{n_2}$ is the relative refractive index of the particle with respect to the medium. Thus the polarizability for the particle in our simulations was found to be 5.99×10^{-34} C m^2 V^{-1}. The force calculated by this method is plotted in Figure 3.19. The comparison between MST and dipole approximation is illustrated in Figure 3.20. The two methods agree very well, showing that the nanoparticle acts to a good approximation as a point dipole and doesn't perturb the mode fields significantly. This is reasonable because the particle was much smaller than the wavelength of the light and also its relative refractive index to the surrounding medium *m* was very close to 1. The significance of these results is discussed in Chapter 6.

See appendix B for some technical notes about the FDTD Simulations ran for the results of this chapter.

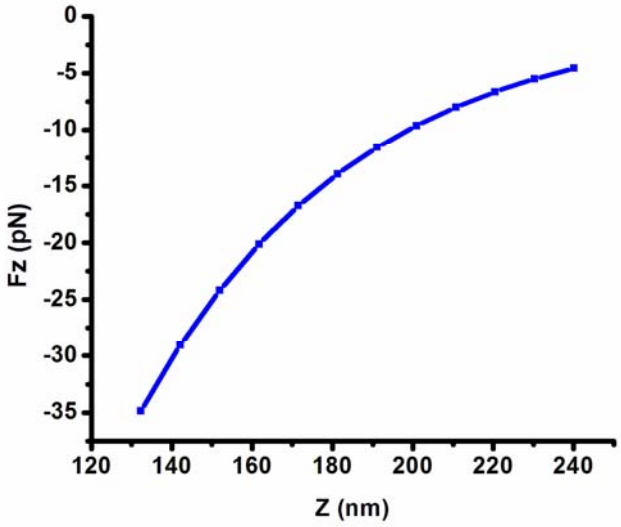

Figure 3.19 *Plot of F_z versus the displacement of the NP along z axis, using the dipole approximation. z is the distance between the NP and the center of the cavity. The force is normalized to a light power inside the input ridge waveguide of 1 W.*

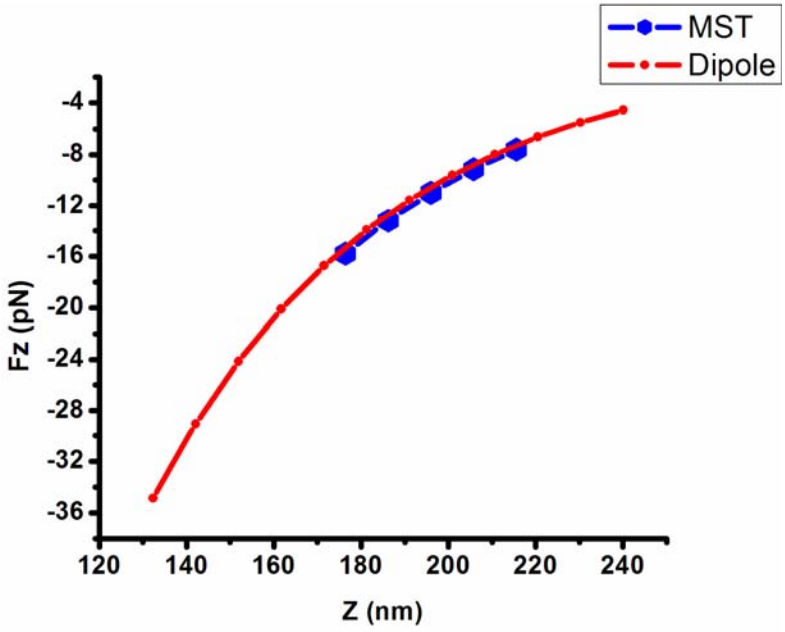

Figure 3.20 *The comparison between the two methods (i.e. MST and dipole approximation) for calculation of the radiation force on a50 nm diameter nanoparticle.*

CHAPTER 4 FABRICATION

4.1 Introduction

In this chapter, we describe our fabrication goals and accomplishments. The initial goal was fabricating samples with the structure of Figure 4.1. Since the size of the entire structure was larger than the writing field of the SEM machine that was available (90×90 μm^2), we decided to use some samples (Figure 4.2) which already had some grating couplers and multimode waveguides on them. So our actual goal was to add other parts (i.e. tapered, ridge and PC waveguides as well as the PC cavity) of the main structure to the structure of Figure 4.2 (see Figure 4.3 for clarification)

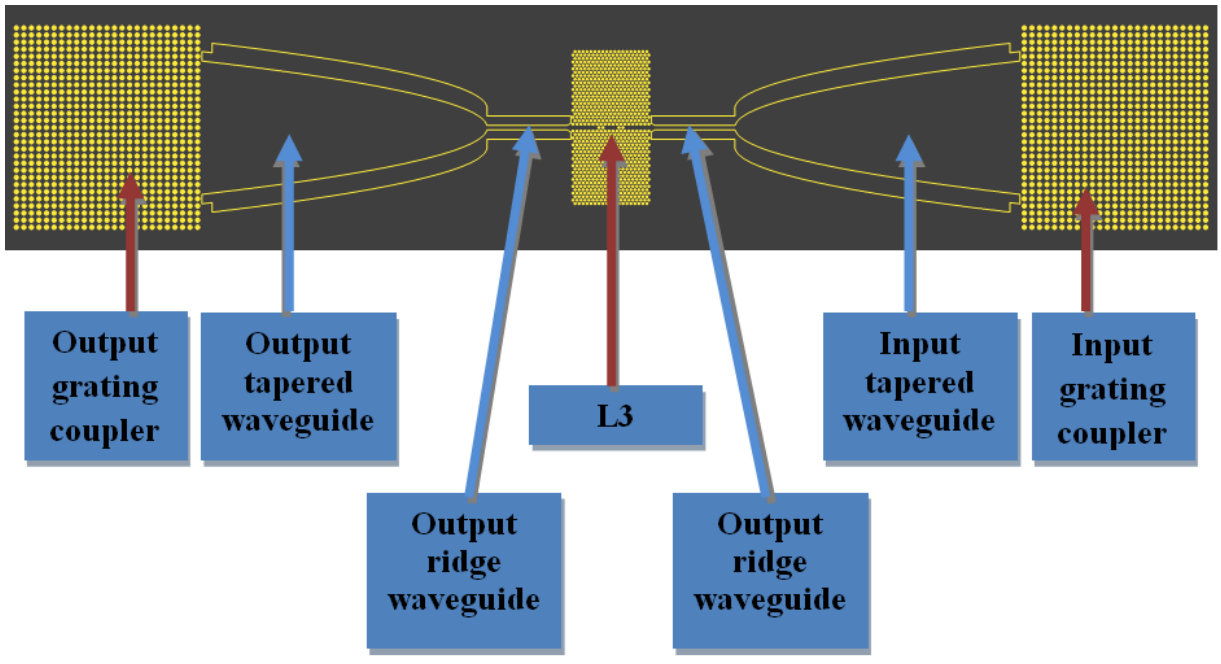

Figure 4.1 *The design of the structure that we aimed to fabricate. It should be mentioned that the PC cavity and waveguides of this structure are the same as Figure 3.16a.*

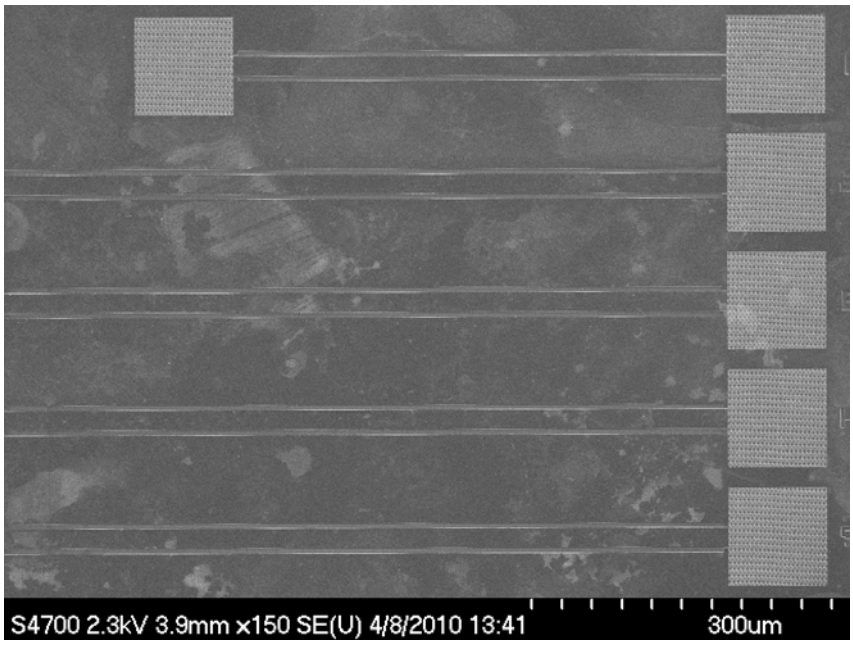

(a)

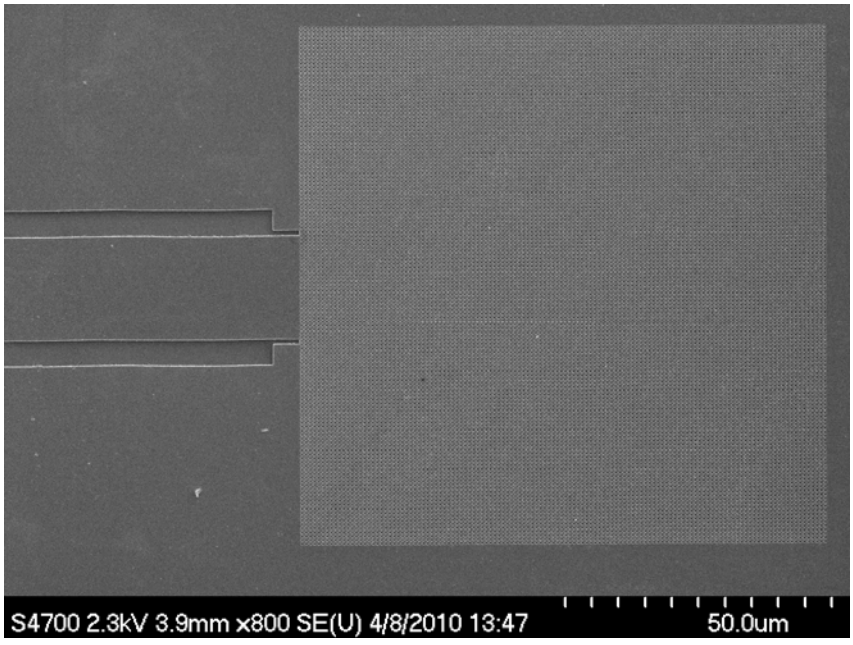

(b)

Figure 4.2 *The SEM images from the samples that already had grating couplers and multimode waveguides on them. The grating couplers (squares) were 100×100μm^2. The width of the waveguides is*

20 μm. (a) This image shows a group of 5 waveguides with different lengths. The boundaries of the waveguide are the parallel lines. (b) The magnified image of one grating coupler and its waveguide.

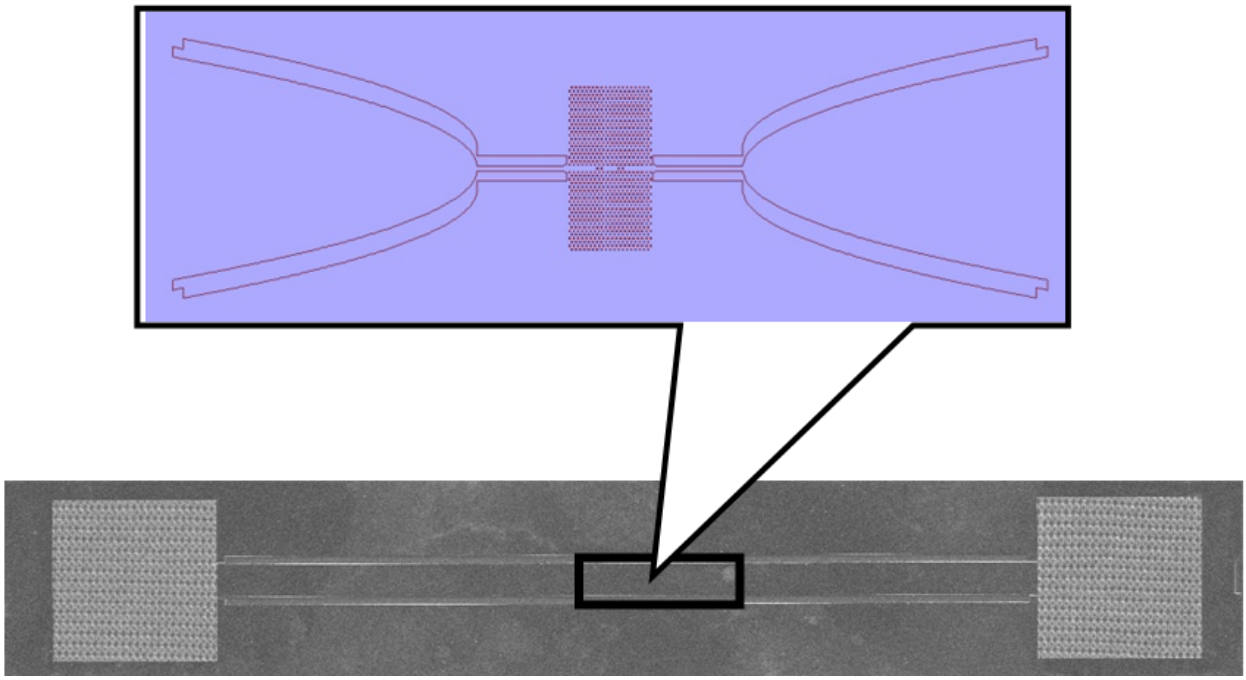

Figure 4.3 *The position that the rest of the structure will be fabricated is shown by the black box which is at the middle of the multimode waveguide.*

The following summarizes the fabrication process of PC cavities on SOI that was developed by Dr. Andras Pattantyus-Abraham and Dr. Murray McCutcheon and in Young's group.Fabricating PC cavities generally involves 5 main steps:

1. Silicon wafer cleaning and coating
2. Electron beam lithography (EBL)
3. Developing
4. Plasma etching
5. Undercutting

For the current structures the final step is not necessary because the cavities are designed to work in solvents with similar refractive indices as the SiO2 layer in the SOI structure. Undercutting is therefore not effective for increasing the optical confinement.

4.2 Wafer Cleaning And Coating

To remove the organic residues from the surface of the SOI wafer, an RCA-1 cleaning recipe was used. Initially, 4 parts of H_2O, mixed with 1 part of ammonium hydroxide (27% NH_4OH), were heated on the hotplate to 70^oC. Then the mixture was removed from the hotplate and 1 part of hydrogen peroxide (30% H_2O_2) was added to it. The solution started to bubble and then the sample was soaked in it for 15 minutes, rinsed with DI water and dried with a dry N_2 gun. The hydrogen peroxide is a strong oxidizer and it grows an oxide layer on top of the silicon layer and subsequently, ammonium hydroxide, which is a mild oxide etchant, removes the oxide layer and cleans the surface.

The electron beam resist used in this work was ZEP-520A. It has two advantages over PMMA. First, it retains a uniform vertical profile as it erodes during etching and secondly it has a lower etch rate in chlorine plasma than PMMA. These two advantages lead to more uniformity in the fabricated structures, as well as near to 90^o sidewalls for the holes in the PCs.

After cleaning the surface of the SOI sample from residues, it was spin-coated with ZEP at 2000 RPM for 60 s to yield a ZEP layer of 480 to 500 nm thickness.

4.3 Electron Beam Lithography (EBL)

This step was the most critical step in fabricating the structure. The design contains various features that make it considerably more challenging to fabricate than a simple isolated PC cavity (MC). In particular, the cavity itself involves a variety of hole sizes, and the single mode ridge waveguide involves large continuous regions instead of holes. This diversity of pattern shapes and sizes requires considerable attention to the SEM beam current, gun alignment, lens centering, beam focus and astigmatism, etc.

Before starting to pattern on the main chips, in which the grating couplers and multimode waveguides were present, some samples were patterned and fabricated on SOI substrates to Figure out the proper SEM setting for fabrication of the design.

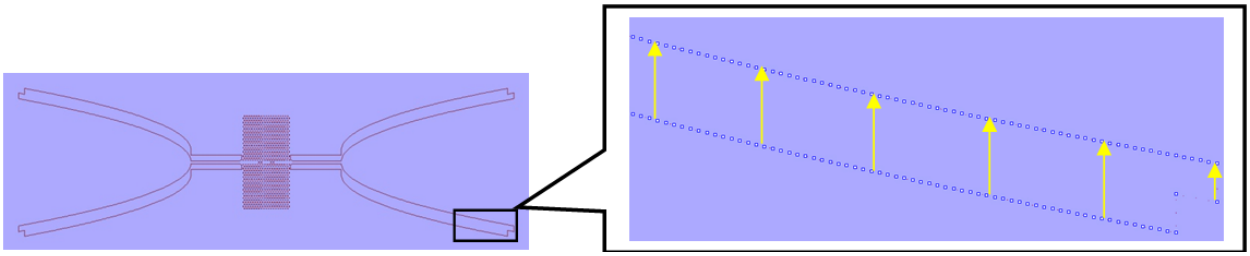

Figure 4.4 *The left image is the CAD design file pattern. The yellow arrows in the right image show the direction that the electron beam sweeps while patterning the tapered and ridge waveguides.*

4.2.1. **Creating the designCAD and run files**

The SEM used in this work is a JEOL model JSM-840A coupled with the Nabity Pattern Generating System™ (NPGS), which provides an interface between computer generated pattern designs and the motion of the electron beam in the SEM. The design files were generated by a Matlab™ code in the format of .DC2 DesignCAD™ files. This format is readable by the NPGS software to control the electron beam for patterning.

There are important points to note about the CAD file that was used in this work:

- The boundaries of the tapered and ridge waveguides are dashed lines with a line-type of 5. According to the NPGS manual, this line type makes the beam sweep from the same side (for example it sweeps always from left to right) (see Figure 4.4). Dr. Banaee found that this kind of line-type gives smooth side walls for the waveguides relative to line-type 1,at which the beam sweeps back and forth during patterning.
- For a closed polygon, the beam sweeping is parallel to one side of the polygon. The sweep side can be determined in the CAD file. For exactly the same polygon in a CAD file, the final fabricated pattern can be slightly different depending on the sweep side. The reason lies in the way that the NPGS software calculates the number of beam passes for a filled polygon (see page 45 of the NPGS manual). The best results were obtained when

one of the shortest sides in the taper region was selected (the sweeping direction is shown in Figure 4.4). There are also parameters which define the exposure conditions for a given CAD file. These parameters could be defined in the Run File Editor menu of the NPGS program. Here, a short introduction to them is given, for more information, please refer to the NPGS manual:

- **Line dose (nC/cm):** the amount of charge per unit of length that is delivered by the beam to the sample.
- **Line spacing:** the distance between adjacent lines in a filled polygon is the line spacing.
- **Center-to-Center spacing:** the spacing between adjacent exposure points is a line.
- **Dwell time:** the time interval in which the beam will expose a single point. Once the beam current and the line dose are set, the NPGS automatically calculates the dwell time.
- **Beam current (pAmp):** the amount of charge per unit of time that hits the sample surface. It was measured by an electrometer that was connected to a Faraday Cup that can be inserted and extracted from the SEM beam. Just before starting to pattern, the Faraday Cup was moved into the beam to measure this current and the value was entered into the Run File Editor.

Table 4.1 *The run file parameters used for patterning the design shown on Figure4.4.*

Parameters	***PC regular holes***	***Shrunk holes near to the PC waveguides and microcavity***	***Tapered and ridge waveguides***
Line dose (nC/cm)	*0.275, 0.3, 0.325*	*0.275, 0.3, 0.325*	*0.325, 0.35, 0.375*
Center-to- center spacing (nm)	*8.2397*	*8.2397*	*8.2397*
Line spacing (nm)	*39.8254*	*39.8254*	*39.8254*
Beam current(pAmp)	*2.1-2.6*	*2.1-2.6*	*2.1-2.6*
Magnification	*1000×*	*1000×*	*1000×*
Working distance (mm)	*15*	*15*	*15*

- The line doses for the holes (Table 4.1) are smaller than the case in which there is no ridge waveguide. The reason is that some fraction of electrons that hit the EB resist for patterning the ridge waveguides back scatter from the silicon surface and expose the resist at other areas near to the waveguides. This effect is known as the proximity effect. This effect makes it very difficult to predict the right line dose for different parts of the design. Therefore some test samples with wide ranges of line dose were fabricated, to find the proper values for the design.
- Small beam current produces smaller spot size [**Nabity2007**], which is good for patterning fine features but on the other hand it increases the writing time and also optimizing the SEM parameters (i.e. Focus, aperture centering, astigmatism, etc) is harder at lower beam currents because of the associated lower brightness and contrast of the SEM image. The beam current used in this work was in the range of 2.1 to 2.6 pA.

4.2.2. **SEM optimization:**

- Once the CAD and run files were ready, the SEM parameters were optimized before starting to pattern. The SOI wafers coated with ZEP were cleaved to small rectangles (10mm×6m). The patterns were written in rows parallel to the longer edge of the sample. Some graphite was put on the shorter sides of the sample using a pencil. This helps in focusing the SEM image on the sides of the sample. After loading the sample into the SEM the following steps were followed to optimize the SEM parameters:
- The acceleration voltage was increased to 30 kV. It was found by Dr. Murray McCutcheon that while patterning the PC holes, the 30kV voltage gives rise to more vertical sidewalls than 20kV. Also higher voltage means smaller beam spot size which is good for writing fine features [**Nabity2007**]. The voltage should be set at first, because other SEM parameters depend strongly on the acceleration voltage.
- In the second step, the gun alignment was checked. To align the gun, we had to adjust the tilt and shift of the gun. To do that we first focus on the gold sample to obtain a relatively sharp image on the “display CRT” then we pushed in the “WFM” button on the “DISPLAY MODE” panel and adjusted brightness and contrast on the “SE IMAGE”

panel so that the line scan profile of the sample was contained within about 2/3 of the maximum range. Then we switched the scan speed to "SR" and the scan mode to "LSP" to have a stationary line profile of the sample. After that, we adjusted the gun shift and tilt to maximize the contrast in the line profile. Then we turned down the filament current to have zero emission and turned it back up slowly and in the meanwhile we adjusted the gun shift and tilt to always maximize the contrast of the line profile on the CRT. We had to continue increasing the filament current to the point that the emission current saturates (filament current of around 260 μA). Once at the saturation value we turned the filament current back down again and repeated the procedure until we saw that by turning up the filament current knob the line profile would go to a first peak, drop back down, and then reach a second peak. The second peak is full saturation. Once we saw that, the gun was aligned and the best filament current to use for patterning would be the start of the second peak (the saturation plateau). *This step is extremely crucial for patterning because it leads to very stable beam current which is essential for a good patterning.*

- Then the stage was moved up to the focus of the SEM using the z working distance knob. Once the gold resolution standard (always mounted beside the sample) was observed in reasonably sharp focus on the screen, the aperture centering (also known as "wobble") was set.
- Then the fine-focus knob and the x and y astigmatism knobs were adjusted alternatively until the image of the gold particles (as small as 50 nm) became sharp.
- The Faraday Cup was moved under the beam by the x and y knobs of the translation stage and the beam current, which was monitored by the electrometer, was set to the values mentioned in Table 4.1 by using the coarse and fine probe-current knobs. By changing the coarse probe-current knob, the focus and the astigmatism change slightly, so another quick adjustment of them would be necessary after adjusting the beam current. Once both probe knobs (i.e. coarse and fine) reach to the end of their ranges, the variable resistor in the "gun bias" helped us to reduce the beam current further. To use that resistor, one should switch the gun bias from "Auto" to the "Manual" mode and then change it to get the right beam current.

Figure 4.5 *a) Top view of the sample inside the SEM. The dashed line shows a row of patterns. Each segment of the dashed line indicates a group of three patterns. The RHS yellow circle show the position, at which the focus and astigmatism adjustments were done. The LHS circle is the position for determining the amount of tilt across the sample.* ***b)*** *Another XZ view of the sample showing the tilt of the sample with respect to a horizontal line. Also the focusing spots are shown with yellow dots in part a.*

- After that, the coordinates of the corners of the wafer chip were measured and used as references for moving the x-y translation stages to pattern in the desired locations. The patterns were written form right to left across the sample.
- Since the sample surface and the gold sample were not at the exact same z level, the focus and the astigmatism were checked on the SOI wafer before patterning. We moved to the right edge of the sample, at the same y coordinate as we planned to write the pattern, and re-adjusted the focus and astigmatism using only the z-working distance knob or z-fine adjustment knob to physically bring back the sample surface to the focus of the beam (the focusing spot is shown by a yellow circle on the right edge of the sample in Figure 4.5). The graphite particles that we had put there before helped for this focusing step.
- Since the entire surface of the sample was not at the same level, some z correction was needed as we were moving across the sample during patterning to bring the sample surface back to focus. Once we had done all adjustments on a point in the right edge of the sample, we went to the left edge of the sample, at the same y-setting, and moved the sample vertically using the z-fine adjustment knob to sharpen the left edge. Then, by dividing the total z-displacement (ΔZ) to the distance between right and left focusing spots ΔX (both are shown in Figure 4.5a), we estimated the slope of the sample and from

that, we could Figure out the amount of z correction needed during patterning of each pattern at a distinct x point. It should be mentioned that the knob has a backlash, so corrections should always be done in one direction i.e. either clockwise or counterclockwise. Also, while mounting the sample onto the chuck, it is better to spend time for minimizing sample tilt.

- During all of these pre-adjustments, one must make sure not to expose the area that is planned to be patterned.
- After determining the tilt correction, the beam was moved back to the right side of the sample and we started to pattern (without exposing the area needed for patterning). After writing each set of patterns, the beam current was re-measured to make sure that it was stable. Otherwise, we readjusted the current by the fine probe current knob which has a negligible effect on other adjustments.

4.4 Sample Development

Once the patterning was complete, the sample was developed with the following recipe (Table 4.2).

The sample was held with a tweezers and dipped in o-xylene (CHROMASOLV PLUS, FOR HPLC, 98%) for one minute. Then immediately the sample was removed into another beaker of IPA and was dipped there for another minute. After that, the sample was blown with nitrogen gun to evaporate the solvent. The sample was smoothly agitated in both o-xylene and IPA.

Table 4.2 *Recipe for developing SOI samples coated with ZEP and patterned with EBL.*

	Chemical	***Time (s)***
Step 1	*o-xylene*	*60*
Step 2	*IPA*	*60*
Step3	*N2*	*Until the sample dries*

4.5 Etching

A Plasmaquest™ electron cyclotron resonance (ECR) etcher in the AMPEL Nanofabrication Facility was used for etching the e-beam patterns into the top silicon layer of the SOI wafer. The active ingredient in the plasma was chlorine. The plasma is generated by a microwave generator that uses the electron cyclotron effect for ionizing the chlorine molecules and atoms. The microwave is tuned to the cyclotron resonance frequency of electrons in the permanent magnetic field of the ion source. Since the gas pressure is small in the chamber, the recombination probability is small. The ions in the chamber are driven toward the sample by a radio-frequency (RF) field generator that provides a DC bias between the plasma source and the sample, which enhances the anisotropy of the etching.

The etching process has the following steps:

- Tuning plasma parameters: at this step the chuck that holds the backing wafer was loaded into the chamber without any sample on it. It was left there for 30 minutes to cool down and then plasma was run with the parameters of Table 4.3 for a few minutes to obtain stable plasma. During the run, the microwave parameters and RF parameters were tuned to minimize the microwave and RF reflected powers and also to have stable (i.e. without any wavering) plasma.
- Then, in the second run of plasma, a test sample (a bare SOI wafer coated with resist) was loaded to the chamber and after another 30 minutes of cooling down, was etched. Before loading the test sample, using the tip of tweezers, we scratched a few lines on the surface of the sample to remove the resist. After etching the test sample, the resist was removed completely and the depth of the scratches were measured with a Tencor™ profilometer to find the etch rate. For removing the resist after etching, the sample was exposed to UV light for 20 minutes and then rinsed with acetone.
- After figuring out the etch rate, we etched the patterned sample in the same way as the test sample. The etching time is determined by the etch rate calibration

described above, and the 200 nm thickness of the silicon layer of the sample. It is recommended to put some scratch marks near to the edges of the actual sample before etching. After etching, the colors of the marks provide a good indication of the etched depth. If the colors of the marks are dark grey, the silicon layer is etched all the way through. If they are greenish or bluish, the sample needs more etching. After etching the resist was removed as described above.

Table 4.3 *The ECR parameters for etching process.*

Parameters		***Step 1***	***Step 2***	***Step 3***
Step time (s)		*50*	*20*	*Variable*
Cl2 (sccm)		*0*	*0*	*30*
Backside He (Torr)		*5*	*5*	*5*
Process Pressure (mTorr)		*5.3*	*5.3*	*5.3*
Microwave powers (Watts)	*Incident*	*0*	*0*	*200*
	Reflected	*0*	*0*	*6 to 12*
Chiller Temperature (OC)		*5*	*5*	*5*
DC bias (V)		*0*	*0*	*-200 to -240*
RF powers (Watts)	*Incident*	*0*	*0*	*~30*
	reflected	*0*	*0*	*1 to 3*

During the etching process a few points should be noted:

- Chamber cleanness is very crucial for good etching. Contaminants can cause serious problems for the etching process. They cause unstable plasma, low etch rate, low DC bias that by itself gives rise to sloped sidewalls. To keep the chamber clean the following notes can be helpful:
- Before touching any movable component in the load lock that goes into the chamber during the loading process, wear a new pair of gloves.
- A very thin layer of vacuum grease should be used for attaching the sample to the carrier wafer: it should not squeeze out the sides after placing the sample on the wafer.

- The donut shaped metal piece which sits on top of the sample, should be wiped after each run to remove depositions from the previous run. This can improve the DC bias.
- The carrier wafer beneath the sample should be replaced after 2 to 4 runs.
- The Teflon o-ring that is between the backing wafer and the donut shape metal has a very big effect on the backside helium leak rate and contaminations inside the chamber and therefore the etch rate. The role of the helium flow under the backing wafer is to cool down the backing wafer and therefore the sample but it should not leak into the chamber because it disrupts the plasma. The Teflon o-ring should be in between the wafer and the donut shaped metal ring to prevent the helium from leaking to the chamber. This leakage leads to melting of another Viton^{TM} o-ring below the backing wafer that causes both unstable plasma and contamination of chamber (contamination comes from the melted Viton^{TM} o-ring). One sign of melting is that the backing wafer sticks to it and doesn't come off easily. Another indication of melting is a very dark black deposition layer on the backing wafer, which is from the melted o-ring during etching. The Teflon o-ring should be wiped after every few runs and reused.
- After wiping any part (like the Teflon o-ring) and also while replacing any part (like the backing wafer), the user should blow them with nitrogen gun to remove the dust from them.

CHAPTER 5 EXPERIMENTAL RESULTS

In this chapter, we present the results of the fabrication process as well as some transmission measurements for the grating couplers and multimode waveguides. Since the fabrication process for the final sample was not finished by the time of writing this thesis, this chapter does not contain any result for the trapping experiment.

5.1 Fabrication Results

The fabrication results are presented in two separate subsections: section 5.1.1 illustrates the uniformity of the samples using SEM images, and section 5.1.2 presents measurements of the *Q* factor from two cavities.

5.1.1. **The fabricated samples images**

After many attempts, we were able to fabricate the structure shown in Figure 4.4 of chapter 4. It was found that the structure is very sensitive to the following parameters and adjustments.

- The beam current: The beam current should be carefully measured and it should be very stable during patterning (less than a 0.1 pA change over a time interval of 20 minutes). The beam current should be measured several times during patterning.

- The focus and astigmatism: Because of large and variable features in this structure, the fabrication quality is strongly sensitive to the focus and astigmatism.
- Sample tilt: Since the correction made by the z-fine adjustment knob is not very accurate (backlash problems) it is best to carefully set the sample surface horizontal before loading the sample.
- Line doses: The line dose of the ridge waveguide and the cavity holes are different. It should be noted that because of the proximity effect these line doses affect each other.

The images of the fabricated samples are shown in Figure 5.1, 5.2, 5.3. The structure parameters, which we aimed to fabricate, were:

- A regular hole radius of 126nm (0.3a) for the cavity.
- A shrunk hole radius of 92nm (0.22a) for the side holes of the cavity and the nearest rows of holes to the PC waveguide.
- A width of 409nm for the ridge waveguide.

The images of some of the samples that turned out closest to these nominal parameters are shown in Figures 5.1, 5.2, 5.3.

We measured the regular holes radius in Figure 5.1d to be 132nm and the smaller holes' radius was found to be 92nm. Both of these values were very close to the expected design parameters. The Figure 5.2 shows some structures that we need them for transmission comparisons. For example the structure in Figure 5.2a can be used to find the PC waveguide loss for 14 periods of that. And Figure 5.2 b is showing the tapered and ridge waveguide connected together, which could be used for measurement of the transmittance of the waveguides. Figure 5.3 is showing a standalone cavity, radii of the holes in this figure are slightly different from, what we aimed for (Table5.1.

Table 5.1 *The radius of the holes in the fabricated (Figure 5.3) and simulated structures.*

	Fabrication	***Simulation***
Regular-size holes radius (nm)	*~140*	*126*
Shrunk holes radius (nm)	*~107*	*92*

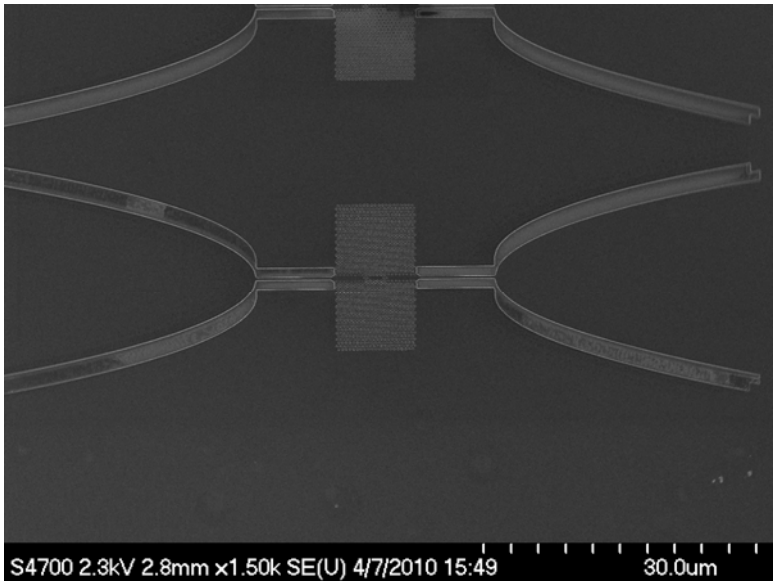
S4700 2.3kV 2.8mm x1.50k SE(U) 4/7/2010 15:49
30.0um

(a)

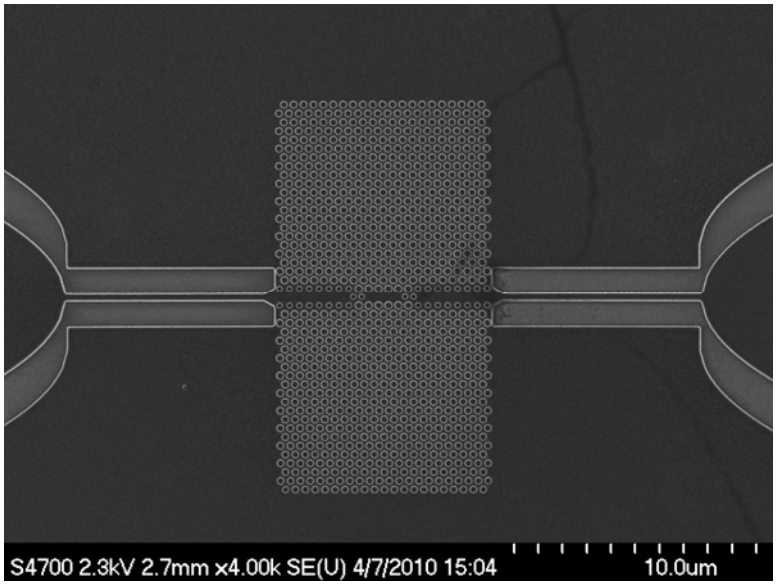
S4700 2.3kV 2.7mm x4.00k SE(U) 4/7/2010 15:04
10.0um

(b)

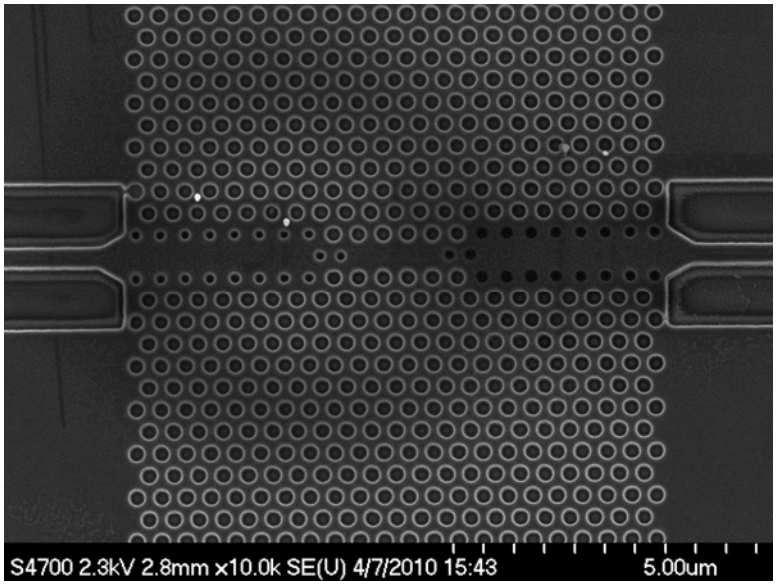

(c)

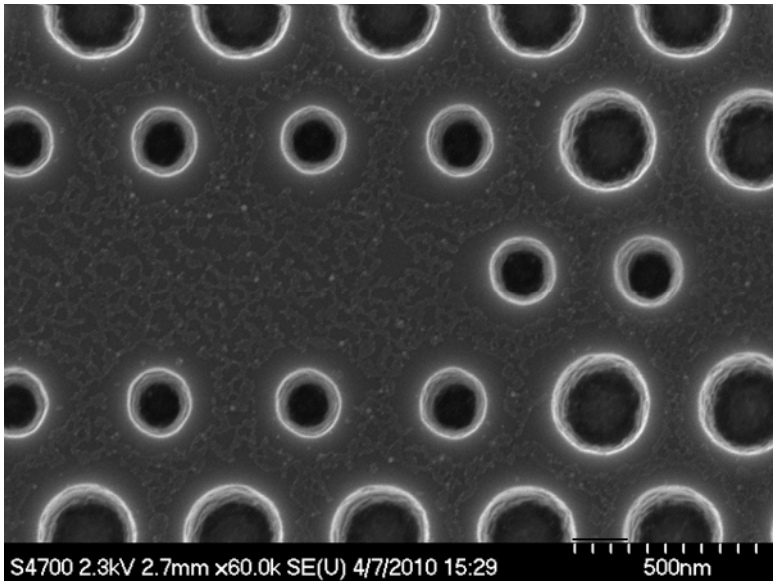

(d)

Figure 5.1 *The SEM images of a fabricated sample at different magnifications. It should be mentioned that the bright dotes on the surface of the sample and part of the roughness of the interior surface of the holes in part (d) is due to the QDs covered the surface for PL measurements.*

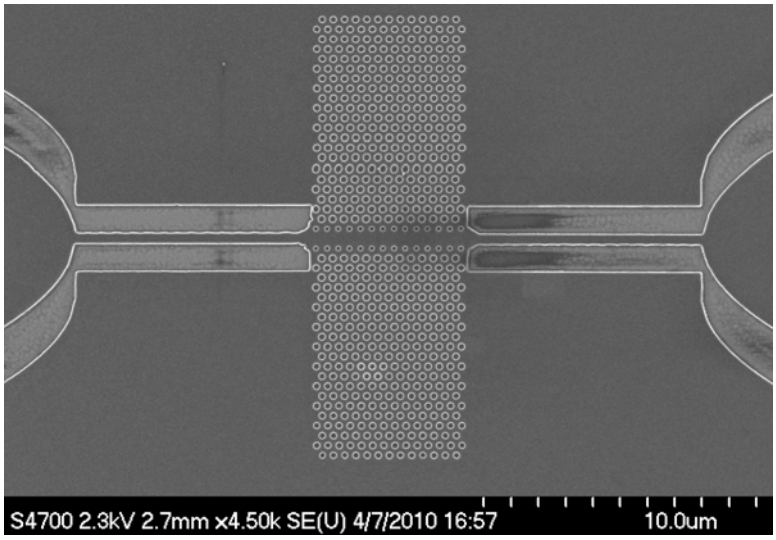

(a)

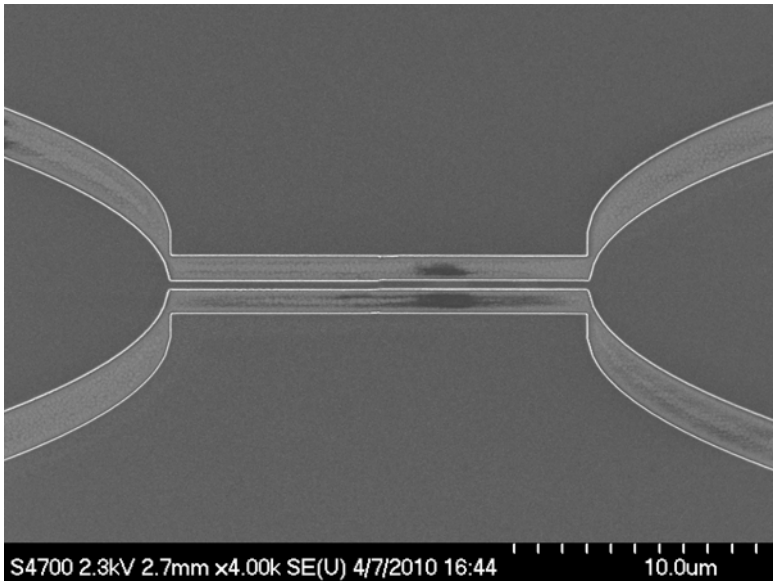

(b)

Figure 5.2 *(a) This structure was fabricated to be used for measuring the transmission efficiency of 14 periods of the modified PC waveguide. (b) The structure, which can be used for measuring the transmission efficiency of the ridge waveguides. The black areas in the images are due to the organic contaminations of the surface of the sample which was burned by electron beam of the SEM during focusing.*

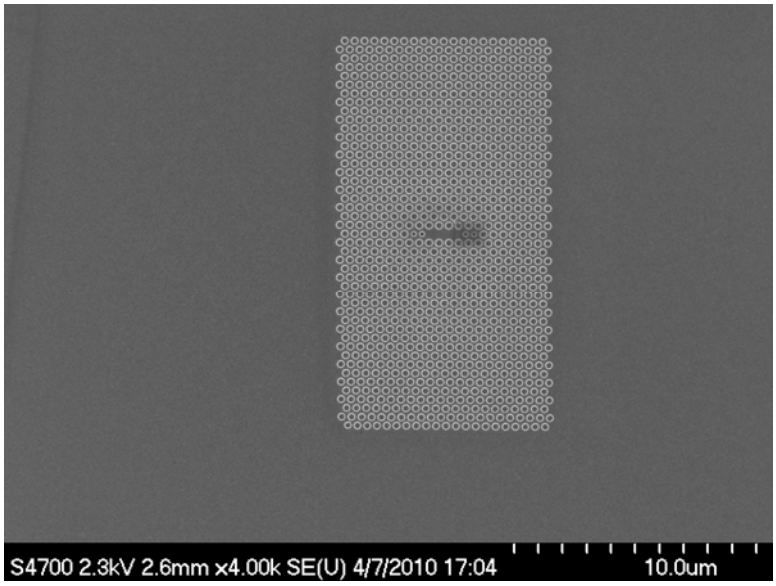

(a)

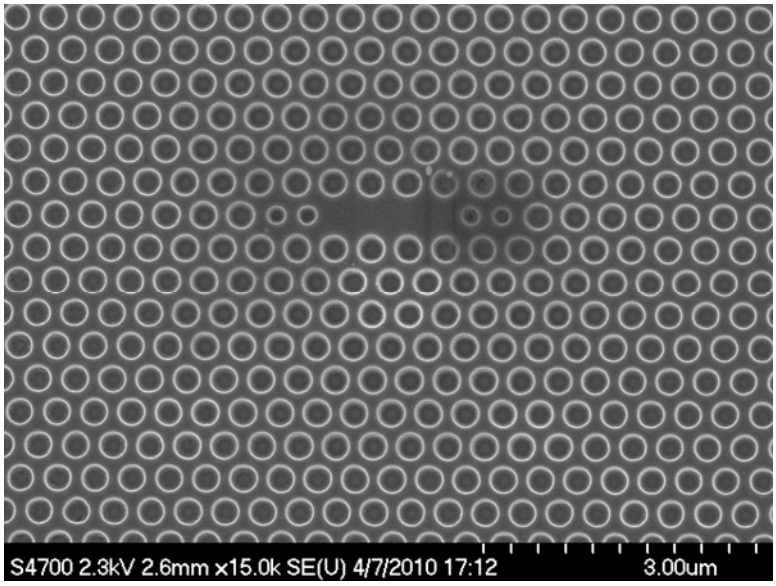

(b)

Figure 5.3 *The stand alone modified cavity with the parameters of Table 5.1 for estimating the Q_v. The black areas in the images are due to the organic contaminations of the surface of the sample which was burned by electron beam of the SEM during focusing.*

The uniformity and smoothness of the features in the fabricated structures are very promising.

5.1.2. *Q* factor measurements

Experimental *Q* factor measurements are usually done in a resonance scattering experiment. But for the case of non-undercut cavities, it was not possible to locate the exact position of the cavity using the infrared tunable laser, but the structure was observable using a HeNe laser source. Hence we adopted a way to measure the Q value by non-resonantly exciting the cavity using a HeNe laser.

We used an imaging PL setup for measuring the *Q* factors. The samples were dip coated in a PbSe QD solution and then moved into a cryostat. Then the cavities on the samples were irradiated by a HeNe laser. The PL spectra emitted by the QDs were recorded by an infrared spectrometer. The emission from the QDs, which are in resonance with the cavity and located near to the cavity, is enhanced with respect to the nonresonant QDs (Figure 5.4a). After fitting a Lorentzian function to the resonance peak, the FWHM of the fit gives the *Q* factor of the cavity (Figure 5.4b and c).

For the cavity of Figure 5.3, the *Q* factor was found to be about 3600 at a peak wavelength of 1567 nm (the cavity was not undercut and it was under vacuum in the cryostat). The vertical *Q* factor for these structure with hole radii of 126 and 92nm (Table 5.1) in a solvent medium (n=1.445) was estimated to be 3800. It should be mentioned that this number (i.e. 3800) was for 12 rings of holes around the center of the cavity but in the structure of Figure 5.3 there are less holes around the cavity. Also the fabricated cavity was covered with a thin layer of QDs, which would decrease the *Q*.

The *Q* factor for the cavity in Figure 5.1c was found to be 1050 at a resonant wavelength of 1559nm. Our simulation for this structure, with hole radii of 126nm and 92nm, in solvent, was ~ 1900 as reported in chapter 3.

Overall, the *Q* factors of the fabricated samples were found to be smaller than what we were expecting. Some of the reasons for these differences are the different sizes of the holes in the fabricated and simulated samples, the QD coatings of the fabricated samples, and the roughness in the surface of the fabricated samples.

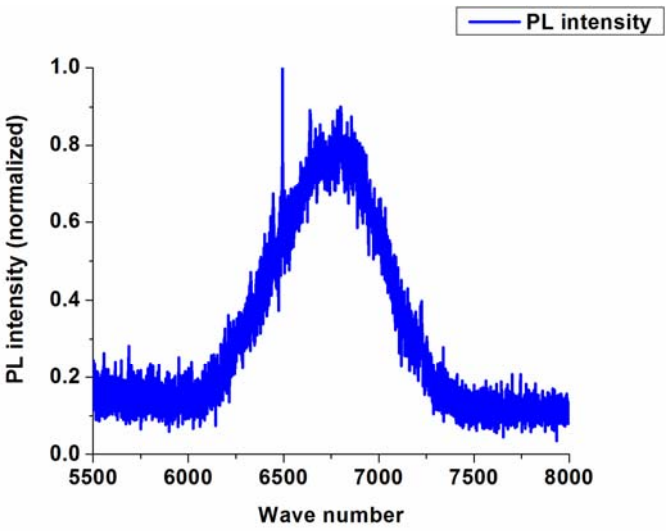

(a)

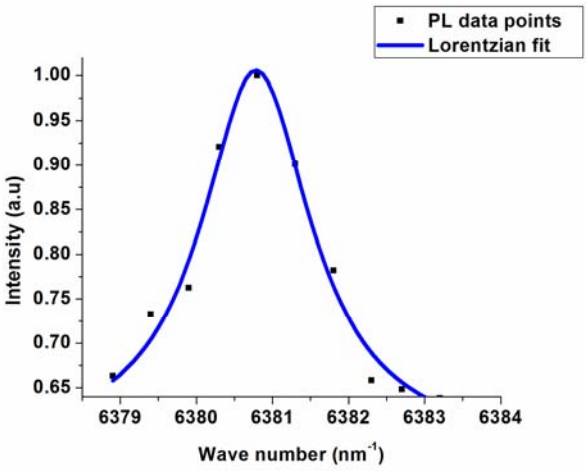

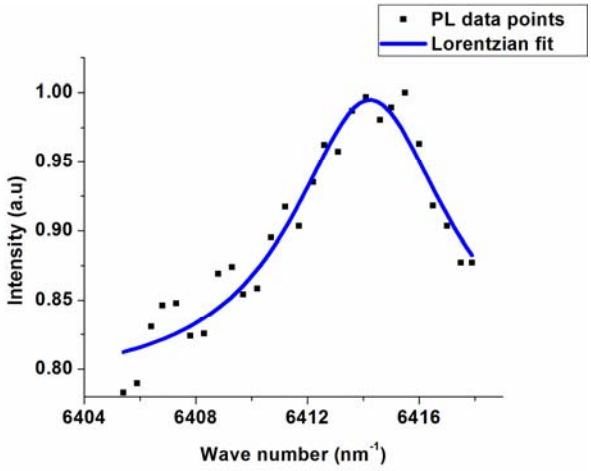

(b) *(c)*

Figure 5.4 *(a) A sample PL spectrum recorded during PL measurements. The broad peak corresponds to the PL of different Qs and the sharp peak is showing the PL intensity of the QDs that are in resonance with the cavity and due to Purcell effect are enhanced compared to the background PL. Part (b) and (c) are showing the PL data points including their Lorentzian fits for the standalone cavity and the structure of Figure 5.1c, respectively. The data points are showing the enhanced part of the PL spectra that correspond to the resonant QDs and the Lorentsian fits were used for estimating the Q factor of the cavities.*

5.2 Transmission Efficiency Measurements For The Multimode Waveguides

One other experiment, which we could do before fabricating the final structure, was measuring the transmission efficiency from the input grating coupler to the output grating coupler (structure of Figure 5.5).

5.2.1. **The experimental setup**

The experimental setup for measuring the transmission is shown in Figure 5.6. The sample containing the multimode waveguides was inside a cuvette and the cuvette was on top of a rotation stage. The laser source and mirror1 and a polarizer were on another rotation stage which was concentric with the sample stage. The light path is shown by the orange arrow in this Figure. The light from the source would hit the input grating coupler and the transmitted light was out-coupled from the output grating coupler toward the elliptical mirror. The rotation stages enabled us to vary the angle between the incident light and the surface of the sample, which was necessary for coupling of different wavelengths (light with different wavelengths couple at different angles to and from the gratings).

The focusing lens had a focal length of 25mm and the elliptical mirror had focal lengths of 15cm and 150cm, which resulted in a magnification of 10 times.

The output grating coupler was at the first focus (15cm) of the elliptical mirror and the magnified image of the grating coupler formed at the second focus (150cm). An InGaAs photodiode was located at the second focus of the mirror to measure the output power of the light beam. The source was a tunable cw laser with the wavelength range of 1520nm to 1630nm and power of ~5mW.

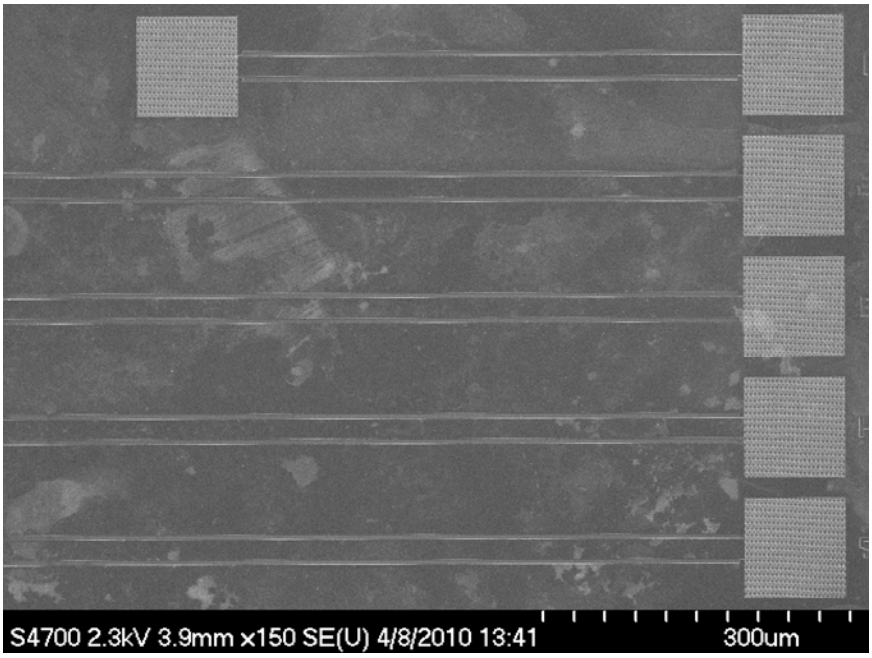

Figure 5.5 *The grating couplers and multimode waveguides. The input grating coupler are the right squares and only one of the output grating couplers is illustrated in this Figure.*

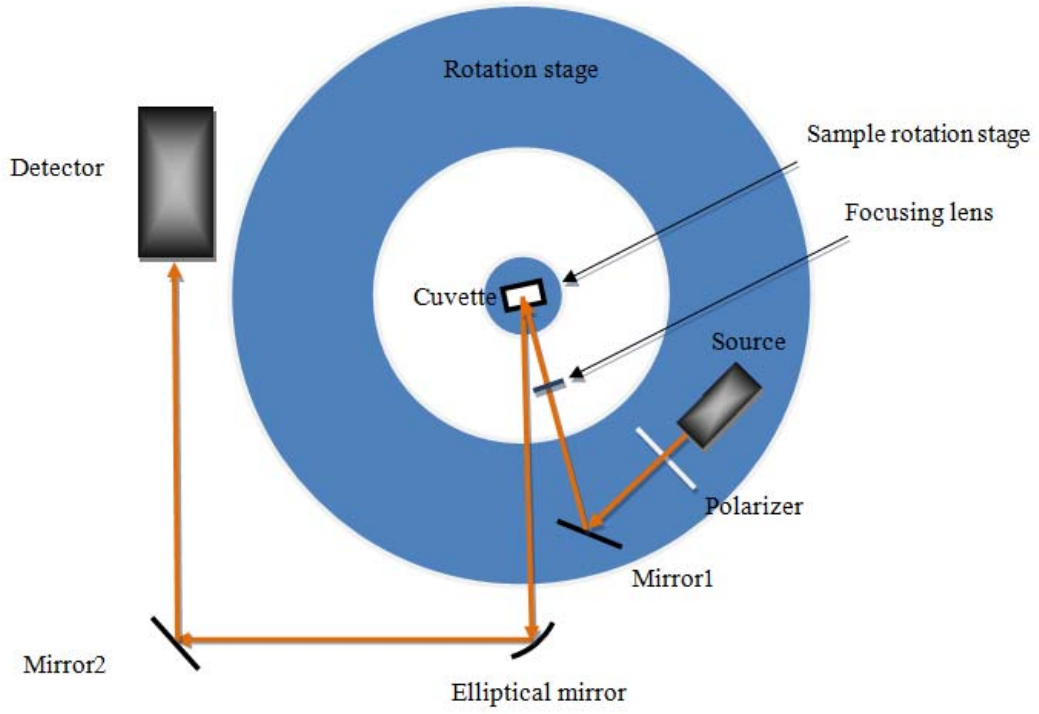

Figure 5.6 *The top view of the experimental set up for measuring the transmission efficiency from the input to output grating couplers of the sample shown in Figure 5.5.*

5.2.2. **Transmission measurement**

After setting up the experiment, we have measured the transmission efficiencies for different groups of grating coupler + multimode waveguides. As partially illustrated in Figure 5.7, there were 7 groups of grating coupler + multimode waveguides. Each group contained 5 samples of grating coupler + multimode waveguides. The grating coupler structures were the same in each group but the lengths of the waveguides were varying.

We have measured the transmission efficiencies for the groups that could transmit light at the working range of our source (i.e. 1520nm to 1630nm). The measurements were done in both air and chloroform medium. The results are shown in Figures 5.8a and 5.8b.

It was found that in both air and chloroform ~2% of the power injected to the input grating coupler was out coupled to the detector. Also transmission measurements in the two medium revealed a ~ 60nm red shift in the peak of the transmission efficiency after replacing air by the solvent. The transmission efficiency was almost constant (~2%) in different groups both with and without the solvent. This transmittance means that ~15% of the source power (~5mW) can reach to the middle of the multimode waveguides.

As it was mentioned, our final modified structure in chapter 3 is going to be located at the middle of the multimode waveguide. Knowing that ~15% of the laser power could reach to the middle of the multimode waveguides, we could estimate that ~10% of the source power could reach to the input ridge waveguide. This estimation was important to approximate the amount of force on the nanoparticles, because the results from the force calculations in chapter 3 were normalize to the power inside the input ridge waveguide. Thus overall we estimate having about 0.5mW delivered to the input ridge waveguide.

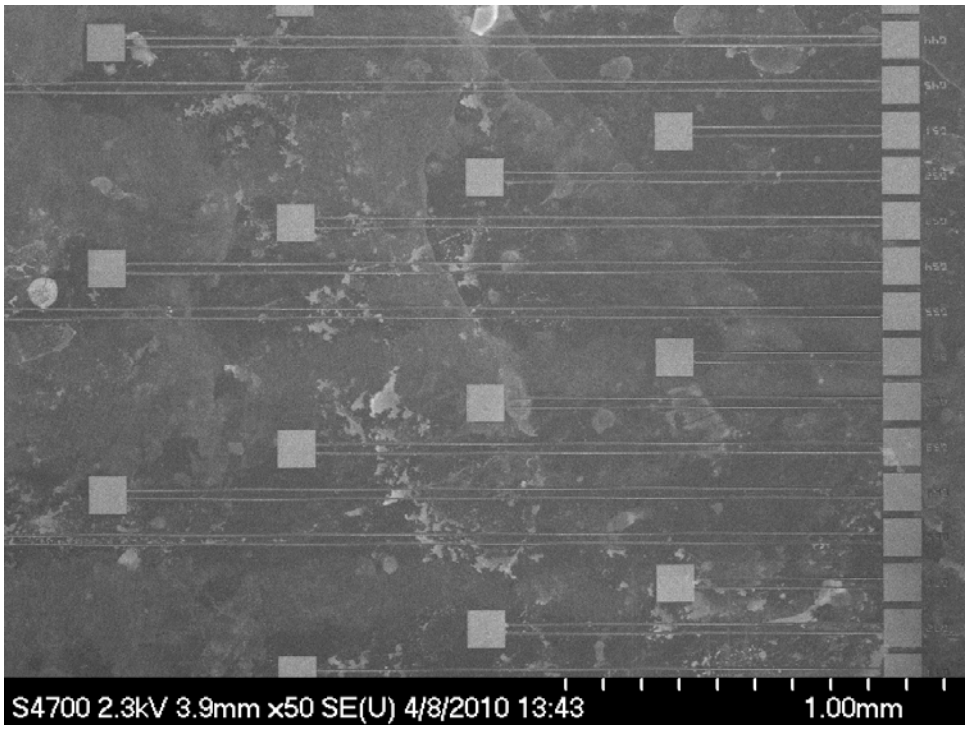

Figure 5.7 *The top view of a sample with groups of grating couplers + multimode waveguide structures. The final modified structures, designed in chapter3, are to be written in the middle of the waveguides of this sample.*

After we had calculated the trapping force and the corresponding potential energy associated with this input power, we found the trapping potential energy to be ~60kT. This energy was for a 50nm radius dielectric particle (n=1.49) located 175nm from the center of the cavity. The minimum potential energy to overcome the random force of the medium (Brownian motion) is typically ~10kT. So the radiation force would suffice to trap the particle if the final fabricated samples have good enough qualities.

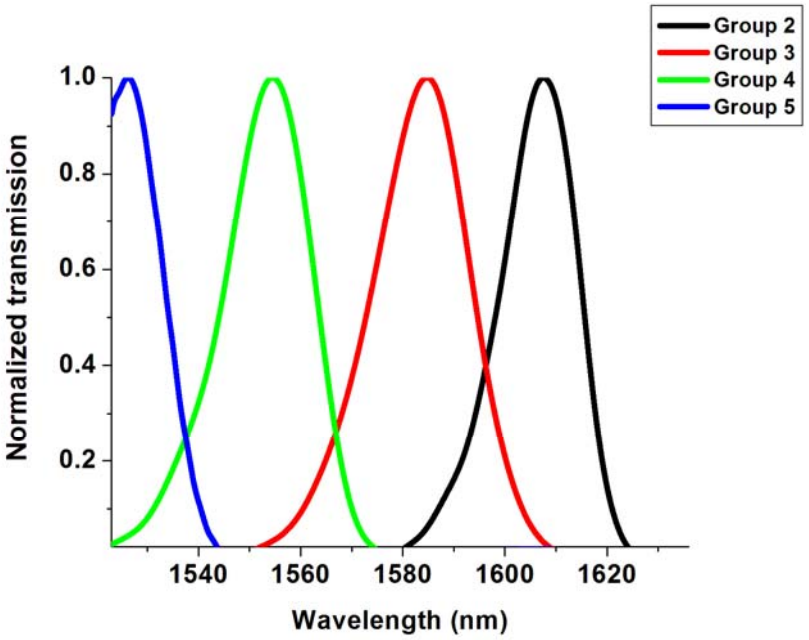

(a)

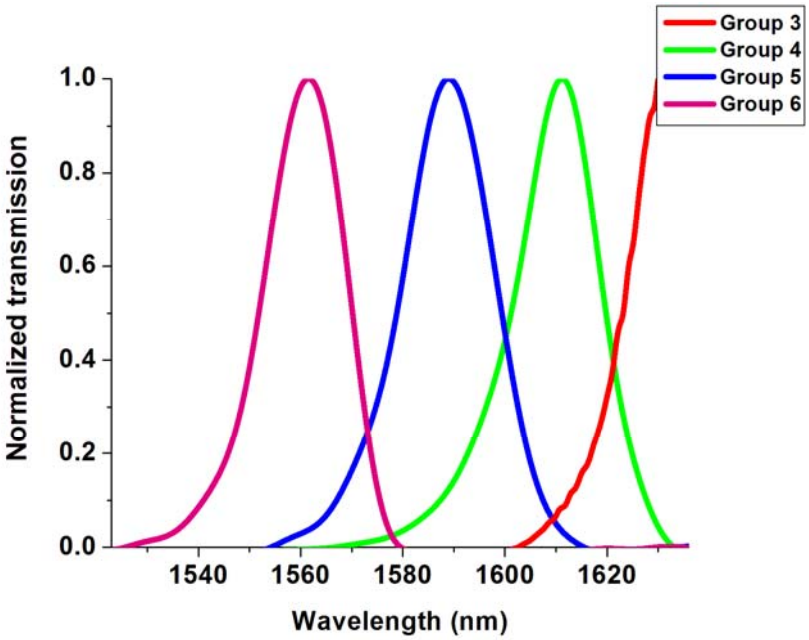

(b)

Figure 5.8 *(a) The transmission efficiencies of 4 different groups in air. All of these measurements were done on the shortest waveguide of each group. Efficiencies are normalized. (b) Transmission measurement in chloroform for 4 different groups that were in the range of the laser.*

CHAPTER 6 CONCLUSION AND FUTURE WORK

6.1 Conclusion

The objective of this project was to design and fabricate a photonic crystal cavity structure in SOI that should offer enough optical force to trap a ~ 50 nm radius dielectric sphere at the peak antinode of the cavity, given a 5 mW cw diode laser source tunable from 1530 nm to 1620 nm. The device has to function in an organic solvent environment, which makes its design more complicated than the "free standing in vacuum" structures more typically used.

Finite difference time domain simulations were used to design a symmetric (input/output) structure that includes on each side, a parabolic tapered waveguide, from a width of 22 μm to 409 nm that adjoins a 196 nm × 409 nm ridge waveguide which couples to a photonic crystal waveguide via a sub-wavelength tapered region. The photonic crystal waveguide is 7 periods (of a triangular photonic crystal along the Γ-K direction) long before encountering a two-hole "tunnel barrier" that separates it from a 3 missing hole (L3) microcavity. The structure is designed to operate in a solvent with refractive index 1.445, which is close enough to the SiO_2 buffer layer index (n=1.44427), that there is no need to undercut the sample.

The final design includes several subtle but effective modifications of a uniform triangular lattice planar photonic crystal with a bandgap centered near 1.56 μm, with a straight "one missing hole" photonic crystal waveguide separated by two holes from a standard L3 cavity. The row of holes directly adjacent to the photonic crystal waveguides were decreased in radius by 27%, from 126nm to 92.4nm, in order to increase the group velocity and minimize propagation losses in the waveguide section. The two holes on either side of the L3 cavity were first shifted and shrunk to maximize Q_v for an isolated cavity, and then readjusted when

integrated with the waveguides in order to have a structure with the highest possible Q value, while having $Q_v = Q_w$. This condition optimizes the energy stored in the cavity mode for a given incident power, and also the overall transmission on resonance. Simulations suggest that the design should have a Q of ~ 1900, and a optimum on-resonance transmission from ridge waveguide to ridge waveguide of 18%.

The vertical force right above the mode's central antinode was calculated "exactly" using the Maxwell stress tensor, and approximately, using the gradient force-dipole approximation. The two results agree very well assuming a 50 nm radius polymer particle (assumed to have a 5 nm PbSe nanocrystal at its centre). Assuming 0.5 mW of incident power in the input ridge waveguide, the calculated vertical trapping force was ~ 8 fN when the particle is 175 nm above the surface. This can be translated into a trapping potential of ~ 60 times kT. It is usually assumed that robust optical trapping requires a trapping potential of 10 times kT, so this design is able to trap a 50nm radius polymer particle by using the radiation force near to the surface of the Si slab.

The design proved difficult to fabricate using ebeam lithography and chlorine plasma etching, owning mostly to the variety of hole sizes and feature shapes (ridge waveguides and small holes). However, good quality samples have now been successfully fabricated on three independent occasions, and this thesis documents many key parameters that must be controlled in the lithography and etching processes to ensure success.

The cavity enhanced photoluminescence emission from fabricated samples that had a layer of PbSe nanocrystals deposited on them was measured in order to estimate the cavity Q values. Control samples that had isolated cavities (no waveguide coupling) showed a Q value of ~ 3600, corresponding to Q_v. The Q value for the full sample including input and output waveguides was 1050. This implies that Q_w ~1480. The design was for Q_v to equal Q_w, so this set of samples indicates the complete sample may be slightly off ideal coupling conditions, but the results are actually very encouraging. The resonant frequency measured (1559nm), compare to the design frequencies of (1567nm).

SEM images of the fabricated samples indicate very uniform hole sizes, smooth waveguide side walls, and good discrimination of the different hole radii in the complicated design. Overall the fabrication results are extremely encouraging.

These structures are to be ultimately fabricated in the middle of 1 mm long, 20 μm wide multimode waveguides that already have relatively efficient grating couplers on each end. As they must operate in a solvent environment for the optical trapping experiment, the overall transmission spectra of several groups of these input/output coupler structures were spectrally resolved using a tunable diode laser. The coupling efficiencies were ~ 10% per grating using a non-optimized focusing lens, and the effect of the solvent was to shift the resonant frequencies of each coupler by ~ 60 nm to the blue. This is valuable information, and suggests that the focusing geometry should be modified to reach the optimum coupling efficiency for these gratings, of ~ 25%.

6.2 Recommendations For Future Work

Everything is set to fabricate the designed structures in the existing input/output couplers. As reported in the thesis, several other test structures have been designed and fabricated to measure the propagation losses and waveguide-to-waveguide coupling efficiencies of the design, independent of the cavities.

Assuming that the measured optical response of the full structures is consistent with simulations, then attempts to trap various sized dielectric particles should commence as soon as possible. Because the current estimate for the maximum trapping force suggests that it may be challenging to reach the required forces with this design, ideas for increasing the cavity Q should also be explored.

The other important task is to model the influence of the resonant nature of the polarizability of the PbSe nanocrystal assumed to be embedded in the polymer spheres. It is possible that this might act to enhance the trapping force of the very particles that are ideal for studying CQED (those near resonant with the cavity mode).

BIBLIOGRAPHY

Akahane2005 Akahane, Y., Asano, T., Song, B.-S. & Noda, S. *Fine-tuned high-Q photonic-crystal nanocavity,* Opt. Express, OSA, 2005, Vol. 13(4), pp. 1202-1214

Akahane2003 Akahane, Y., Asano, T., Song, B.-S. & Noda, S. *High-Q photonic nanocavity in a two-dimensional photonic crystal* Nature, 2003, Vol. 425(6961), pp. 944-947

Andreani2004 Andreani, L.C., Gerace, D. & Agio, M. *Gap maps, diffraction losses, and exciton-polaritons in photonic crystal slabs,* Photonics and Nanostructures Fundamentals and Applications, 2004, Vol. 2(2), pp. 103-110

Ashkin1970a Ashkin, A.*Atomic-Beam Deflection by Resonance-Radiation Pressure* Phys. Rev. Lett., American Physical Society, 1970, Vol. 25(19), pp. 1321-

Ashkin1986 Ashkin, A., Dziedzic, J.M., Bjorkholm, J.E. & Chu, S. *Observation of a single-beam gradient force optical trap for dielectric ps* Opt. Lett., OSA, 1986, Vol. 11(5), pp. 288-290

Banaee2007 Banaee, M.G., Pattantyus-Abraham, A.G., McCutcheon, M.W., Rieger, G.W. & Young, J.F. *Efficient coupling of photonic crystal microcavity modes to a ridge waveguide* Applied Physics Letters, AIP, 2007, Vol. 90(19), pp. 193106

Barclay2005 Barclay, P., Srinivasan, K. & Painter, O. *Nonlinear response of silicon photonic crystal microresonators excited via an integrated waveguide and fiber taper* Opt. Express, OSA, 2005, Vol. 13(3), pp. 801-820

Borselli2006 Borselli, M., Johnson, T.J. & Painter, O. *Measuring the role of surface chemistry in silicon microphotonics* Applied Physics Letters, Amer Inst Physics, 2006, Vol. 88(13), pp. 131114

Borselli2004 Borselli, M., Srinivasan, K., Barclay, P.E. & Painter, O.*Rayleigh scattering, mode coupling, and optical loss in silicon microdisks* Applied Physics Letters, Amer Inst Physics, 2004, Vol. 85(17), pp. 3693-3695

Bose2009 Bose, R., Gao, J., McMillan, J.F., Williams, A.D. & Wong, C.W. *Cryogenic spectroscopy of ultra-low density colloidal lead chalcogenide quantum dots on chip-scale optical cavities towards single quantum dot near-infrared cavity QED* Opt. Express, OSA, 2009, Vol. 17(25), pp. 22474-22483

Bose2007 Bose, R., Yang, X., Chatterjee, R., Gao, J. & Wong, C.W. *Weak coupling interactions of colloidal lead sulphide nanocrystals with silicon photonic crystal nanocavities near 1.55 mu m at room temperature* Appl. Phys. Lett., AIP, 2007, Vol. 90(11), pp. 111117-3

Bustamante2000 Bustamante, C., Macosko, J.C. & Wuite, G.J.L. *Grabbing the cat by the tail: manipulating molecules one by one* Nat Rev Mol Cell Biol, Macmillan Magazines Ltd., 2000, Vol. 1(2), pp.130-136

Cai2000 Cai, M., Painter, O. & Vahala, K.J. *Observation of Critical Coupling in a Fiber Taper to a Silica-Microsphere Whispering-Gallery Mode System* Phys. Rev. Lett., American Physical Society, 2000, Vol. 85(1), pp. 74-

Chu1985 Chu, S., Hollberg, L., Bjorkholm, J.E., Cable, A. & Ashkin, A. *Three-dimensional viscous confinement and cooling of atoms by resonance radiation pressure* Phys. Rev. Lett., American Physical Society, 1985, Vol. 55(1), pp. 48-

Chutinan2001 Chutinan, A., Mochizuki, M., Imada, M. & Noda, S. *Surface-emitting channel drop filters using single defects in two-dimensional photonic crystal slabs* Applied Physics Letters, AIP, 2001, Vol. 79(17), pp. 2690-2692

DiVincenzo2000 DiVincenzo, D.P *The Physical Implementation of Quantum Computation* Fortschritte der Physik, 2000, Vol. 48(9-11), pp. 771-783

Fan2004 Fan, W.S.Z.W.S. *Temporal coupled-mode theory and the presence of non-orthogonal modes in lossless multimode cavities* IEEE, 2004, Vol. 40, pp. 1511 - 1518

Finer1994 FINER, J.T., SIMMONS, R.M. & SPUDICH, J.A. *Single Myosin Molecule Mechanics - Piconewton Forces And Nanometer Steps* Nature, Macmillan Magazines Ltd, 1994, Vol. 368(6467), pp. 113-119

Foresi1997 Foresi, J.S., Villeneuve, P.R., Ferrera, J., Thoen, E.R., Steinmeyer, G., Fan, S., Joannopoulos, J.D., Kimerling, L.C., Smith, H.I. & Ippen, E.P. *Photonic-bandgap microcavities in optical waveguides* Nature, 1997, Vol. 390(6656), pp. 143-145

Fushman2005 Fushman, I., Englund, D. & VuCkovic, J. *Coupling of PbS quantum dots to photonic crystal cavities at room temperature* Appl. Phys. Lett., AIP, 2005, Vol. 87(24), pp. 241102-3

Gorodetsky1996 Gorodetsky, M.L., Savchenkov, A.A. & Ilchenko, V.S. *Ultimate Q of optical microsphere resonators* Opt. Lett., OSA, 1996, Vol. 21(7), pp. 453-455

Grillet2003 Grillet, C., Letartre, X., Seassal, C., Rojo-Romeo, P., Viktorovitch, P., Le Vassor d'Yerville, M., Cassagne, D., Albert, J., Deahese, O., Bertru, N. & Le Corre, A. *Low loss single line photonic crystal waveguide on InP membrane* Proceedings of the International Conference on Superlattices, Nano-structures and Nano-devices ICSNN 2002 o-structures and Nano-devices ICSNN 2002 Physica E: Low-dimensional Systems and Nanostructures, 2003, Vol. 17, pp. 472-474

Gerard2003 Gérard, J.-M. *Solid-State Cavity-Quantum Electrodynamics with Self-Assembled Quantum Dots* Single Quantum Dots, 2003, pp. 269-314

Harada1996 Harada, Y. & Asakura, T. *Radiation forces on a dielectric sphere in the Rayleigh scattering regime* Optics Communications, 1996, Vol. 124(5-6), pp. 529-541

Hennessy2007 Hennessy, K., Badolato, A., Winger, M., Gerace, D., Atature, M., Gulde, S., Falt, S., Hu, E.L. & Imamoglu, A.*Quantum nature of a strongly coupled single quantum dot-cavity system* Nature, 2007, Vol. 445(7130), pp. 896-899

Iida2008 Iida, T. & Ishihara, H. *Nano-Optical Manipulation Using Resonant Radiation Force* Progress in Nano-Electro-Optics VI, 2008, pp. 115-168

Imamoglu1999 Imamoglu, A., Awschalom, D.D., Burkard, G., DiVincenzo, D.P., Loss, D., Sherwin, M. & Small, A. *Quantum Information Processing Using Quantum Dot Spins and Cavity QED* Phys. Rev. Lett., American Physical Society, 1999, Vol. 83(20), pp. 4204-

Jackson1975 Jackson, J.D., *Classical electrodynamics*. John Willey & Sons, New York, 1975

Jewell1989 Jewell, J.L., MCCALL, S.L., LEE, Y.H., SCHERER, A., GOSSARD, A.C. & ENGLISH, J.H. *Lasing Characteristics Of Gaas Microresonators* Applied Physics Letters, Amer Inst Physics, 1989, Vol. 54(15), pp. 1400-1402

Joannopoulos2008 Joannopoulos, J.D., Johnson, S.G., Winn, J.N., Meade, R.D., *Photonic Crystals: Molding the Flow of Light (Second Edition)*. Princeton University Press, 2008

John1987 John, S. *Strong localization of photons in certain disordered dielectric superlattices* Phys. Rev. Lett., American Physical Society, 1987, Vol. 58(23), pp. 2486-

Kellermayer1997 Kellermayer, M.S., Smith, S.B., Granzier, H.L. & Bustamante, C. *Folding-Unfolding Transitions in Single Titin Molecules Characterized with Laser Tweezers* Science, 1997, Vol. 276(5315), pp. 1112-1116

Kim2004 Kim, G.-H., Lee, Y.-H., Shinya, A. & Notomi, M. *Coupling of small, low-loss hexapole mode with photonic crystal slab waveguide mode* Opt. Express, OSA, 2004, Vol. 12(26), pp. 6624-6631

Lin1998 Lin, S.Y., Fleming, J.G., Hetherington, D.L., Smith, B.K., Biswas, R., Ho, K.M., Sigalas, M.M., Zubrzycki, W., Kurtz, S.R. & Bur, J. *A three-dimensional photonic crystal operating at infrared wavelengths* Nature, Macmillan Magazines Ltd., 1998, Vol. 394(6690), pp. 251-253

Little2004 Little, B., Chu, S., Absil, P., Hryniewicz, J., Johnson, F., Seiferth, F., Gill, D., Van, V., King, O. & Trakalo, M. *Very high-order microring resonator filters for WDM applications* Photonics Technology Letters, IEEE Photonics Technology Letters, IEEE DOI - 10.1109/LPT.2004.834525, 2004, Vol. 16(10), pp. 2263-2265

Loss1998 Loss, D. & DiVincenzo, D.P. *Quantum computation with quantum dots* Phys. Rev. A, American Physical Society, 1998, Vol. 57(1), pp. 120-

Mandal2009 Mandal, S., Serey, X. & Erickson, D. *Nanomanipulation Using Silicon Photonic Crystal Resonators* Nano Letters, American Chemical Society, 2009, pp. -

Martini2002 Martini, F.D. & Monroe, C. F. De Martini and C. Monroe, editors. Experimental Quantum Computation and Information: Proceedings of the International School of Physics Enrico Fermi", Course CXLVIII. IOS *Press, Amsterdam, 2002* IOS Press, 2002

McKeever2004 McKeever, J. T. T. *Trapped atoms in cavity QED for quantum optics and quantum information Caltech,* 2004, -

Mitsugi2003 Mitsugi, S., Shinya, A., Kuramochi, E., Notomi, M., Tshchizawa, T. & Watanabe, T. *Resonant tunneling wavelength filters with high Q and high transmittance based on photonic crystal slabs* Lasers and Electro-Optics Society, 2003. LEOS 2003. The 16th Annual Meeting of the IEEE 2003, Vol. 1, pp. 214-215 vol.1 other

Nabity2007 Nabity, J., Compbell, L., Zhu, M. & Zhou, W. *E-beam Nanolithography Integrated with Scanning Electron Microscope* Scanning Microscopy for Nanotechnology, 2007, pp. 120-151

Nicholls1901 Nicholls, G.F. Hull. A Preliminary communication on the pressure of heat and light radiation. *Phys. Rev. (Series I)* 13, No. 5, 307-320 P. 1901

Noda2000 Noda, S., Chutinan, A. & Imada, M. *Trapping and emission of photons by a single defect in a photonic bandgap structure* Nature, 2000, Vol. 407(6804), pp. 608-610

[Noda2007 Noda, S., Fujita, M. & Asano, T. *Spontaneous-emission control by photonic crystals and nanocavities* Nat Photon, 2007, Vol. 1(8), pp. 449-458

[Novotny2006 Novotny, L., Hecht, B., *Principles of nano-optics*. Cambridge Univeristy Press, 2006

Onoa2003 Onoa, B., Dumont, S., Liphardt, J., Smith, S.B., Tinoco, Ignacio, J. & Bustamante, C. *Identifying Kinetic Barriers to Mechanical Unfolding of the T. thermophila Ribozyme* Science, 2003, Vol. 299(5614), pp. 1892-1895

Park2004 Park, H.-G., Kim, S.-H., Kwon, S.-H., Ju, Y.-G., Yang, J.-K., Baek, J.-H., Kim, S.-B. & Lee, Y.-H. *Electrically Driven Single-Cell Photonic Crystal Laser* Science, 2004, Vol. 305(5689), pp. 1444-1447

Pattantyus-Abraham2009 Pattantyus-Abraham, A.G., Qiao, H., Shan, J., Abel, K.A., Wang, T.-S., van Veggel, F.C.J.M. & Young, J.F. *Site-Selective Optical Coupling of PbSe Nanocrystals to Si-Based Photonic Crystal Microcavities* Nano Letters, American Chemical Society, 2009, Vol. 9(8), pp. 2849-2854

Pelton2002a Pelton, M., Santori, C., VucÌ†koviÄ‡, J., Zhang, B., Solomon, G.S., Plant, J. & Yamamoto, Y. *Efficient Source of Single Photons: A Single Quantum Dot in a Micropost Microcavity* Phys. Rev. Lett., American Physical Society, 2002, Vol. 89(23), pp. 233602-

Pelton2002 Pelton, M., Vukovic, J., Solomon, G., Scherer, A. & Yamamoto, Y. *Three-dimensionally confined modes in micropost microcavities: quality factors and Purcell factors* Quantum Electronics, IEEE Journal of Quantum Electronics, IEEE Journal of DOI - 10.1109/3.980269, 2002, Vol. 38(2), pp. 170-177

Peter2005 Peter, E., Senellart, P., Martrou, D., Lemaître, A., Hours, J., Gérard, J.M. & Bloch, J. *Exciton-Photon Strong-Coupling Regime for a Single Quantum Dot Embedded in a Microcavity* Phys. Rev. Lett., American Physical Society, 2005, Vol. 95(6), pp. 067401-

Phillips1985 Phillips, W.D., Prodan, J.V. & Metcalf, H.J. *Laser cooling and electromagnetic trapping of neutral atoms* J. Opt. Soc. Am. B, OSA, 1985, Vol. 2(11), pp. 1751-1767

Popovic2006 Popovíc, M.A., Barwicz, T., Watts, M.R., Rakich, P.T., Socci, L., Ippen, E.P., Kärtner, F.X. & Smith, H.I. *Multistage high-order microring-resonator add-drop filters* Opt. Lett., OSA, 2006, Vol. 31(17), pp. 2571-2573

Preble2007 Preble, S.F., Xu, Q. & Lipson, M. *Changing the colour of light in a silicon resonator* Nat Photon, 2007, Vol. 1(5), pp. 293-296

Rahmani2006 Rahmani, A. & Chaumet, P.C. *Optical trapping near a photonic crystal* Opt. Express, OSA, 2006, Vol. 14(13), pp. 6353-6358

Reithmaier2004 Reithmaier, J.P., Sek, G., Loffler, A., Hofmann, C., Kuhn, S., Reitzenstein, S., Keldysh, L.V., Kulakovskii, V.D., Reinecke, T.L. & Forchel, A. *Strong coupling in a single quantum dot-semiconductor microcavity system* Nature, 2004, Vol. 432(7014), pp. 197-200

Ryu2004 Ryu, H.-Y., Notomi, M., Kim, G.-H. & Lee, Y.-H. *High quality-factor whispering-gallery mode in the photonic crystal hexagonal disk cavity* Opt. Express, OSA, 2004, Vol. 12(8), pp. 1708-1719

Ryu2003 Ryu, H.-Y., Notomi, M. & Lee, Y.-H. *High-quality-factor and small-mode-volume hexapole modes in photonic-crystal-slab nanocavities* Applied Physics Letters, AIP, 2003, Vol. 83(21), pp. 4294-4296

Schubert2005 Schubert, E.F. & Kim, J.K. *Solid-State Light Sources Getting Smart* Science, 2005, Vol. 308(5726), pp. 1274-1278

Smith1996 Smith, S.B., Cui, Y. & Bustamante, C. *Overstretching B-DNA: The Elastic Response of Individual Double-Stranded and Single-Stranded DNA Molecules* Science, 1996, Vol. 271(5250), pp. 795-799

Song2005 Song, B.-S., Noda, S., Asano, T. & Akahane, Y. *Ultra-high-Q photonic double-heterostructure nanocavity* Nat Mater, 2005, Vol. 4(3), pp. 207-210

Srinivasan2002 Srinivasan, K. & Painter, O. *Momentum space design of high-Q photonic crystal optical cavities* Opt. Express, OSA, 2002, Vol. 10(15), pp. 670-684

Srinivasan2005 Srinivasan, K., Stintz, A., Krishna, S. & Painter, O. *Photoluminescence measurements of quantum-dot-containing semiconductor microdisk resonators using optical fiber taper waveguides* Phys. Rev. B, American Physical Society, 2005, Vol. 72(20), pp. 205318-

Takano2006 Takano, H., Song, B.-S., Asano, T. & Noda, S. *Highly efficient multi-channel drop filter in a two-dimensional hetero photonic crystal* Opt. Express, OSA, 2006, Vol. 14(8), pp. 3491-3496

Tanabe2007 Tanabe, T., Shinya, A., Kuramochi, E., Kondo, S., Taniyama, H. & Notomi, M. *Single point defect photonic crystal nanocavity with ultrahigh quality factor achieved by using hexapole mode* Applied Physics Letters Applied Physics Letters DOI - 10.1063/1.2757099, 2007, Vol. 91(2), pp. 021110-021110-3

Tskhovrebova1997 Tskhovrebova, L., Trinick, J., Sleep, J.A. & Simmons, R.M. *Elasticity and unfolding of single molecules of the giant muscle protein titin* Nature, 1997, Vol. 387(6630), pp. 308-312

Vahala2003 Vahala, K.J. *Optical microcavities* Nature, 2003, Vol. 424(6950), pp. 839-846

Vernooy1998a Vernooy, D.W., Furusawa, A., Georgiades, N.P., Ilchenko, V.S. & Kimble, H.J. *Cavity QED with high-Q whispering gallery modes* Phys. Rev. A, American Physical Society, 1998, Vol. 57(4), pp. R2293-

Vernooy1998 Vernooy, D.W., Ilchenko, V.S., Mabuchi, H., Streed, E.W. & Kimble, H.J. *High-Q measurements of fused-silica microspheres in the near infrared* Opt. Lett., OSA, 1998, Vol. 23(4), pp. 247-249

Vuckovic2002 Vuckovic, J., Pelton, M., Scherer, A. & Yamamoto, Y. *Optimization of three-dimensional micropost microcavities for cavity quantum electrodynamics* Phys. Rev. A, American Physical Society, 2002, Vol. 66(2), pp. 023808-

Wu2007 Wu, Z., Mi, Z., Bhattacharya, P., Zhu, T. & Xu, J. *Enhanced spontaneous emission at 1.55 mu m from colloidal PbSe quantum dots in a Si photonic crystal microcavity* Appl. Phys. Lett., AIP, 2007, Vol. 90(17), pp. 171105-3

Yablonovitch1987 Yablonovitch, E. *Inhibited Spontaneous Emission in Solid-State Physics and Electronics* Phys. Rev. Lett., American Physical Society, 1987, Vol. 58(20), pp. 2059-

Yamada2001 Yamada, K., Morita, H., Shinya, A. & Notomi, M. *Improved line-defect structures for photonic-crystal waveguides with high group velocity* Optics Communications, 2001, Vol. 198(4-6), pp. 395-402

Yang2009 Yang, A.H.J., Moore, S.D., Schmidt, B.S., Klug, M., Lipson, M. & Erickson, D. *Optical manipulation of nanops and biomolecules in sub-wavelength slot waveguides* Nature, Macmillan Publishers Limited. All rights reserved, 2009, Vol. 457(7225), pp. 71-75

Yee1966 Yee;, K. *Numerical solution of initial boundary value problems involving maxwell's equations in isotropic media* 1966, Vol. Volume 14, Issue 3, May 1966, pp. 302 – 307

Yoshie2004 Yoshie, T., Scherer, A., Hendrickson, J., Khitrova, G., Gibbs, H.M., Rupper, G., Ell, C., Shchekin, O.B. & Deppe, D.G. *Vacuum Rabi splitting with a single quantum dot in a photonic crystal nanocavity* Nature, 2004, Vol. 432(7014), pp. 200-203

APPENDIX A **LIGHT-MATTER INTERACTION IN CAVITIES**

Purcell in 1946 described the modification of light-matter coupling in cavities [**Purcell1946**]. The spontaneous emission of an emitter is dependent on both the optical density of states and the electric field profile at the location of the emitter. Both of these factors can be modified in a cavity. When a single light emitter (like QD) is located inside a cavity, at an electric field maximum, and with its transition dipole moment aligned with the electric field, the coupling parameter g between the exciton and the cavity mode, which is defined as below, reaches a value g_0, the vacuum Rabi frequency.

$$g = \frac{\mathbf{p}\cdot\mathbf{E}_{vac}}{\hbar} \quad \text{A.1}$$

$$g_0 = \frac{p}{\hbar}\sqrt{\frac{\hbar\omega_0}{2\epsilon V}} \ , \quad \text{A.2}$$

where p is the transition dipole moment of the exciton , V is the effective mode volume of the cavity and ϵ is the dielectric constant at the location of the exciton and E_{vac} is the vacuum field, which satisfies $\epsilon V E_{vac}^2 = \frac{\hbar\omega_0}{2}V$ [**Yoshie2004**]. When g is larger than the decay rate of the cavity mode γ_c and exciton dipole γ_e, then the exiton and the cavity will strongly couple and the photon emitted by the excited will be re-absorbed and re-emitted many times before the coupled system decays. When the cavity loss and the relaxation time of the emitter inside the cavity can be neglected, the spontaneous emission will be a reversible process (since the cavity stores the emitted photon in the emitter's neighborhood, it can be reabsorbed and reemitted again and again

and vacuum Rabi oscillation occurs) and in this strong coupling regime there will be entangled states of the exciton and cavity mode.

When g is smaller than the decay rates γ_c, γ_e, the coupling regime is described as "weak", but there can still be a substantial effect of the cavity on the dynamics of the exciton. The excited exciton will couple to the continuum radiation modes and will emit photons irreversibly. However, because of the increased local density of electromagnetic modes per unit volume inside the cavity compared to the free space density of states, the spontaneous emission rate of the exciton will be enhanced in the cavity. The enhancement factor of the spontaneous emission of an emitter inside a cavity (eq.A.3) compared to free space (eq.A.4) is called the Purcell factor (eq.A.5) [**Purcell1946, Noda2007, Vahala2003, Vuckovic2002**].

$$\Gamma = \frac{4Qg^2}{\omega} \qquad \text{A.3}$$

$$\Gamma_0 = \frac{p^2\omega^3}{3\pi\epsilon_0\hbar c^3} \qquad \text{A.4}$$

$$P_0 = \frac{3\epsilon_0\lambda^3}{4\pi^2\epsilon}\frac{Q}{V} \qquad \text{A.5}$$

In some other definitions, the Purcell factor is the emission enhancement relative to a bulk dielectric medium instead of free space (eq.A.6).

$$P = \frac{3}{4\pi^2}\left(\frac{\lambda}{n}\right)^3\frac{Q}{V} \qquad \text{A.6}$$

So when the transition energy of the emitter is resonant and weakly coupled with a cavity resonance, its emission rate will be enhanced by *P*, which is proportional to *Q/V*. From eq. A.6 it would be obvious why tailoring the cavity design to increase this proportionality (i.e. *Q/V*) is crucial in some of photonic device applications including illumination, displays [**Noda2003,**

Schubert2005, Pelton2002, Pelton2002a]. This enhancement can be used to increase the efficiency of the single photon emitters and LEDs.

APPENDIX B **SOME TECHNICAL NOTES ABOUT THE FDTD SIMULATIONS**

During running FDTD simulations, some important points should be noted:

- It is always a good idea to have a 2D index monitor in the simulations to make sure the structures are as they supposed to be (for example all holes with the same radius should be exactly the same on the index monitor).
- Since the NP was very small (50nm in radius) it needed finer mesh cells (about 10nm on less on each dimension). But it would be very time consuming to use such a small mesh cells for the whole simulation region. In this case we defined an override region, only around the NP (Figure B.1). The mesh in this region could be set independently of the rest of the simulations region.
- Care must be taken during setting the boundary and the cell sizes. The boundary of the override region should match with the outside mesh cells. The center and size of the override region should be set in a way that it doesn't shift the outside mesh cells (this will preserve the periodicity of the structure). Also the size of the mesh in the override region should match with its boundary. For example:

  Assume that the cell size out of the override region was $21 \times 21\frac{\sqrt{3}}{2} \times 19.6\, nm^3$, then a good choice for the override region size to cell size inside the override region would be $\frac{21}{4} \times 21\frac{\sqrt{3}}{8} \times \frac{19.6}{4} nm^3$.
- There should be at least one mesh cell between the DFT monitor and the surface of the NP.
- To increase the accuracy of the results on measuring the MST, the DFT monitors were located exactly on the boundaries of the mesh cell (Figure B.1).

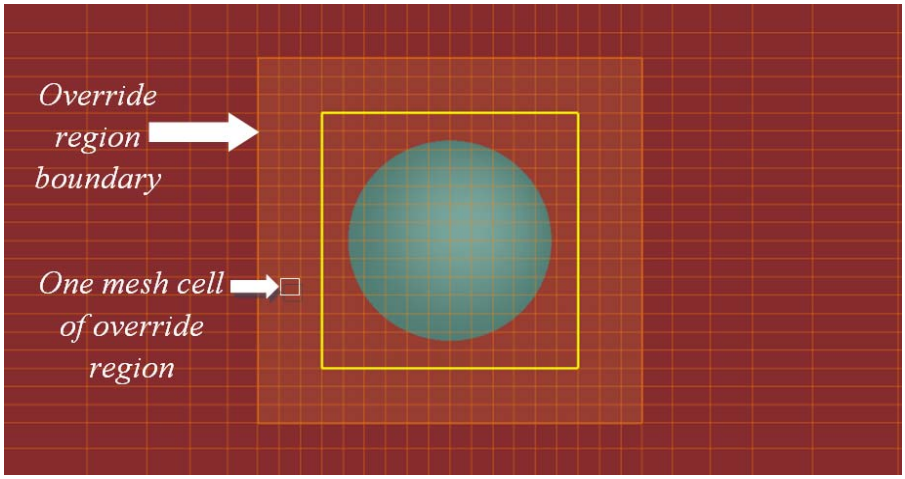

Figure B.1 *This figure shows the situations of the NP, override region and the DFT monitor (top-view). The 2D DFT monitor is the yellow square which exactly matches with the boundaries of mesh cells.*

- Sometimes there are some oscillations in the frequency domain data, which are caused by early termination of the simulation. "These oscillations are the result of the convolution between the true response of the system and the sinc function that comes from stopping the simulation too early" (See User Guide of Lumerical FTDT Solutions). To solve this problem, the simulation should be run for longer time to let the fields decay.